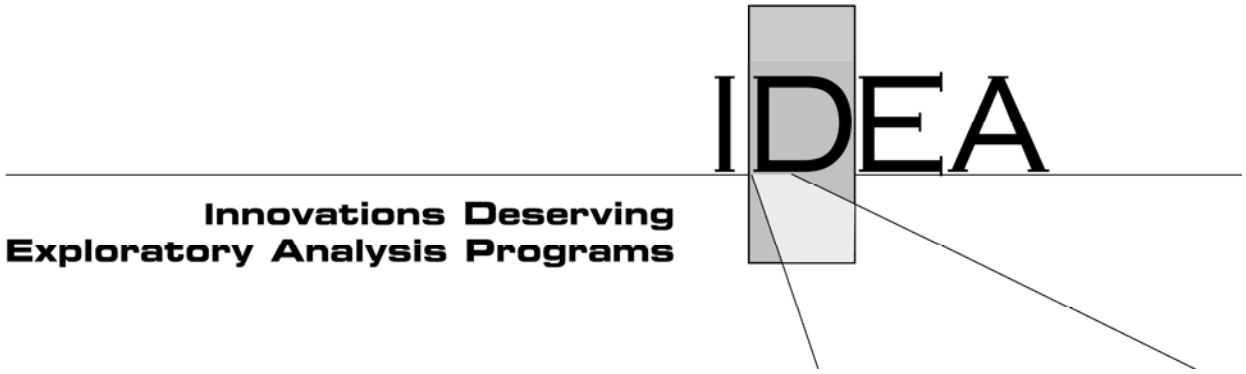

Highway IDEA Program

Manufacture and Testing of a Filament Wound Composite Bridge Superstructure

Final Report for Highway IDEA Project 63

Prepared by:
I.D. Parsons, S. White, D. Therriault, J. Bignell, University of Illinois

February 2002

TRANSPORTATION RESEARCH BOARD
OF THE NATIONAL ACADEMIES

INNOVATIONS DESERVING EXPLORATORY ANALYSIS (IDEA) PROGRAMS
MANAGED BY THE TRANSPORTATION RESEARCH BOARD (TRB)

This NCHRP-IDEA investigation was completed as part of the National Cooperative Highway Research Program (NCHRP). The NCHRP-IDEA program is one of the four IDEA programs managed by the Transportation Research Board (TRB) to foster innovations in highway and intermodal surface transportation systems. The other three IDEA program areas are Transit-IDEA, which focuses on products and results for transit practice, in support of the Transit Cooperative Research Program (TCRP), Safety-IDEA, which focuses on motor carrier safety practice, in support of the Federal Motor Carrier Safety Administration and Federal Railroad Administration, and High Speed Rail-IDEA (HSR), which focuses on products and results for high speed rail practice, in support of the Federal Railroad Administration. The four IDEA program areas are integrated to promote the development and testing of nontraditional and innovative concepts, methods, and technologies for surface transportation systems.

For information on the IDEA Program contact IDEA Program, Transportation Research Board, 500 5th Street, N.W., Washington, D.C. 20001 (phone: 202/334-1461, fax: 202/334-3471, http://www.nationalacademies.org/trb/idea)

Table of Contents

c.1

1. Introduction and Objectives

This report documents the research performed under contract number NCHRP-63, "Manufacture and Testing of a Filament Wound Composite Bridge Superstructure," by I. D. Parsons (Associate Professor of Civil Engineering), S. White (Associate Professor of Aeornautical and Astornautical Engineering), D. Therriault (Graduate Research Assistant, Department of Aeronautical and Astronautical Engineering) and J. Bignell (Graduate Research Assistant, Department of Civil and Environmental Engineering) at the University of Illinois at Urbana-Champaign from October 1999 to August 2001.

The primary aim of this work was to determine the manufactuability and experimental performance of a conceptual design for a filament wound bridge superstructure described in [3,4]. Finite element simulations [4] demonstrated that the proposed design can withstand the loads of heavy traffic, with a weight saving of at least 50% over a conventional steel-concrete bridge. This weight saving can be translated into lower construction costs, and increased seismic resistance (since the supporting columns have to carry less load). Furthermore, the durability of the fiber glass reinforced material will substantially reduce the life cycle cost of the bridge (i.e., the material eliminates corrosion problems associated with reinforced concrete decks).

However, before the construction industry can be expected to invest in the development of this structural system necessary to produce fully functioning structures, the manufacturing process and theoretical predictions must be verified by building and testing some small scale prototypes. The primary objectives of this research project were therefore:

1. Build a small number of scaled prototypes to demonstrate the feasibility of the manufacturing procedure;
2. Test the prototypes measure their stiffness, strength and fatigue properties;
3. Build finite element models of the fabricated specimens to determine if their structural properties can be predicted.

The report is organized in the following manner. Section 2 summarizes relevant work by other researchers and discusses the features of the conceptual design. Section 3 described the procedures that were adopted to produce the specifications for the small-scale prototypes that were manufactured and tested. The design of the fabrication equipment is documented in Section 4. The manufacturing process is described in Section 5. The experimental equipment used to test the structural performance of the prototype bridges is described in Section 6. Section 7 contains the experimental data obtained using this equipment. Section 8 presents the results of finite element simulations of the manufactured prototypes. The results of this research project are discussed in Section 9.

2. FRP Bridge Designs

This section presents a brief overview of fiber reinforced plastic bridge research performed by other workers, and outlines the structural features and manufacturing processes of the bridge design considered in this report.

2.1 Overview of Previous Research

Bridges are vital components of the nation's infrastructure, many of which are deteriorated. The total estimated cost of bringing deficient bridge superstructures to an acceptable level is $110 billion [6]. Fiber-reinforced plastics present several advantages over conventional bridge materials. One of the primary sources of bridge deterioration is steel corrosion. The de-icing chemicals used in winter deteriorate the structural sections and the reinforcing re-bars in conventional designs. Fiber reinforced material is a viable solution to this problem. In earthquake prone areas, lightweight modular bridge components can be used as permanent replacements for damaged bridges to reduce the interruption of traffic that normally accompanies conventional construction. The availability of such designs will aid in restoring bridges faster than other methods of construction. Moreover, the low weight of composite materials, resulting in lower inertia forces, can be a significant factor in designing bridges subjected to seismic activity.

These observations have motivated several researchers to consider fiber reinforced plastics as an alternative bridge construction material, primarily because of the corrosion resistance of this class of materials. These efforts can be divided into three categories: retrofitting schemes to repair and upgrade bridge components (e.g., [7],[11]); design of replacement components made from fiber reinforced plastics (e.g., [11],[13],[15]); and the design of new structures fabricated from composites (e.g., [5],[10],[16]).

A number of fiber-reinforced polymer (FRP) bridges have been designed or constructed in the United States and other countries. In England, the first FRP bridge to carry trucks was recently completed ([10]). The bridge, with a 26.9 ft. span and a width of 14.25 ft., crosses the Stroudwater Canal and is considered an important example of the use of FRP in a civil engineering application. Lockheed Martin Corporation researchers designed and tested a 30 ft. span bridge ([5]) in which pultruded panels form the bridge

deck and are attached to three U-shaped girders with mechanical fasteners. This structure carried a load of up to 100 kips without failure. Measurements of strain in the deck and the beam components of this bridge revealed a significant margin of safety when comparing these values with the material's ultimate strain.

The design and construction of a 450 ft. cable-stayed bridge that will cross U.S. 5 in California is being studied by government, industry, and the University of California at San Diego (UCSD). UCSD researchers also have developed modular short-span bridge systems ([16]), employing a fiberglass bridge deck supported by a number of carbon shells filled with lightweight concrete. More recently, a 33 ft. span FRP bridge was designed and constructed in Ohio through a collaborative effort between the State of Ohio, private industry, and Wright Patterson Air Force Base engineers ([8]). A bridge deck system developed by researchers at West Virginia University and constructed of pultruded sections was used to replace the deck of Laurel Lick Bridge in West Virginia ([12]). In New York State, two FRP bridge systems are planned for construction. A bridge superstructure built by Hardcore Composites of New Castle, Delaware, has been completed, and another FRP bridge deck is still in the planning process ([1]). A comprehensive discussion of the current state-of-the-art is given in [14].

2.2 The Proposed Filament Wound Bridge Superstructure

The proposed structural system studied in this report evolved to its final stage by considering manufacturing techniques, material capabilities and structural behavior. The resulting design represents a new integral bridge superstructure that does not mimic current bridge design. Deviation from current practice is essential if FRP is to be used successfully in bridges, since conventional design and construction methodologies are tailored specifically to the inherent advantages of steel and concrete, and using the same designs cannot be expected to produce an efficient fiber reinforced bridge structure.

2.2.1 Structural System

The bridge superstructure is shown in Figure 2.1 and consists of two components: a series of inner cells, lying parallel to the direction of traffic, and an outer shell. Special consideration was given to three factors when this design was developed. First, filament

winding was chosen as the basic manufacturing procedure, since it allows for automated manufacturing, with faster fabrication cycles and reduced manufacturing costs. Second, attention was given to the transfer of shear between the different components; the oval inner cells provide sufficient contact area to reduce the shear stress to acceptable values. Third, additional stiffness and strength was developed by incorporating shell behavior into the structure, rather than relying solely on plate bending common in standard bridge deck designs. Shell action is obtained by providing contact between the inner cells.

The proposed design has several important features. The designer can readily choose the material, winding angles and thickness of plies to comply with appropriate strength and stiffness criteria. The circular shapes used in the inner cells and the outer shell avoid stress concentrations that are present at corners of an I- or box-section. Effective transfer of shear through the bridge is achieved by providing large contact areas between the inner cells and the outer shell. The contact area can be chosen based on the shear strength of the bonding material. The proposed design develops shell action in a structure primarily acting in bending by providing contact between the inner cells at the mid-surface.

Previous research [4] used finite element analysis to investigate the potential performance of this structural system. For example, a two lane highway bridge with a span of 60 ft., a width of 30 ft. and a depth of 3 ft. was designed. These dimensions are typical of many highway bridges found in the U.S.A., and produce a length-to-depth aspect ratio of 20:1, which is within the ranges found in bridges constructed using conventional materials. The numerical model of the bridge was subjected to the traffic loads specified by AASHTO [2]. The analysis demonstrated that the L/800 deflection criterion controls the design with a weight saving of at least 50% over a conventional steel-concrete bridge.

2.2.2 Manufacturing Process

The bridge is manufactured using the filament winding process. Filament winding is a manufacturing technique that has been used extensively in the aerospace industry since the early 1960's. The principles of filament winding are presented in Figure 2.2. Filament is wound onto a mandrel surface through a payout head that traverses along the length of a rotating mandrel. The angle at which fibers are placed in relation to the mandrel axis

can be controlled by the ratio of the traverse speed of the payout head to the rotational speed of the mandrel. This delivers high-speed and accurate lay-up of fiber reinforcement around the mandrel. The fiber winding angles are machine controlled to form the required stacking sequence specified by the designer. Several types of reinforcement can be used, including fibers, prepreg tape and rovings. Subsequent to filament winding of the structure, the entire assembly is then cured either in an autoclave or oven, with a vacuum bag being used around the structure to draw off voids during the cure cycle.

The filament wound bridge considered in this report is manufactured in a two stage process. First, the inner cells of the bridge deck are filament wound and cured separately using a mandrel that can be extracted after cure. After manufacturing the inner cells are trimmed and prepared for integration with the outer shell.

The outer shell structure is constructed by winding filament directly onto the inner cells as shown in Figure 2.3. A series of inner cells are coupled together with a mandrel framing system. The frame is assembled to end pieces that contain a chuck coupling that fits into the filament winder chucks. Once the inner cell mandrel system is placed into the filament winder, the outer shell filaments are wound onto the inner cell surfaces. The entire assembly is then cured in an autoclave under vacuum pressure to produce the finished part.

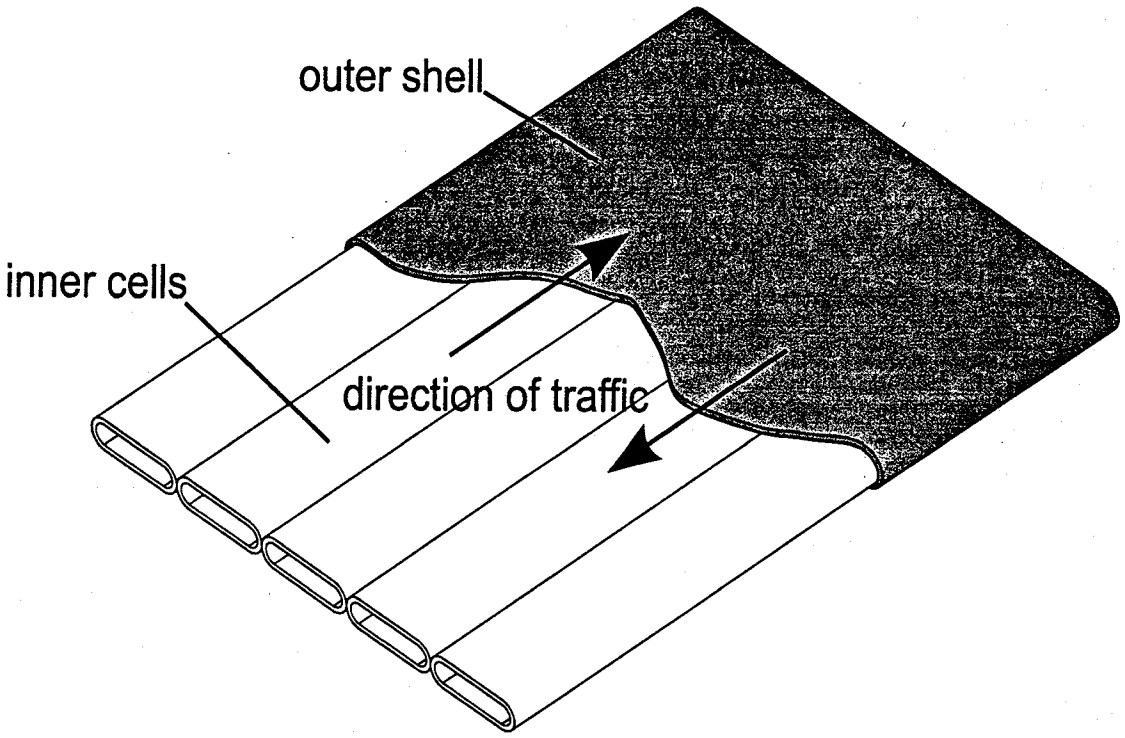

Figure 2.1: Filament wound bridge superstructure conceptual design.

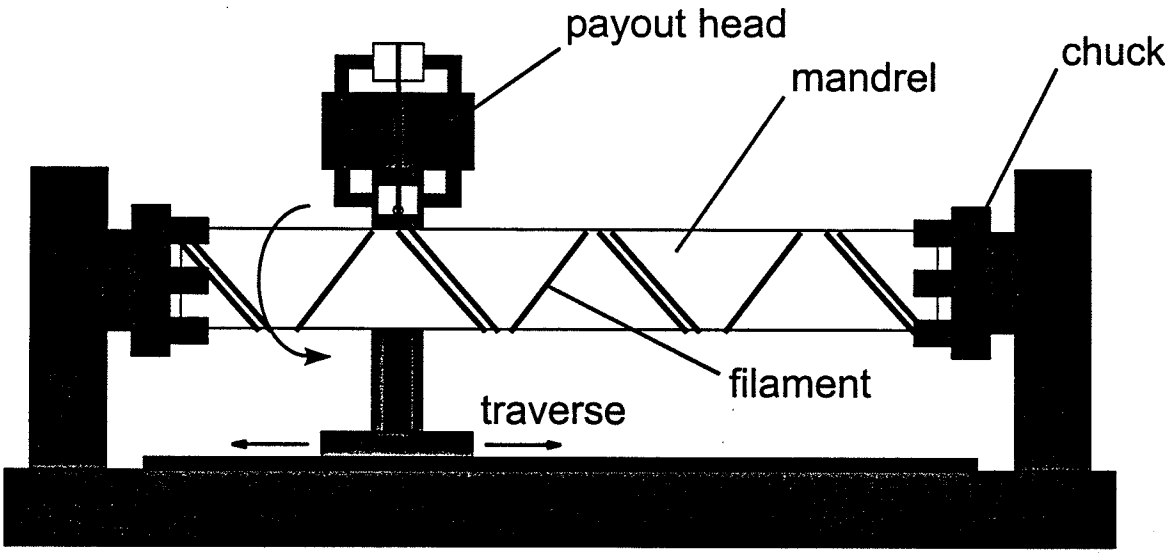

Figure 2.2: The filament winding process.

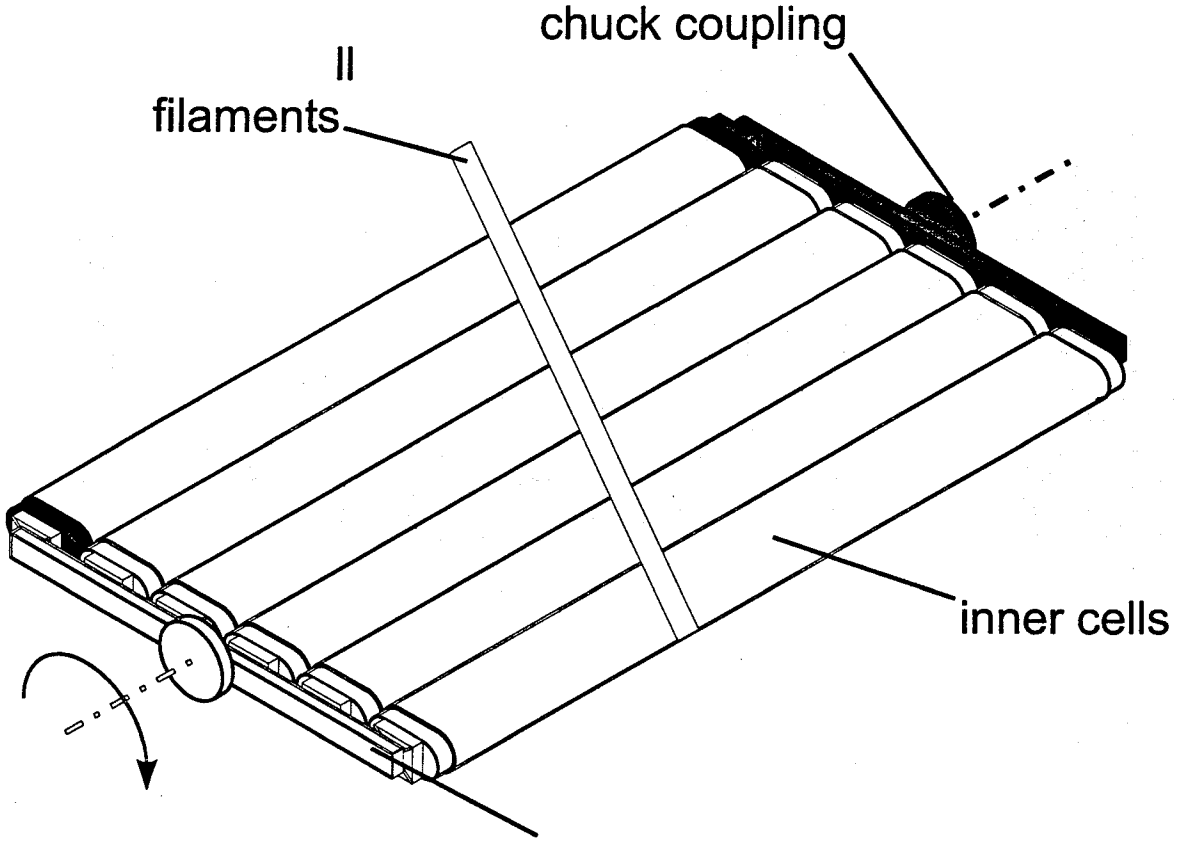

Figure 2.3: Filament winding of the outer shell onto the inner cells.

3. Initial Design of the Prototype Bridge

This section describes the initial design of the small-scale prototype filament wound bridges that were manufactured and tested. Small-scale versions of the bridge design described in Section 2 were necessitated by the dimensions of the filament winder and autoclave available at the University of Illinois. The filament winder had a maximum part diameter of 32 in. and a maximum length of 8 ft., and the autoclave used to curing of the wound parts had an inner diameter of 32 in. and a total length of 80 in. Thus, in order to preserve the aspect ratios encountered in full-size highway bridges, each model was approximately 60 in. long, 24 in. wide and 3 in. deep. Six inner cells were used in each specimen.

In order to make more detailed selections for the various dimensions of the model bridges, an Excel worksheet was created to optimize the prototype dimensions, see Figure 3.1. The spreadsheet computes the prototype aspect ratios with those of a hypothetical full-size structure. The input parameters are indicated with yellow cells and are:

- Cell and shell thickness;
- Inside radius of the cell;
- Width the flat surface of the cell;
- Number of cells;
- Total length of the bridge.

The computed outputs are:

- Bridge length to width aspect ratio;
- Bridge length to depth aspect ratio;
- Bridge width to depth aspect ratio;
- Shell thickness to cell thickness ratio;
- Total coverage area to area of the cross-section ratio;
- Weight of the bridge;

- Approximate price of the bridge.

The price reflects the cost of materials only, and is computed by multiplying the weight of the bridge with the price per pound of the material.

After a number of iterations, the initial bridge geometry shown in the spreadsheet column denoted as "standard" was selected. This geometry has aspect ratios that are very similar to those that would be expected in the full-size structure. Note that the input parameters of the inner cell (inner radius and flat surface) for this geometry are rounded to preferred sizes in order to construct the mandrel with standard tubing.

After the geometric dimensions of the model bridge had been selected, appropriate winding angles of the inner cell and the outer shell had to be chosen. The limitations of the manufacturing equipment were the controlling factor. Ideally, the winding angle and thickness of each layer in the inner cells and outer shell would be specified used the optimization procedure described in [3]. However, given that the length of the test specimens were close to the maximum mandrel length of the filament winding machine, only a limited range of winding angles could be considered. This is as result of the need to provide sufficient excess material when winding the outer shell to allow the payout head to change direction. Small winding angles (where 0° and 90° represent winding angles parallel and perpendicular to the axis of the rotating mandrel, respectively) would require more excess material, and would consequently limit the final length of the finished part. Large winding angles would avoid this problem, but would tend to produce specimens with low stiffness and strength. Therefore, two winding angle configurations were chosen that represent a compromise between these two competing factor:

- Inner cell 45°, outer shell 30°;
- Inner cell 45°, outer shell 45°.

Table 3.1summarizes the selected nominal dimensions of the specimens. It should be noted that these dimensions were limited by the available manufacturing equipment, and were not chosen to optimize the structural performance of the filament wound bridge superstructure.

	Shell	Cell
Number	1	6
Length	60 in.	60 in.
Width	23.875 in.	3.938 in.
Depth	2.9375 in.	2.688 in.
Thickness	0.125 in.	0.09375 in.

Table 3.1: Summary of the prototype bridge dimensions.

Part	Parameter	ID	Unit	Full Size	Scaled1	Scaled2	Standard
CELL	Thickness	t	in	0.75	0.125	0.0625	0.09375
	Outer radius	ro	in	16.772	1.313	1.406	1.344
	Inner radius	ri	in	16.022	1.188	1.344	1.250
	Flat distance	d	in	8.986	1.313	1.156	1.250
	Width	wcell	in	42.531	3.938	3.969	3.938
	Height	hcell	in	33.545	2.625	2.813	2.688
	Volume	vcell	in^3	65340.3	78.6	41.1	59.9
	Weigth	Wcell	lb	4247.1	5.1	2.7	3.9
SHELL	Thickness	T	in	1.141	0.1875	0.09375	0.125
	Outer radius	Ro	in	17.913	1.500	1.500	1.469
	Inner radius	Ri	in	16.772	1.313	1.406	1.344
	Width (total Width)	wshell	in	300	24	24	23.875
	Height (total Depth)	hshell	in	35.8267	3	3	2.9375
	Volume	vshell	in^3	523567.0	571.9	287.6	380.3
	Weight	Wshell	lb	34031.9	37.2	18.7	24.7
BRIDGE	Number of cells	N		7	6	6	6
	Total Length	Lcell	in	720	60	60	60
	Ratio : Length / Width	Rlw	in / in	2.40	2.50	2.50	2.51
	Ratio: Length / Depth	Rld	in / in	20.10	20.00	20.00	20.43
	Ratio : Width / Depth	Rwd	in / in	8.37	8.00	8.00	8.13
	Ratio : Tshell / T cell	RTt	in / in	1.52	1.50	1.50	1.33
	Ratio : Area cov. / Area mat.	Rcov-mat	in^2/in^2	7.69	4.03	7.87	5.54
	Total Weight of cells	Wcellt	lb	29729.8	30.7	16.0	23.4
	Total Weight of bridge	Wtot	lb	63761.7	67.8	34.7	48.1
3 BRIDGES	Weight for 3 bridges	W3tot	lb	191285	203	104	144
	Approx. Price for fiber	Pf	$	215196	229	117	162
	Approx. Price for resin	Pr	$	717319	763	391	541
	Total Price	Ptot	$	932514	992	508	703

Figure 3.1: Excel worksheet used for selection of the bridge geometry.

4. Manufacturing Tooling Design

This section described the tooling that was designed and fabricated to facilitate the manufacture of the bridge superstructure using the equipment available at the University of Illinois. Two sets of tooling were required: a mandrel for winding the inner cells, and supports to hold the inner cells in place during the winding of the outer shell.

4.1 Inner Cell Mandrel

An aluminum mandrel was designed and manufactured to serve as the mandrel used to wind the inner cells. Aluminum was chosen because of its high coefficient of thermal expansion and its ease of machining. In order to reduce cost, this mandrel was assembled from standard box and circular tube stock to create the desired cross-section shown in Figure 4.1. Figure 4.2 shows engineering drawings of the complete mandrel. A 1.25 in. by 2.5 in. rectangular tube was connected to two halves of a 2.5 in. diameter tube using steel screws spaced at 6 in. intervals along the 84 in. length of the mandrel. Two inner cells mandrels were built to facilitate rapid manufacture of the required cells.

Each end of the mandrel required an extension so that the mandrel could be installed on the filament winder. Figure 4.3 shows drawings of the aluminum block extensions that were fabricated for this purpose. Figures 4.4 and 4.5 show photographs of these extensions. The tailstock end of the mandrel incorporates an aluminum block fixed inside the mandrel with two lateral screws. The headstock end of the mandrel, which locates into the chuck of the filament winder), requires a circular cross-section extension block, which is also fixed into the mandrel with lateral screws.

Each mandrel was tapered using several spacers located along the mandrel length. The spacers were inserted between the cut circular tube edges and the lateral side of the rectangular tube as shown in Figure 4.6. The spacer size was 0.040 in. at the tailstock end of the mandrel and decreased to zero at the headstock end in increments of 0.010 in. This taper greatly eased the removal of the cured inner cells from the mandrel.

4.2 Support for Outer Shell Winding

The bridge design considered in this report use the inner cells as the mandrel during the winding of the outer shell. Tooling was therefore required that would hold the selected number of inner cells (that was either two or six for the prototype bridges considered in this project) in place curing this phase of the manufacturing procedure. This tooling had to be adjustable so that different cell of different thickness could be accommodated and so that gaps of various dimensions could be introduced between the cells. Furthermore, this tooling had to be designed to fit inside the available autoclave that was used to cure the outer shell after the filaments had been wound in place. Figure 4.7 shows engineering drawings of the tooling that was manufactured to fulfill these objectives; this figure also indicates the dimensions of the autoclave employed.

The outer shell support tooling consists of two aluminum bars to which up to six inner cell extensions can be attached. An aluminum bar is shown in Figure 4.8, and Figure 4.9 shows six inner cell extensions attached to one of these bars. Figures 4.10 and 4.11 show engineering drawings of these components. The inner cell extensions are simply 12 in. long versions of the inner cell mandrel, with rectangular blocks attached to the inside the rectangular tube in a manner similar to the tailstock extension described above. The long aluminum bars are 32 in. long and contain two grooves and slots. The slot provides the required adjustment between the positions of the inner cells by allowing the inner cells to be moved laterally across the axis of the bridge. The groove is 0.25 in. deep and constrains the rotation of the inner cell extension about its longitudinal axis.

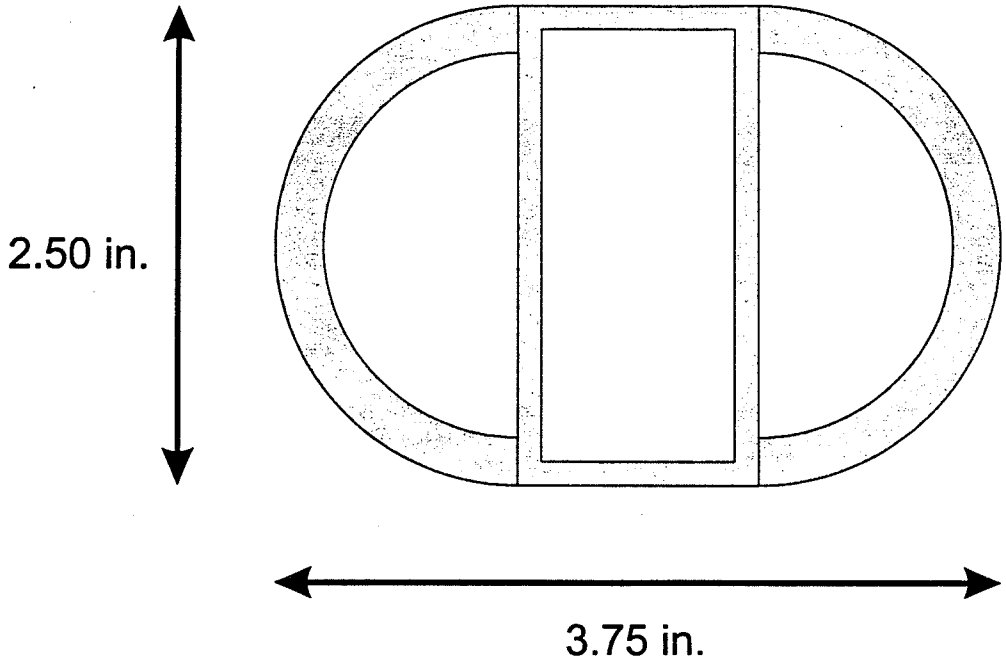

Figure 4.1: Inner cell mandrel cross section.

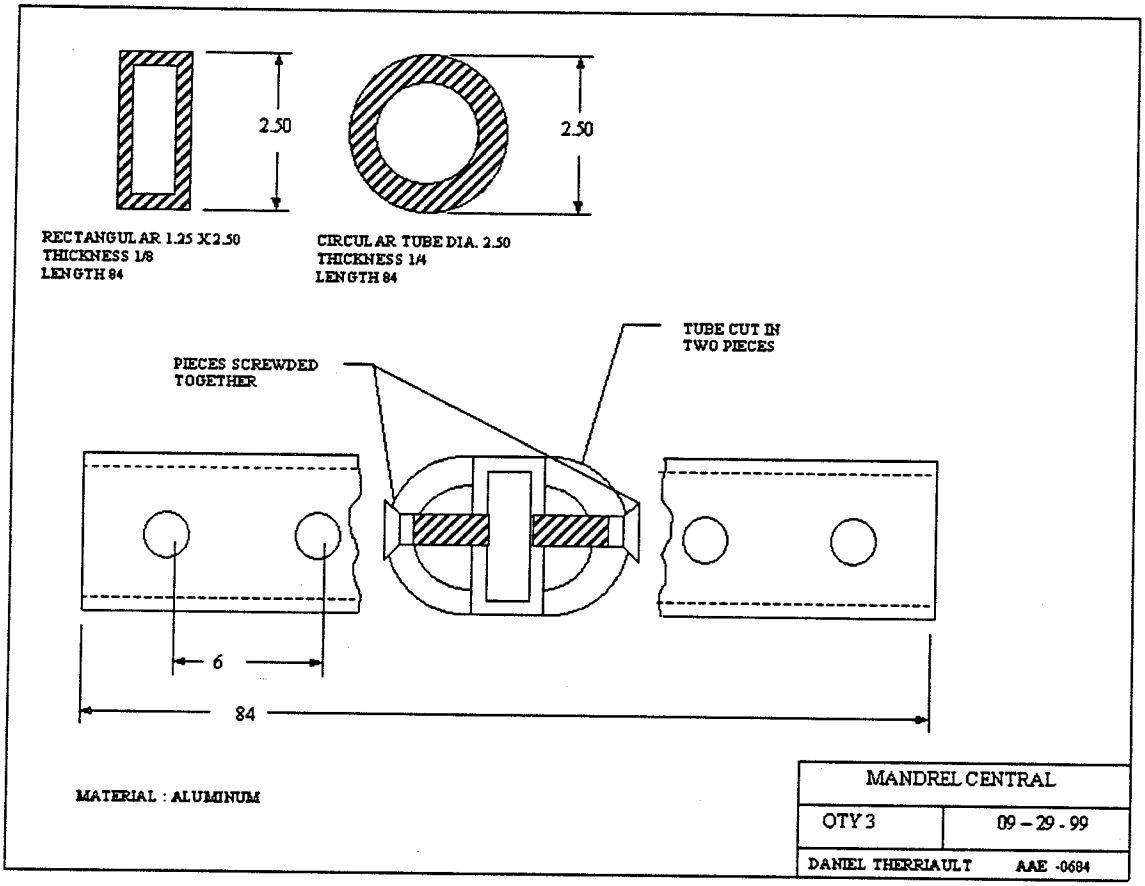

Figure 4.2: Engineering drawing of the inner cell mandrel.

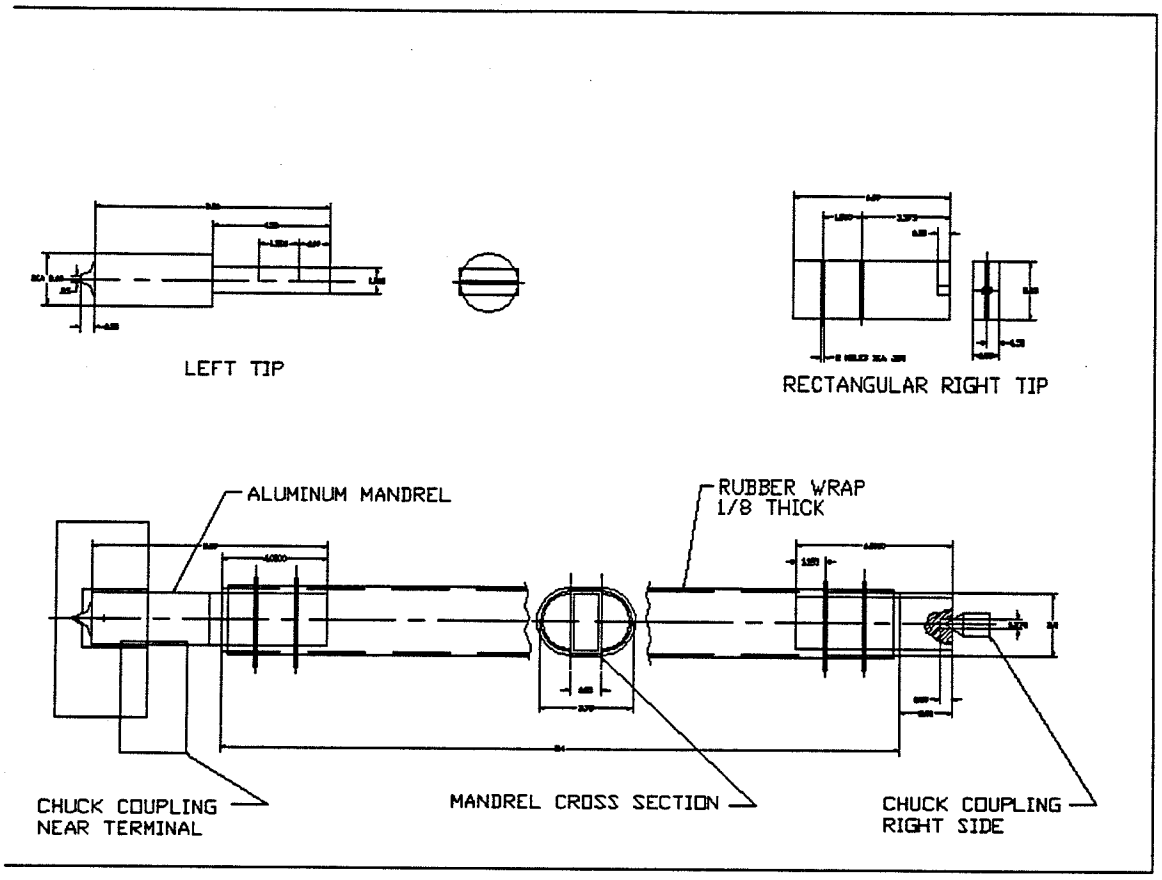

Figure 4.3: Enginnering drawing of the inner cell mandrel and extension blocks.

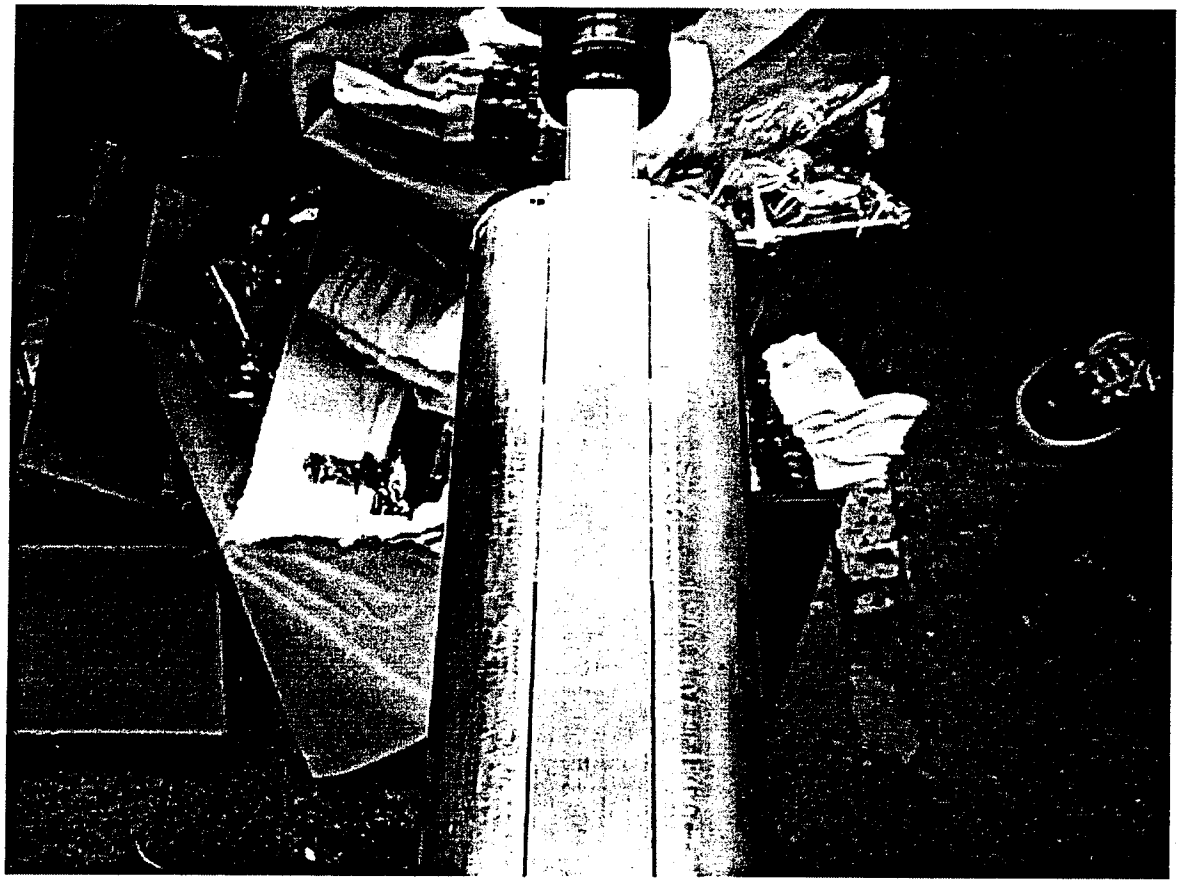

Figure 4.4: Tailstock end of the inner cell mandrel.

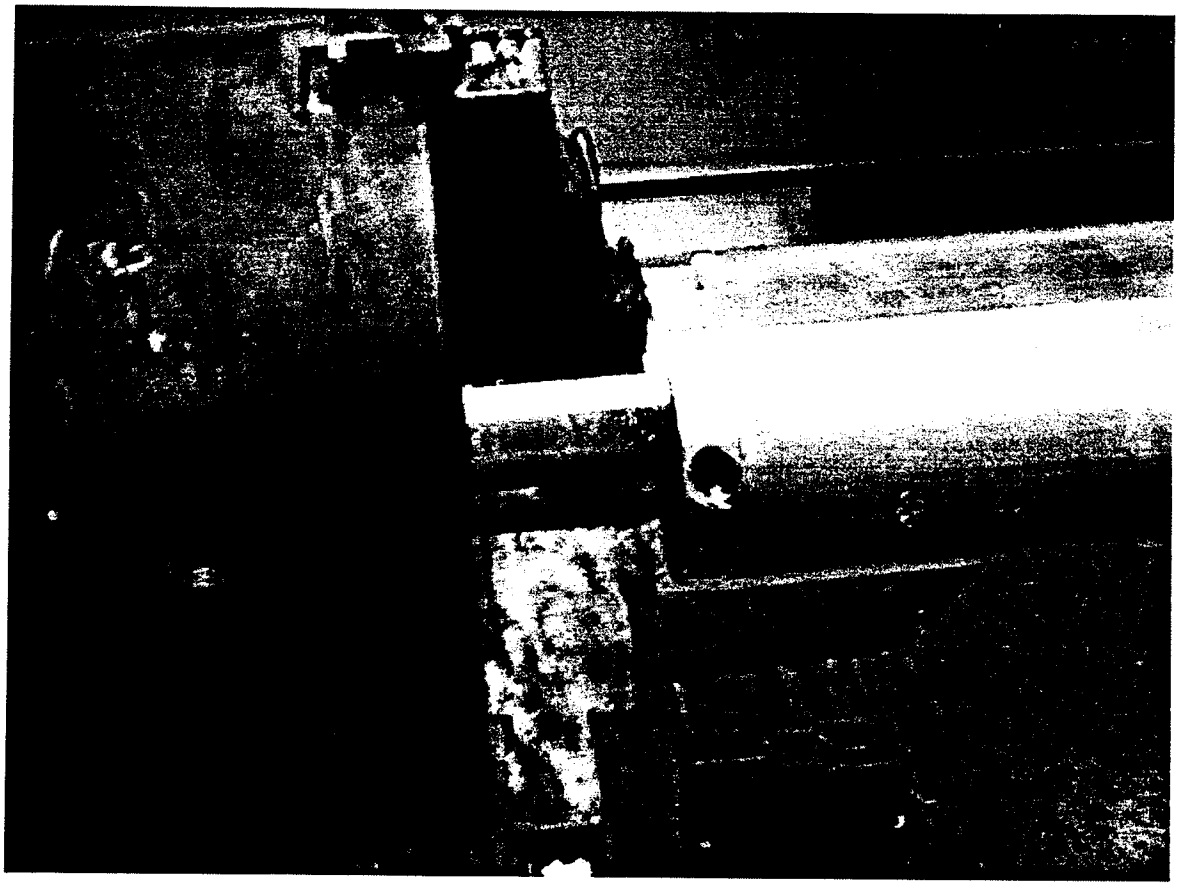

Figure 4.5: Headstock end of the inner cell mandrel.

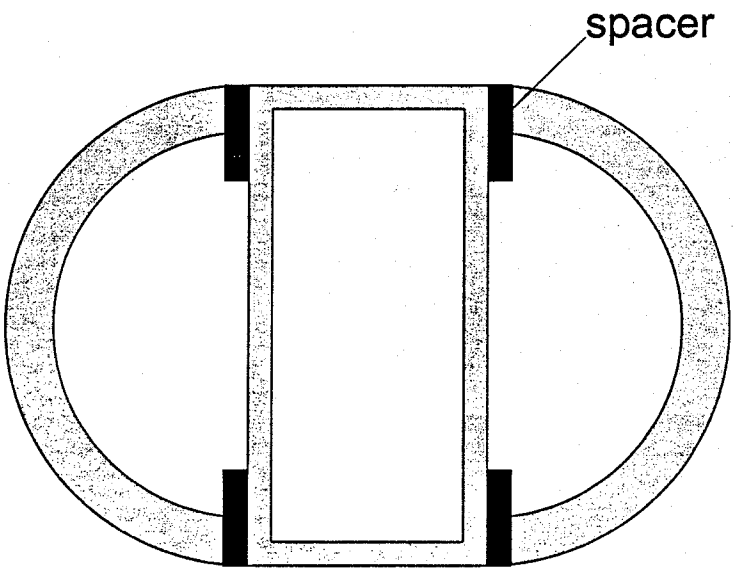

Figure 4.6: Location of the inner cell mandrel spacers.

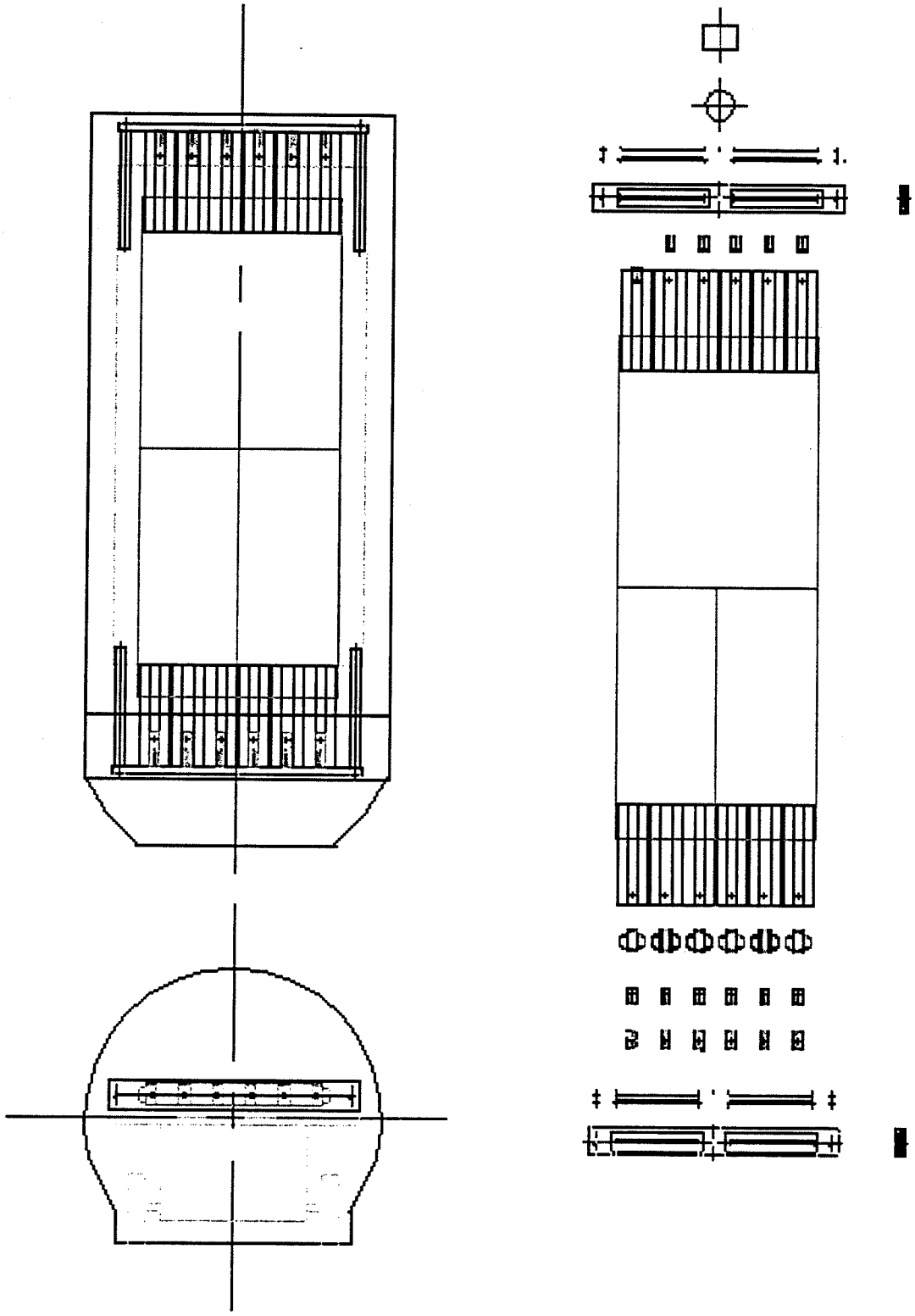

Figure 4.7: Enginnering drawing of the outer shell support tooling.

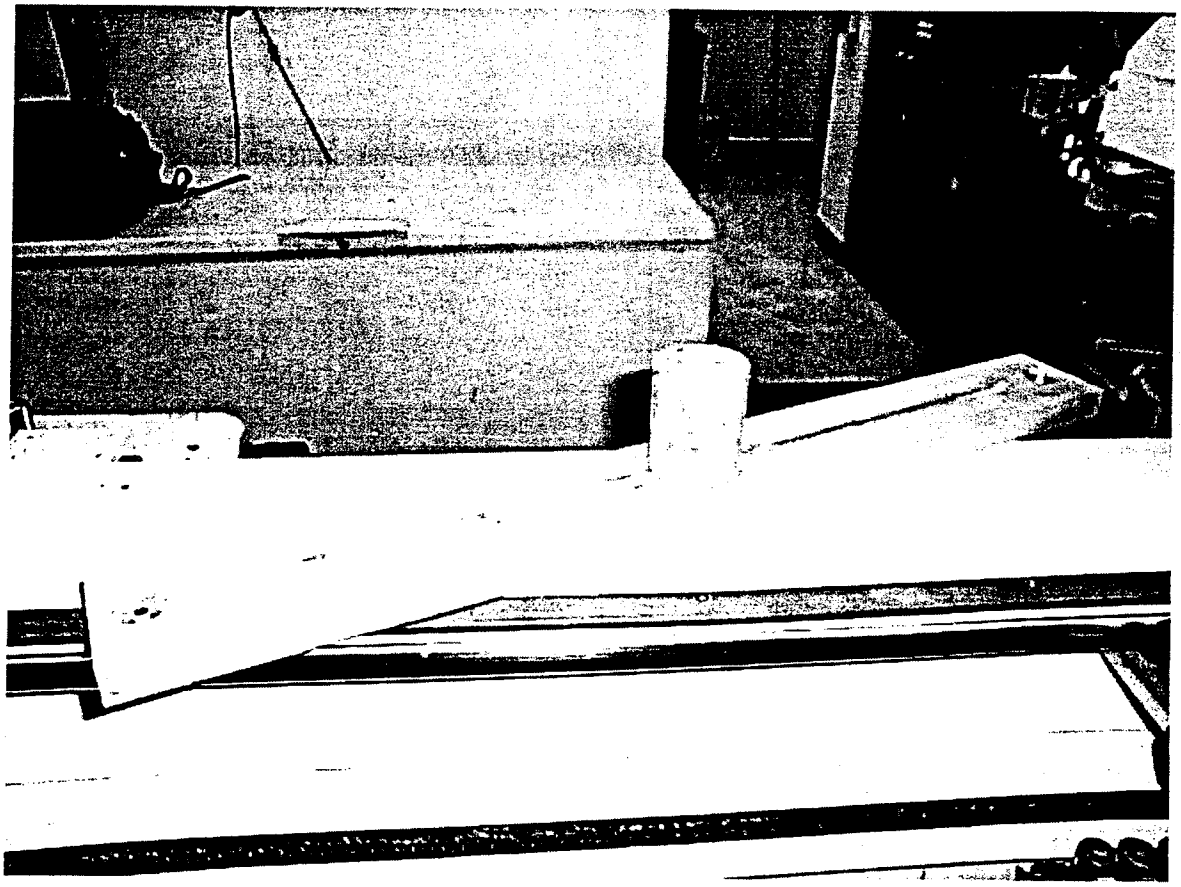

Figure 4.8: Aluminum bar used in the outer shell support tooling.

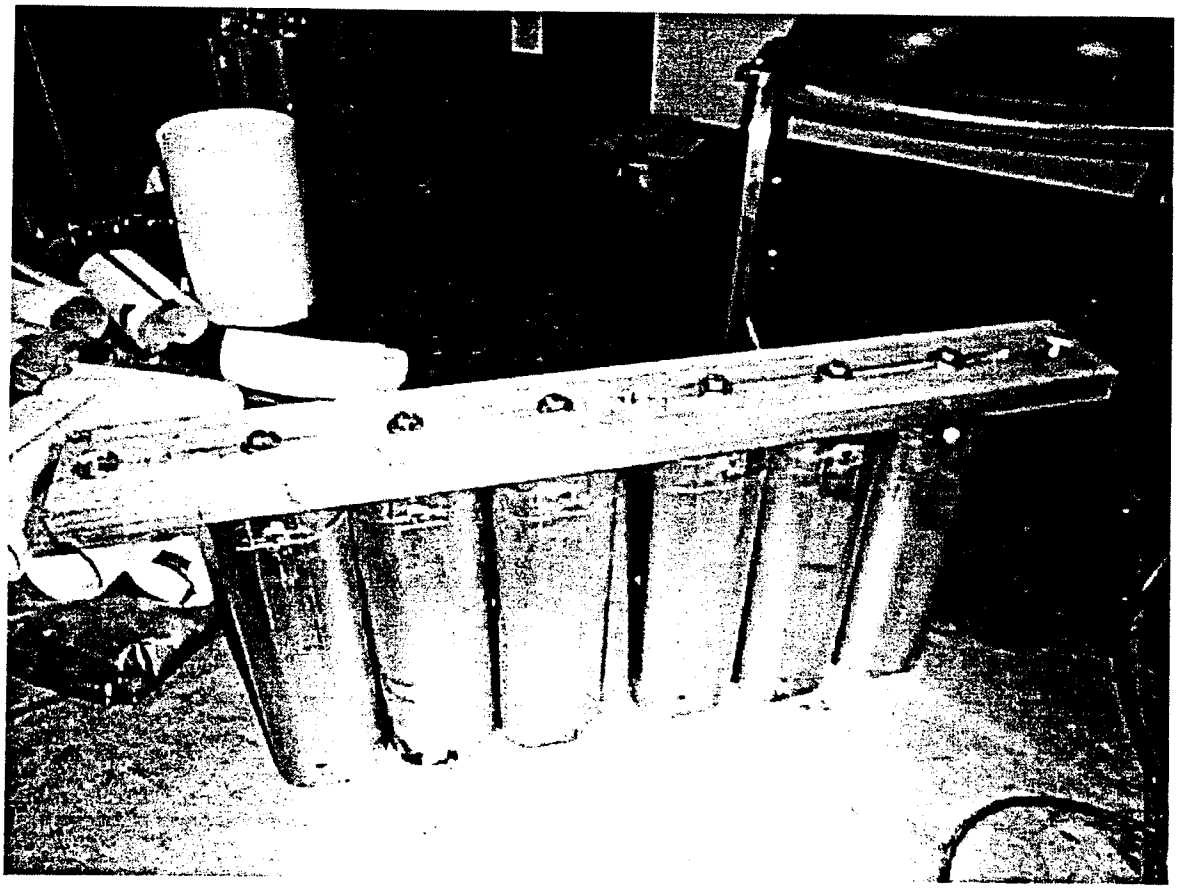

Figure 4.9: Aluminum bar with inner cell support blocks used in the outer shell support tooling.

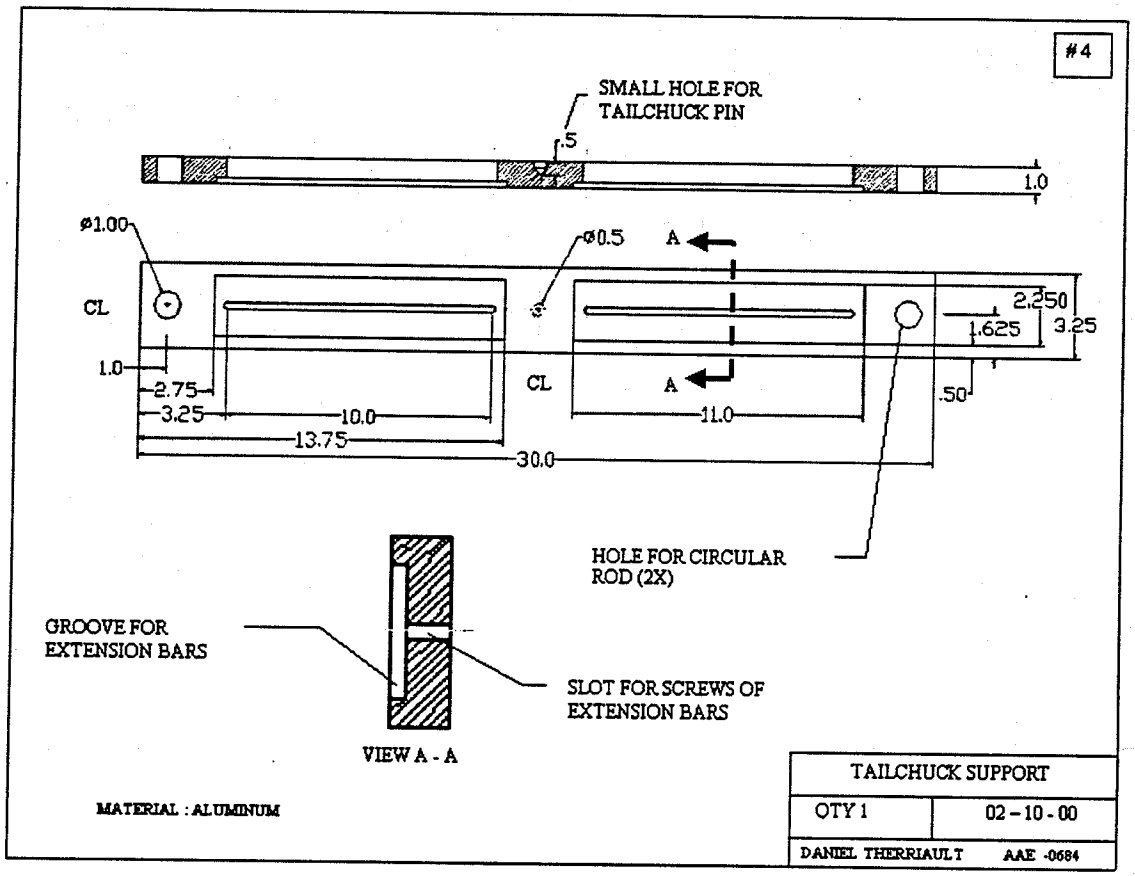

Figure 4.10: Engineering drawing of the aluminum bar used in the outer shell support tooling

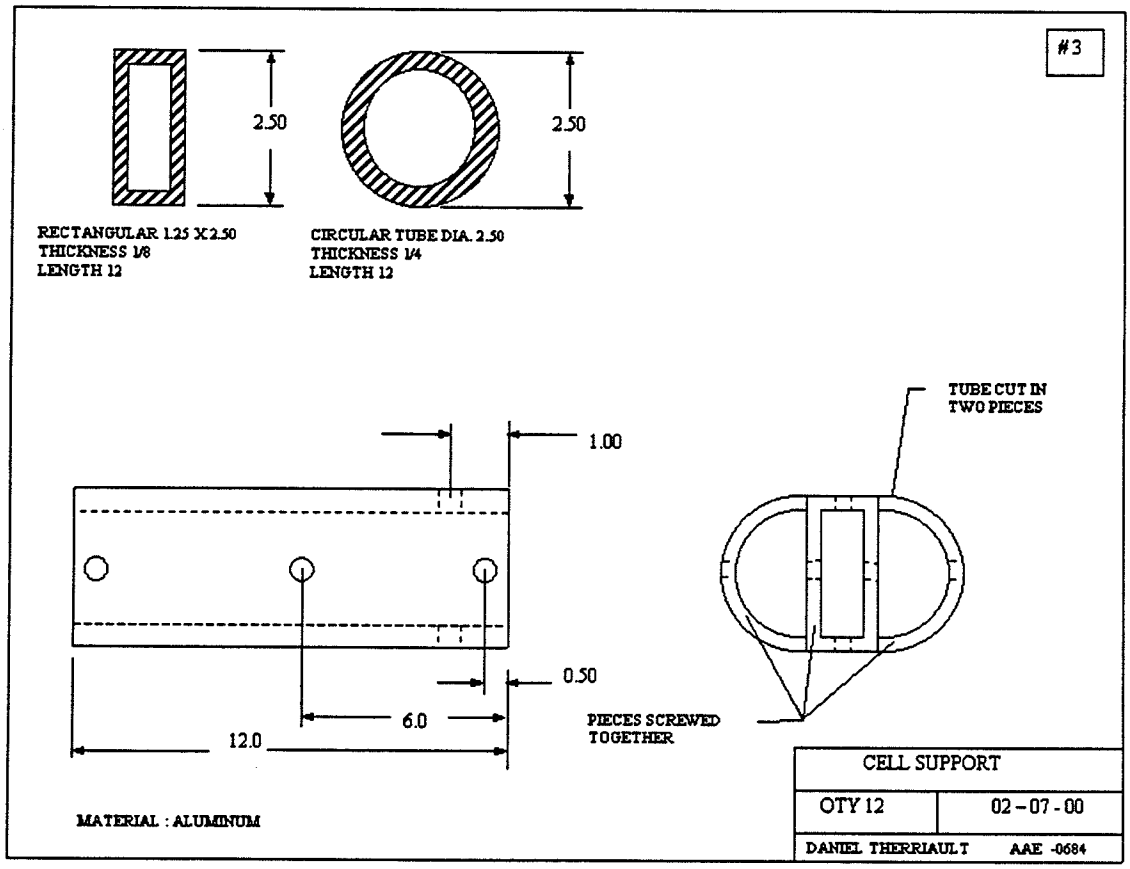

Figure 4.11: Engineering drawing of the inner cell support blocks used in the outer shell support tooling.

5. Filament Winding Manufacturing Process

This section describes the filament winding manufacturing process that was used to manufacture the test specimens examined in this study. This process delivers high-speed and accurate lay-up of fiber reinforcement around a mandrel. Since large volumes of materials are involved in the construction of bridge superstructures, the choice of filament winding is an attractive solution for automating the manufacturing process. It also allows the designer to optimize the winding angle and ply thickness for maximum structural performance.

The two components of the bridge superstructure (the inner cells and the outer shell) were made using the filament winding process. In this section, the equipment nad material used to manufacture the bridges are discussed, followed by a step-by-step description of the manufacture of the inner cells and the outer shell.

5.1 Manufacturing Equipment

5.1.1 The Filament Winder

The filament winder employed in this study an En-Tec four axis machine shown in Figure 5.1. The four winding axes shown in this figure are:

- Motion of the payout head along the longitudinal axis of the mandrel;
- Motion of the payout head along the vertical axis perpendicular to the mandrel;
- Rotation of the eye on the payout head;
- Rotation of the mandrel.

A sketch of the winder is shown in Figure 5.2. The principal components of the winder are: a payout head to wind the fiber that translates along axes 1 and 2, a rotating eye to wind a helical pattern that rotates along axis 3, a mandrel that rotates to wind the fiber, a tailstock chuck that holds the tailstock end of the mandrel, a headstock chuck that holds the headstock end of the mandrel, a control terminal, a material rack that contains the spools of material and extensioners which control the fiber tension during the winding, and a personal computer that creates the winding pattern file.

The maximum part dimensions that can be manufactured on this machine is a diameter of 32 in. and a length of 8 ft.. The winding pattern is created on a PC with the software program FGX; the filament winder is operated using the program WIMAX 2.

5.1.2 Autoclave

A filament wound composite part is cured using the autoclave shown in Figure 5.3. The autoclave heats the part using the selected temperature curing cycle while applying a vacuum pressure to the part. Thermocouples are placed on the part an in the interior of the autoclave to monitor the temperature time history.

5.2 FRP Composite Materials

The spools of FRP composite material must be installed in the material rack shown in Figure 5.4. Two types of FRP material were used in this project: an E-glass/epoxy prepreg tow and a carbon/epoxy prepreg tow, both manufactured by TCR Composites. In both cases, the resin used was designated UF3325 by the manufacturers. The E-glass fibers were Roving 158B AB 450 Tack-Pak Wrap Bulk Unit Stretch Wrap, and the carbon fibers were Toray T700 -12000 -50C.

When winding a component, it is best to use two spools of material at the same time to reduce the winding time. The utilization of a prepreg material requires the use of the prepreg fiber disposal of the payout head, see Figure 5.5. After the tows were correctly installed, the extensioners were calibrated in order to control the tension during the winding. The fiber tension was controlled mechanically by the springs inside the extensioners.

The prepreg FRP material was stored in a freezer to extend its storage life. The suggested temperature curing cycles are listed in Table 5.1. An example of a recommended cure profile is illustrated in Figure 5.6.

5.3 Manufacture of the Inner Cell

Many cells were manufactured during the course of this project. The preliminary design calculations discussed in Section 3 of this report provided the cell dimensions. Each cell has a total wall thickness of 0.85 in., a winding angle of $\pm 45^{\circ}$, and a length of

69 in.. Two layers of two superposed tows of prepreg were required to obtain a part approximately 0.085 in. thick.

5.3.1 Winding Pattern Creation

The helical winding pattern was created using the program FGX. The part diameter was defined as the average between the width and the height of the mandrel since the inner cell cross-section is not circular. The winding pattern was generated so that the individual tows were placed one beside each other during the winding. This reduced the number of crossovers to give a more compact and stiffer part.

5.3.2 Mandrel Coating

One manufacturing problem that was encountered during this study was the sticking of the cured inner cell to the mandrel. This prevented the cured inner cell from being removed from the mandrel. It was found that the combination of a tapered mandrel and a mandrel wrapping of 1/16 in. Teflon film solved this problem.

The film was cut to the desired length (75 in.) and width (10.625 in) and wrapped around the inner cell mandrel. The film was heated with a hot blower to facilitate its application on the mandrel surface. High temperature tape was used to attach the film edges together and to seal the joint as shown in Figure 5.7.

5.3.3 Inner Cell Winding

The leading end of the tow must be taped on the mandrel surface before starting the inner cell winding to ensure that the tows will be pulled during the mandrel rotation. The cell winding was performed at about 50% of the machine speed, see Figure 5.8. During the winding operation, it was ensured that there was enough material on the spools, there was no fiber slipping on the rotating eye rollers, and the fiber was not sliding on the Teflon film. Two layers of 20 minutes duration were required to obtain the desired cell thickness.

5.3.4 Vacuum Bagging and Curing

A vacuum bag was used to apply pressure on the inner cell during its curing at high temperature inside the autoclave. This pressure was required to ensure a good resin flow between the fiber tows. The components of the vacuum bag used for the inner cells were:

- Teflon/Fiberglass porous release film;
- Two layers of breather/bleeder cloth;
- Top and Bottom parts of vacuum port;
- Bagging film;
- Silicone tape;
- High temperature tap.

First, the layer of release film was wrapped around the wound part. Then two layers of bleeder cloth were applied to absorb the extra resin during the cure cycle. The bottom part of the vacuum port was then installed on top of the bleeder cloth. All of the components were taped with high temperature tape. A large piece of bagging film was used to wrap the part and the mandrel completely using the silicone tape. A small hole was made in the bagging film to assemble the top and bottom parts of the vacuum port. The inner cell was cured inside the autoclave under vacuum pressure at the temperature cycle prescribed by the material manufacturer. Figure 5.9 shows two inner cells inside the autoclave ready to cure.

5.3.5 Final Inner Cell Part Preparation

The vacuum bag was cut open after completion of the curing cycle. An opened bag is shown in Figure 5.10. The cured inner cell is then slide off the aluminum mandrel. This was facilitated by the use of a tapered mandrel and the Teflon file. Figure 5.11 shows a finished inner cell next to the filament winder with inner cell mandrel.

5.4 Manufacture of the Outer Shell

The construction of the outer shell of the bridge presents two basic problems. First, the cross-section is further removed from the ideal circular shape than the inn cells. The

relatively high width to depth ratio creates a problem with the creation of the winding pattern using the FGX computer program, since this software assumes that the part has a circular cross-section. Thus there will be a difference between the predicted and the actual winding angles. The winding process is further complicated by the tendency of the fiber to slip at each end of the outer shell because the winding angle is low and the shell is thick. Second, the gap between the outer shell and the inner cells shown in Figure 5.12 complicates the curing process. It is essentially to be able to apply pressure during the cure cycle to the unsupported portion of the outer shell that is located over this gap. This is necessary to ensure adequate resin flow during cure so that voids are eliminated form the final part and to ensure that the outer shell is flat.

These two issues were solved using the techniques described in the remainder of this section so that several two and six cell bridges could be manufactured.

5.4.1 Inner Cell Location

The first task during the manufacture of the outer shell manufacture is to install the required number of outer cells on the support tooling described in the previous section. Figure 5.13 shows the support tooling at one end of the bridge prior to the location of the inner cells; note the application of the Teflon film around the inner cell support blocks. This film was required to ensure a tight fit of the inner cells over these support blocks. Figure 5.14 shows six inner cells located on the outer shell support tooling prior to the winding of the outer shell.

Durng the course of this research project, various gaps were introduced between the inner cells on some of the two cell configurations. This is documented in subsequent sections. These gaps were accommodated by using the adjustment provided through the slots in the outer cell support tooling. When a gap of zero size was required (i.e., when the inner cells were positioned to contact their neighbor – the most common approach adopted in this study), the sides of each cell were sanded to remove any surface imperfections. The edges of the inner cells were then bonded together using a five minute epoxy glue.

5.4.2 Expanding Foam Application

After the inner cells had been positioned in the support tooling, an expanding foam material was applied in the gap between the outer shell and the cells to provide support for the outer shell fibers during cure. This expanding foam offers a cheap, light and easy to apply material to fill the gap. In addition, the foam resists relatively high temperatures (up to a maximum of 120°C).

Figure 5.15 shows this foam being sprayed over the whole length of the inner cells. After the foam had been applied, an aluminum plate coated with a Teflon film was used to apply pressure to the foam as shown in Figure 5.15. This pressure aids in producing a flatter foam surface. The foam was then trimmed and sanded; Figure 5.16 shows a six cell bridge after the application of all of the expanding foam.

5.4.3 Winding of the Outer Shell

The outer shell can be wound after the expanding foam has been applied to fill the gap between the inner cells and the outer shell. The outer shell requires three layers of two-tow thick material in order to obtain the desired shell thickness of 0.125 in. Figure 5.17 and 5.18 show the winding of a two cell bridge with an outer shell angle of ±30° and a six cell bridge with an outer shell angle of ±45°, respectively. The winding time is approximately 45 minutes and 2 hours per layer for the two cell and six cell bridges for a machine speed of 50 %, respectively.

5.4.4 Vacuum Bagging and Curing

After the outer shell has been wound, the entire bridge superstructure was placed in a vacuum bag and cured in the autoclave. The composition of the vacuum bag was similar to that used during the manufacture of the inner cell.

Two aluminum plates were placed between the bleeder and breather layers as shown in Figures 5.19 and 5.20. These plates were used to apply a pressure during cure over the top and bottom surfaces of the bridge so that these surfaces remained flat. Two and four vacuum ports were used in the bags of the two and six cell bridges, respectively. After the vacuum bag had been installed, the bridge was placed inside the autoclave for curing (see Figures 5.21 and 5.22 for the two and six cell bridges, respectively.

The outer shell was cured in a similar manner to the inner cells: inside the autoclave under a specified temperature cycle and vacuum pressure. A different curing cycle was designed because the recommended curing temperature exceeded the maximum foam temperature. The objective of this modification was to gel the resin at a lower temperature (110°C) before the complete curing at 155 °C as shown in Figure 5.23. This modified curing cycle required a total time of five hours.

5.4.5 Final Outer Shell Preparation

After the curing cycle was complete, the vacuum bag was cut and removed from the bridge to produce the parts shown in Figures 5.24 and 5.25. The final step involved trimming the ends of the cured part. A completed six cell bridge is shown in Figures 5.26.

Temperature (Degree F) / (degree C)	Time (Hour)
270 / 135	4
290 / 145	2
310 / 155	1

Table 5.1: Manufacturer's recommended cure temperature and hold time for E-glass/epoxy prepreg.

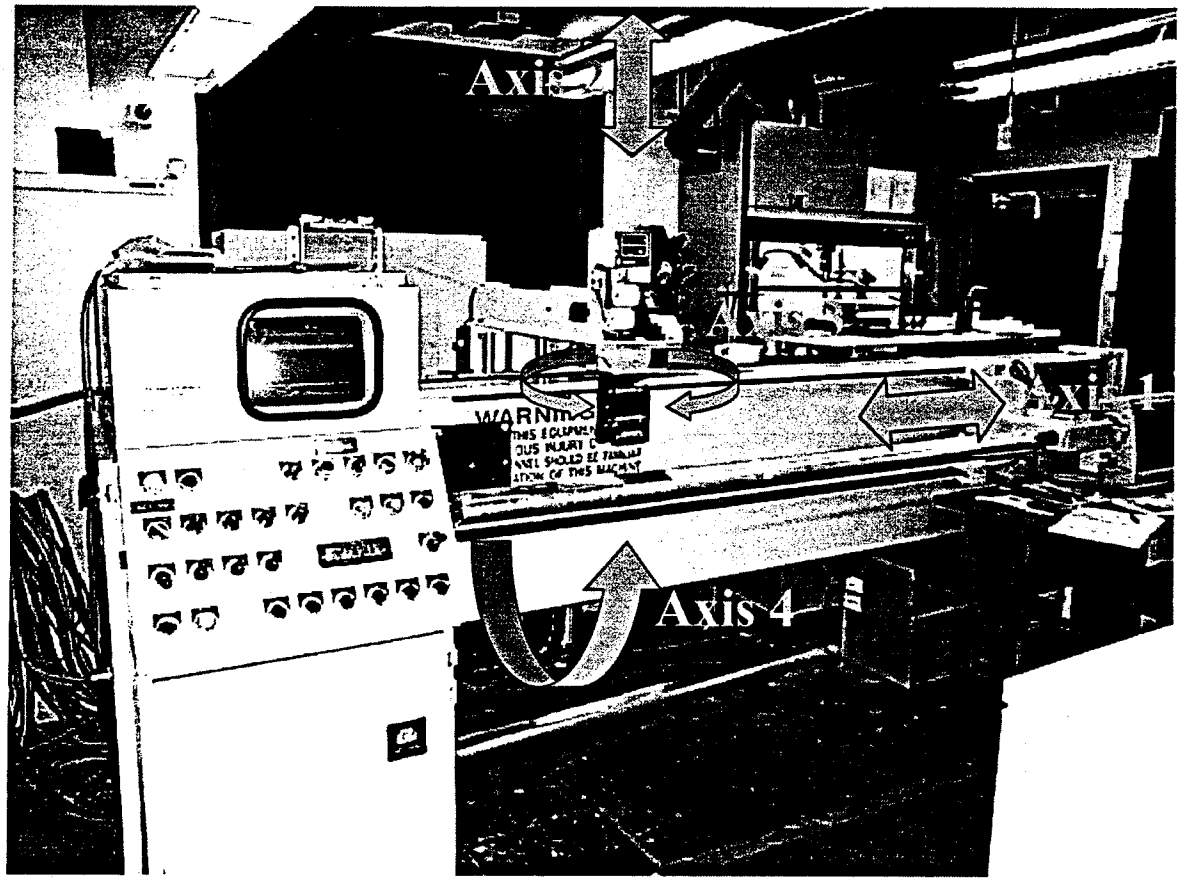

Figure 5.1: The En-Tec four axis filament winder employed in this study.

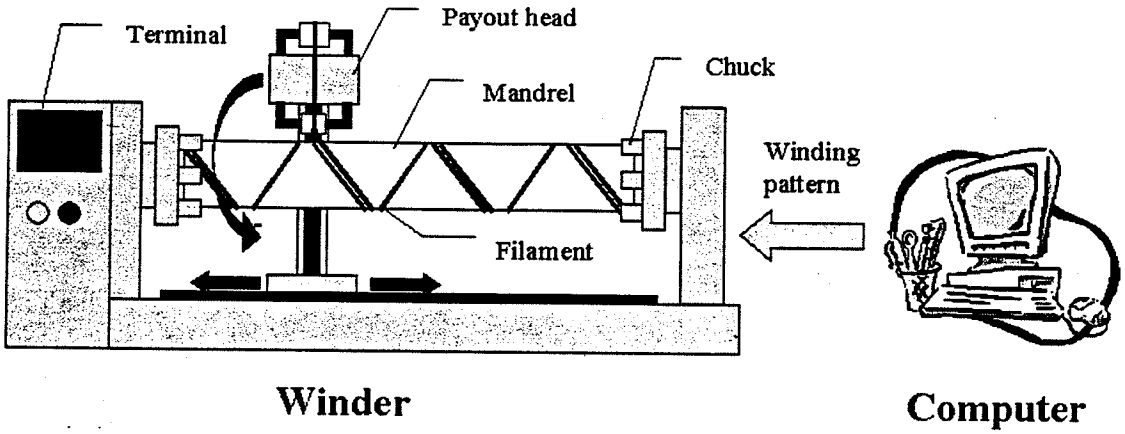

Figure 5.2: Schematic representation of the filament winder.

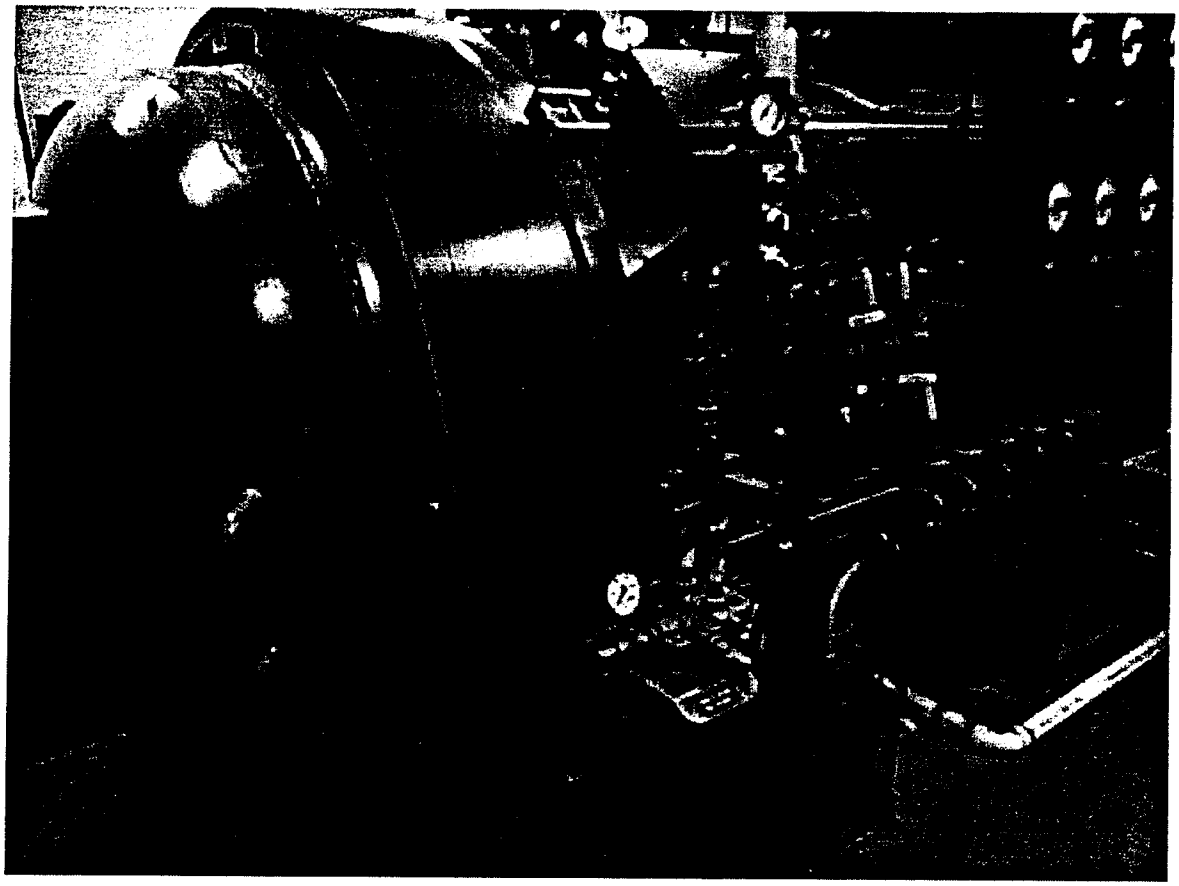

Figure 5.3: The autoclave employed in this study.

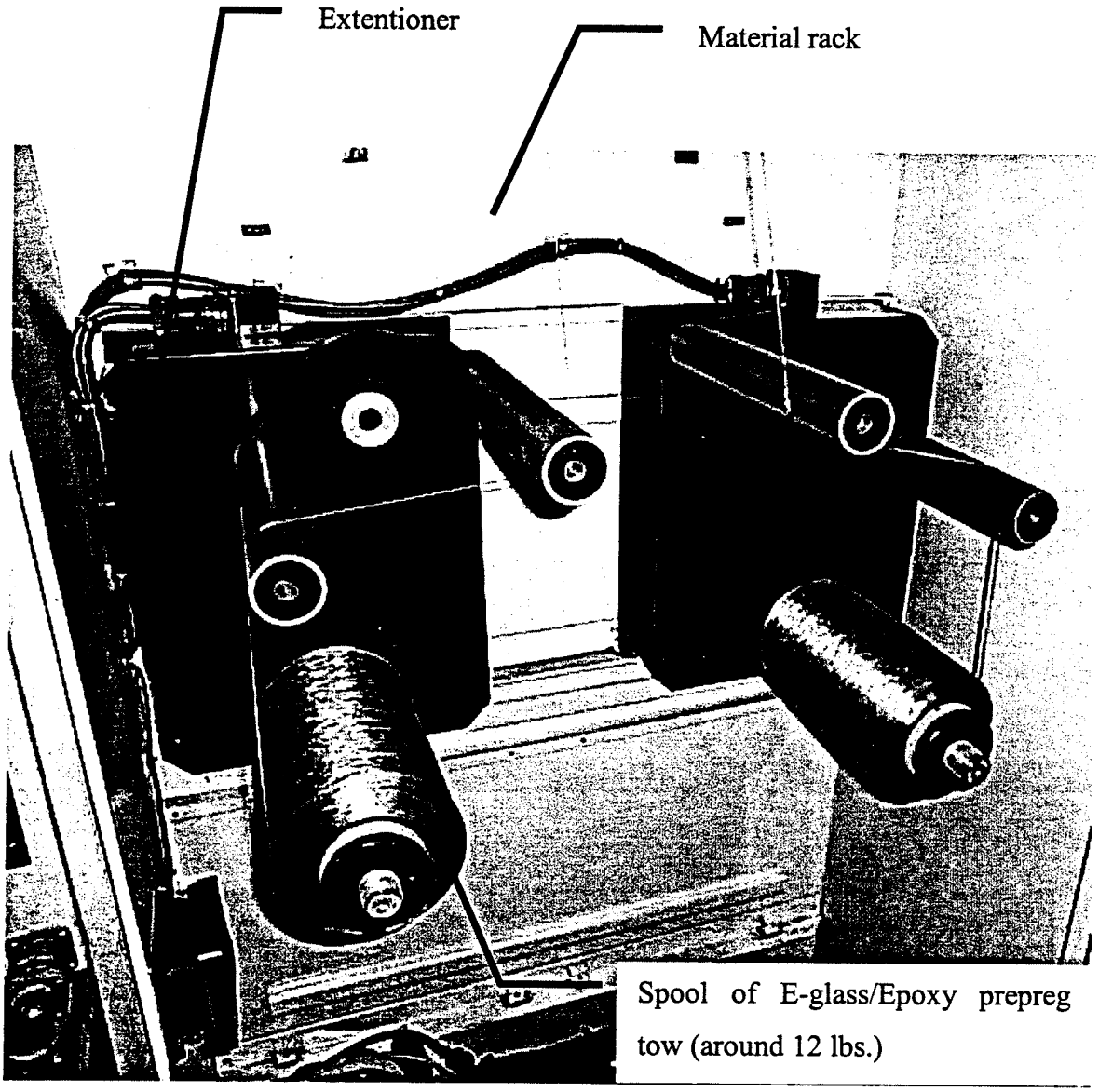

Figure 5.4: Installation of the FRP composite material spools on the rack.

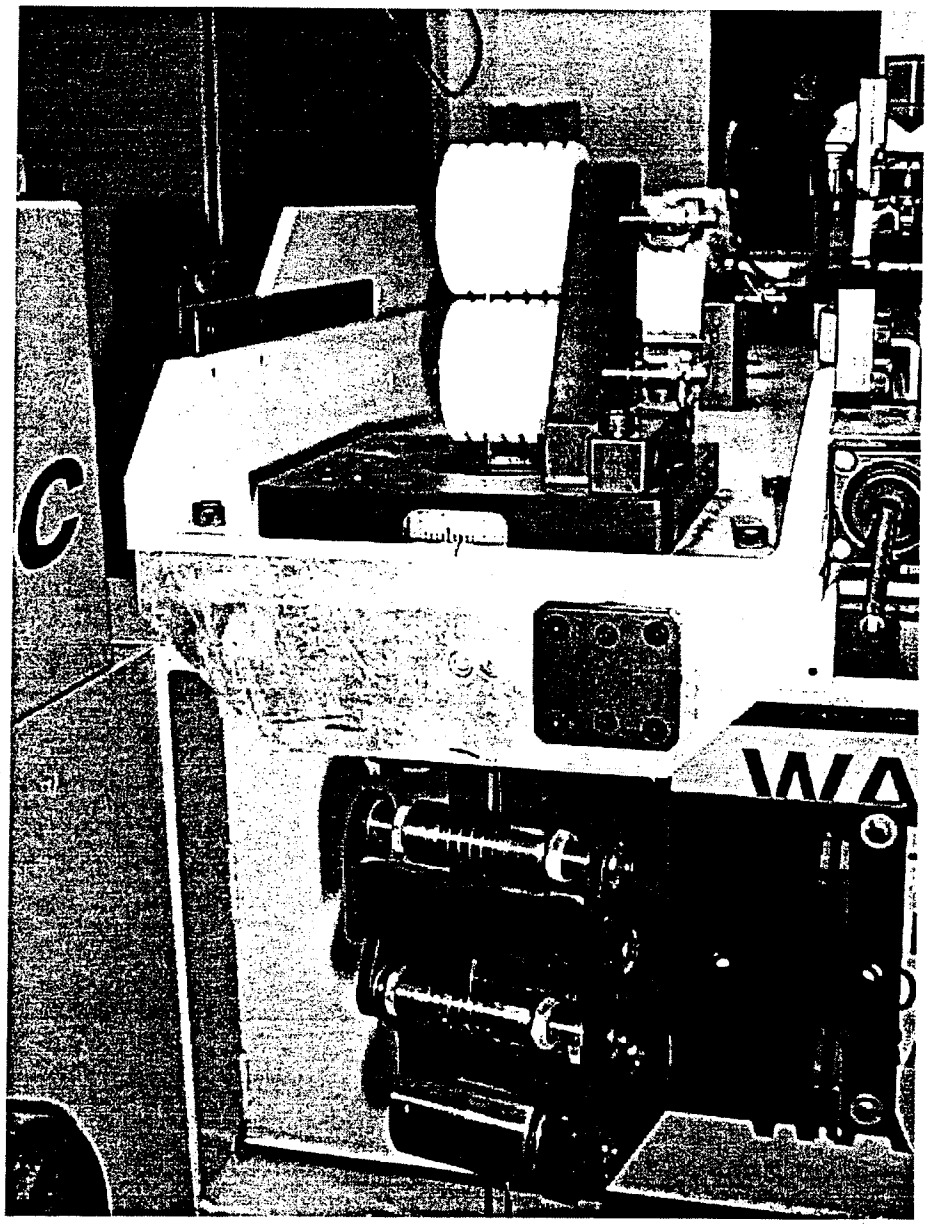

Figure 5.5: Prepreg winding configuration for the payout head.

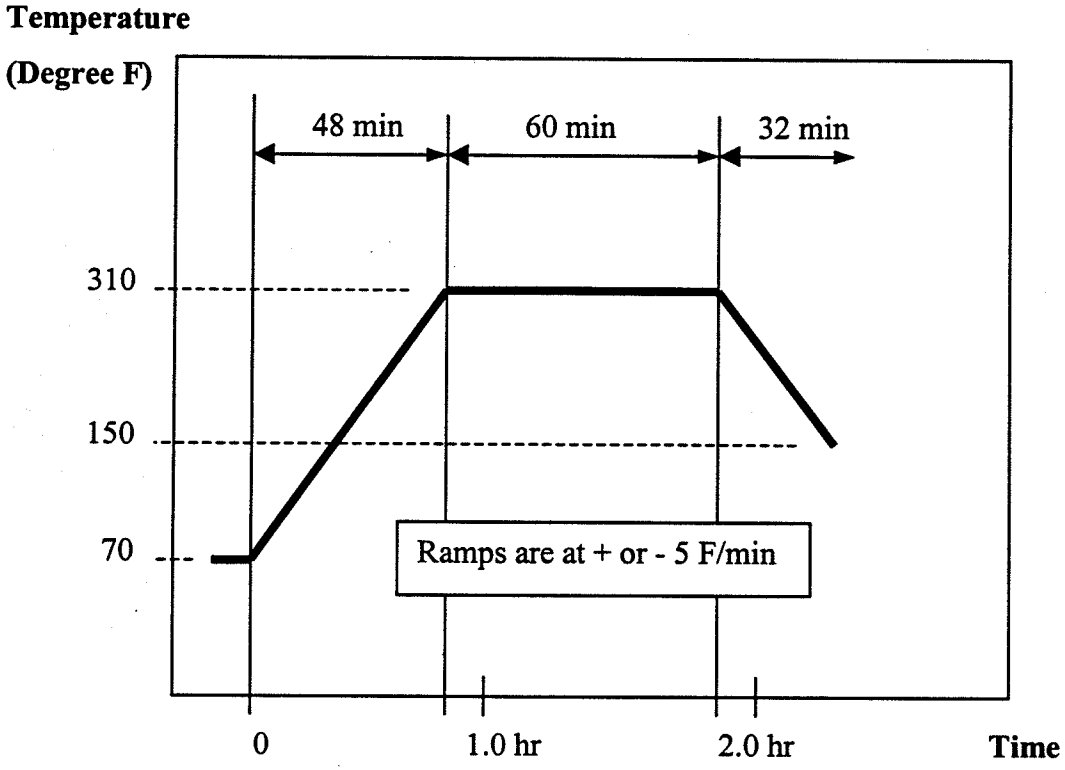

Figure 5.6: Manufacturer's recommended cure profile for E-glass/epoxy prepreg.

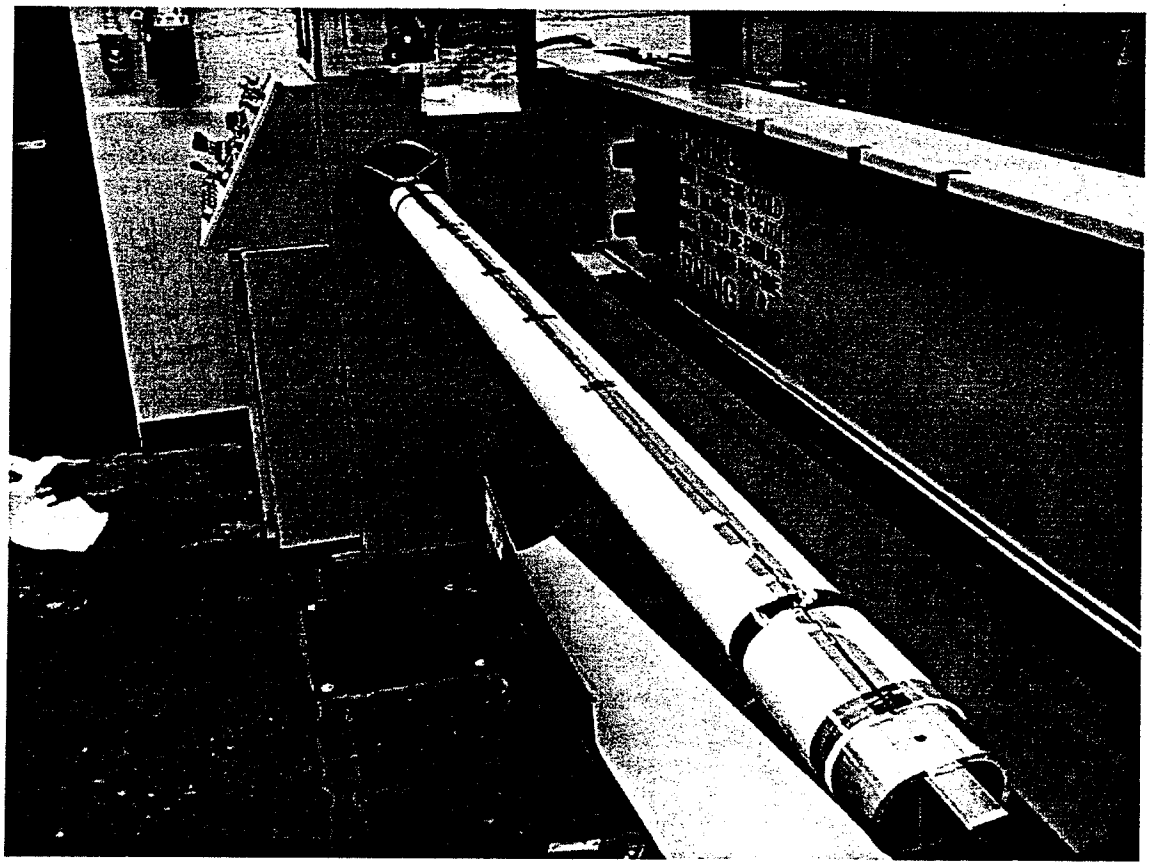

Figure 5.7: Inner cell mandrel with Teflon film installed on the filament winder.

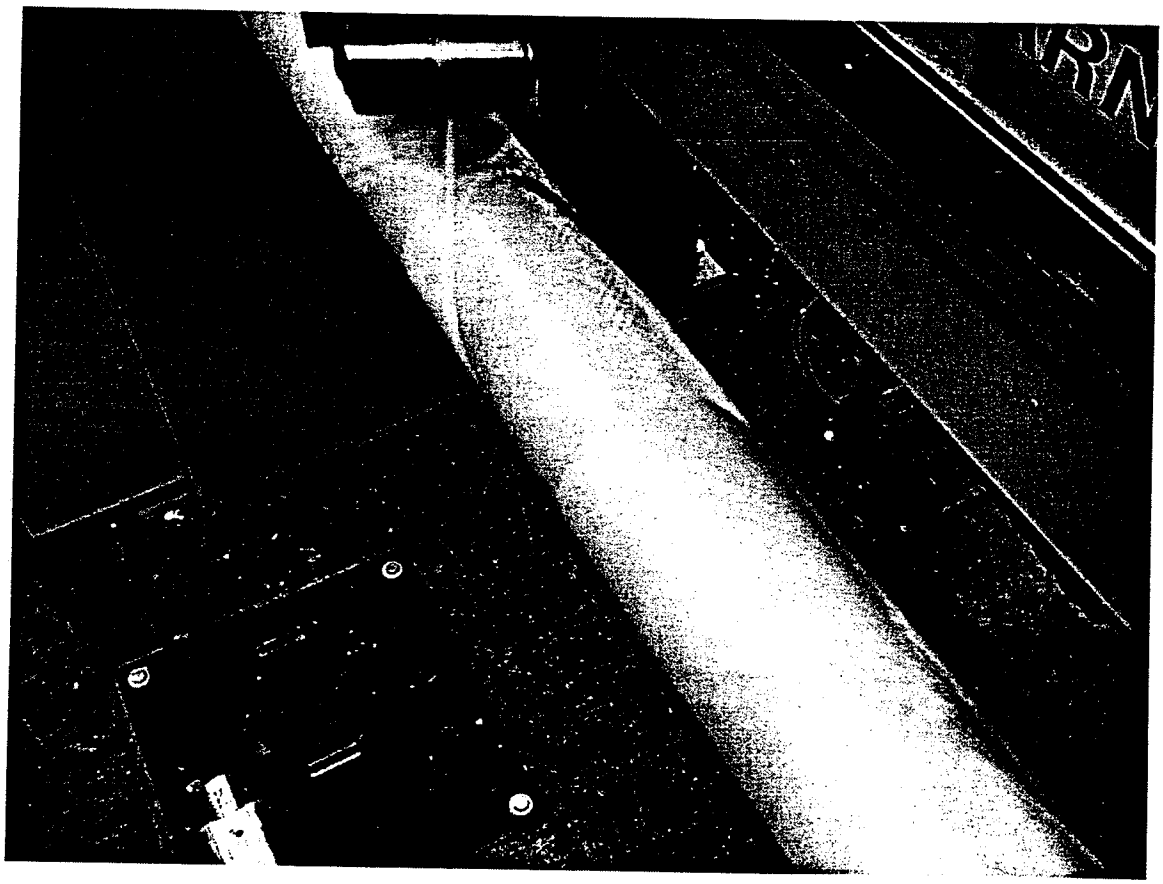

Figure 5.8: Manufacture of an inner cell at a winding angle of ±45°.

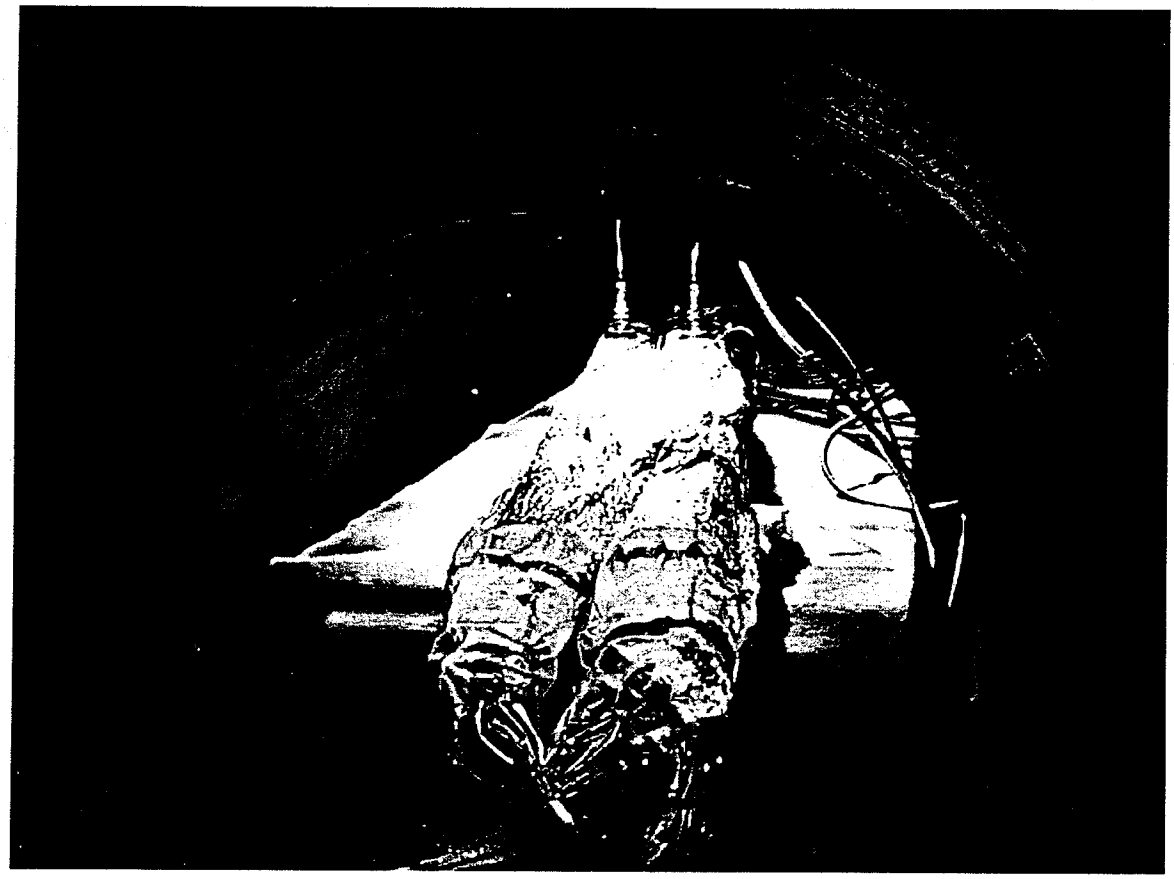

Figure 5.9: Two inner cells inside vacuum bags in the autoclave prior to curing.

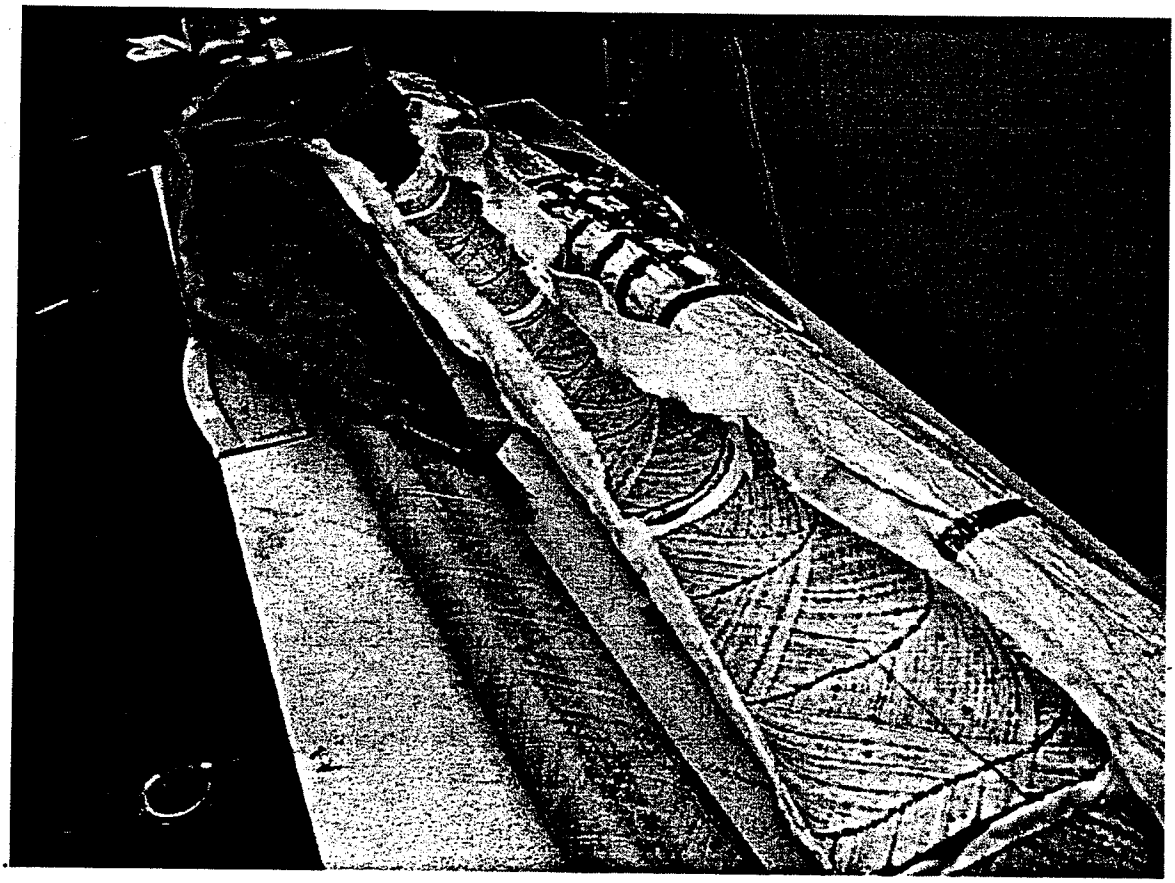

Figure 5.10: Inner cell on mandrel and opended vacuum bag after curing in the autoclave.

Figure 5.11: Cured inner cell after removal from the mandrel.

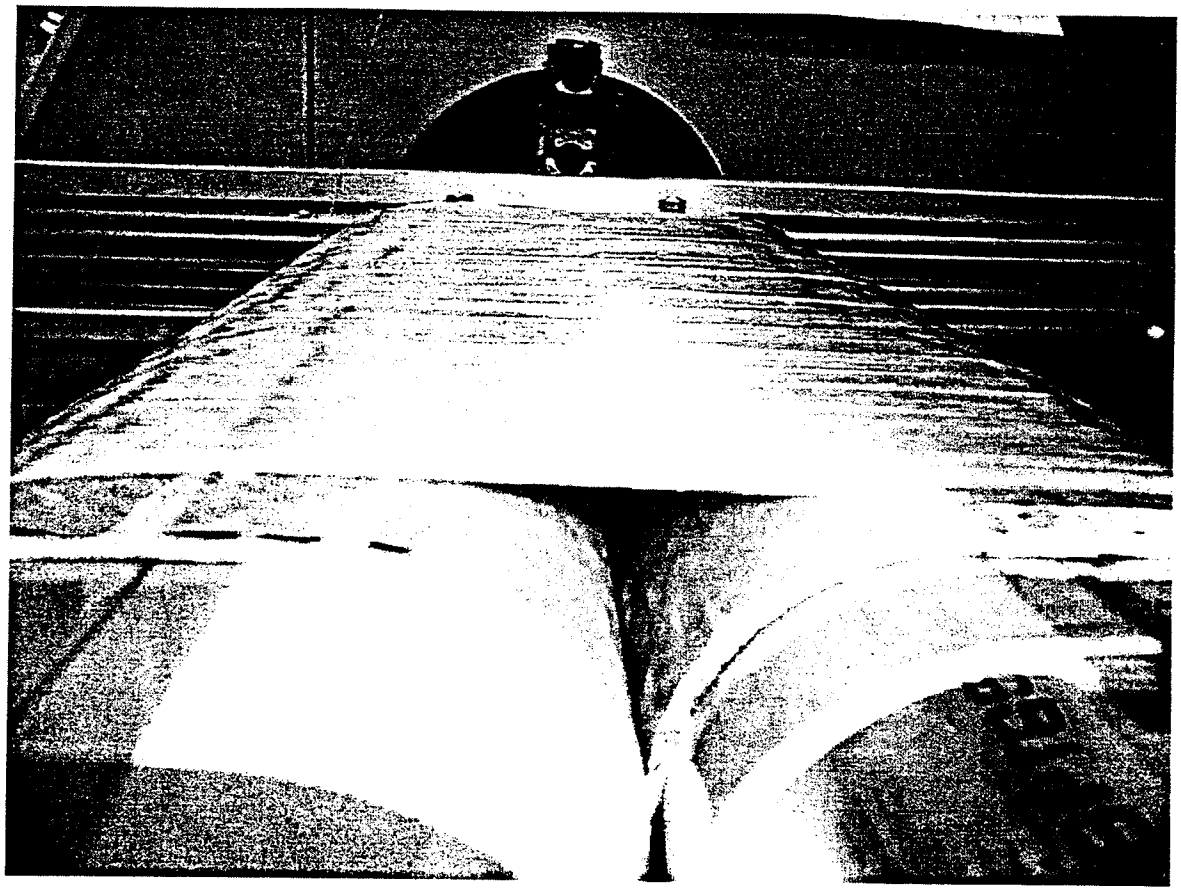

Figure 5.12: Gap between the outer shell and the inner cells.

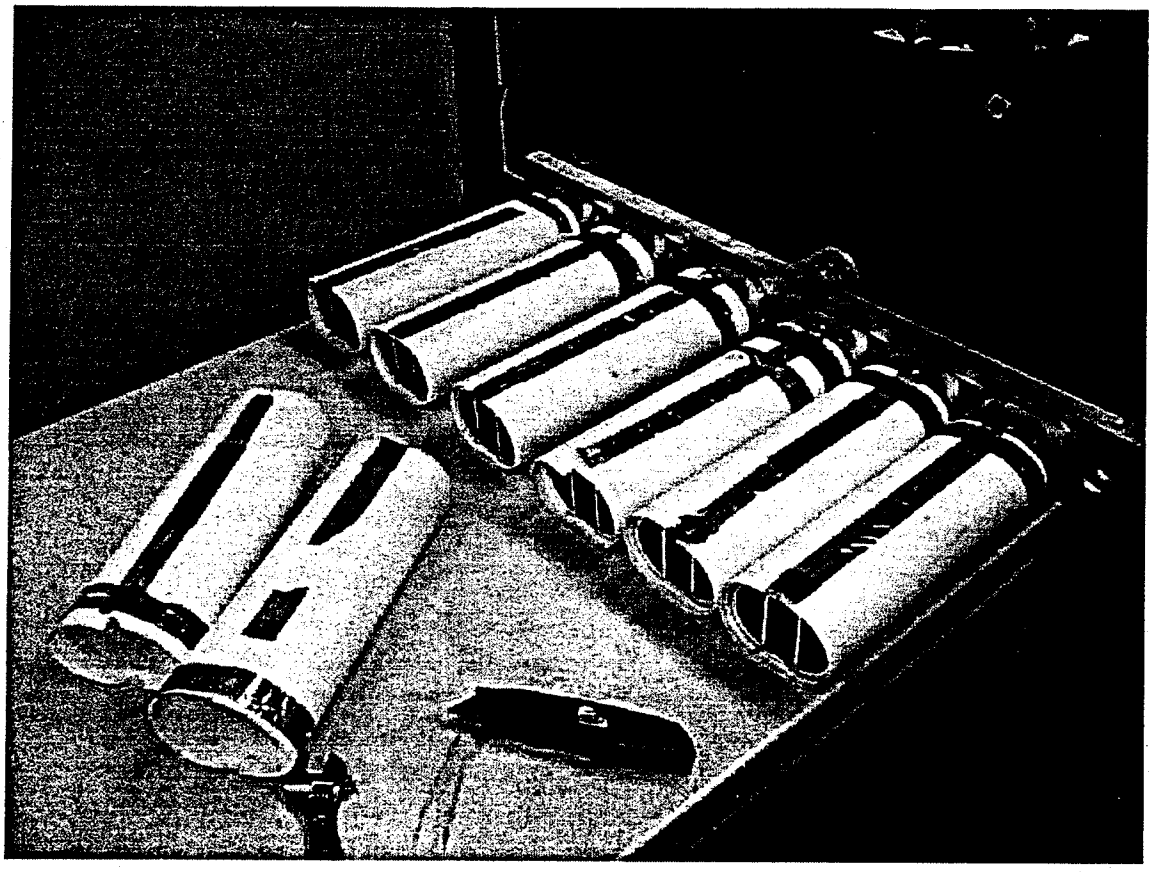

Figure 5.13: Support tooling used for the outer cell winding of a six cell bridge.

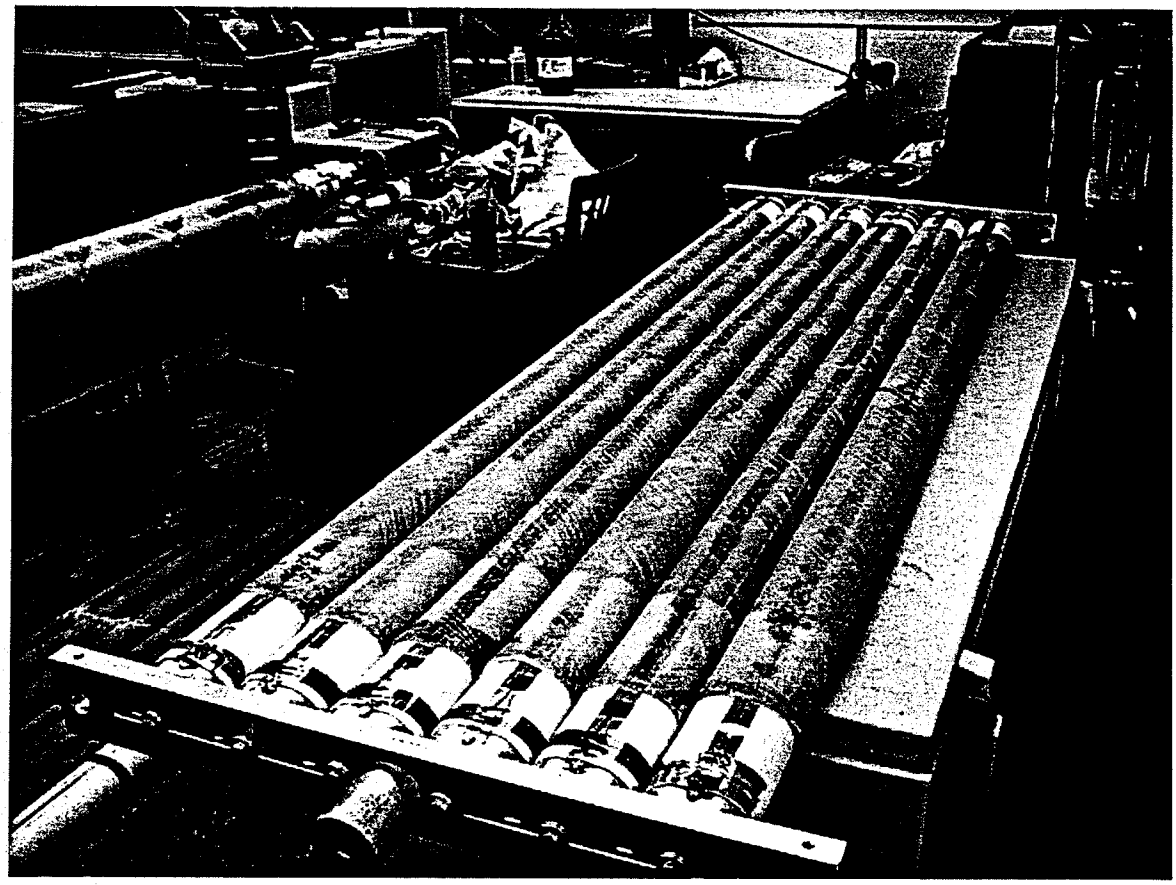

Figure 5.14: Inner cell location for the outer shell winding of a six cell bridge.

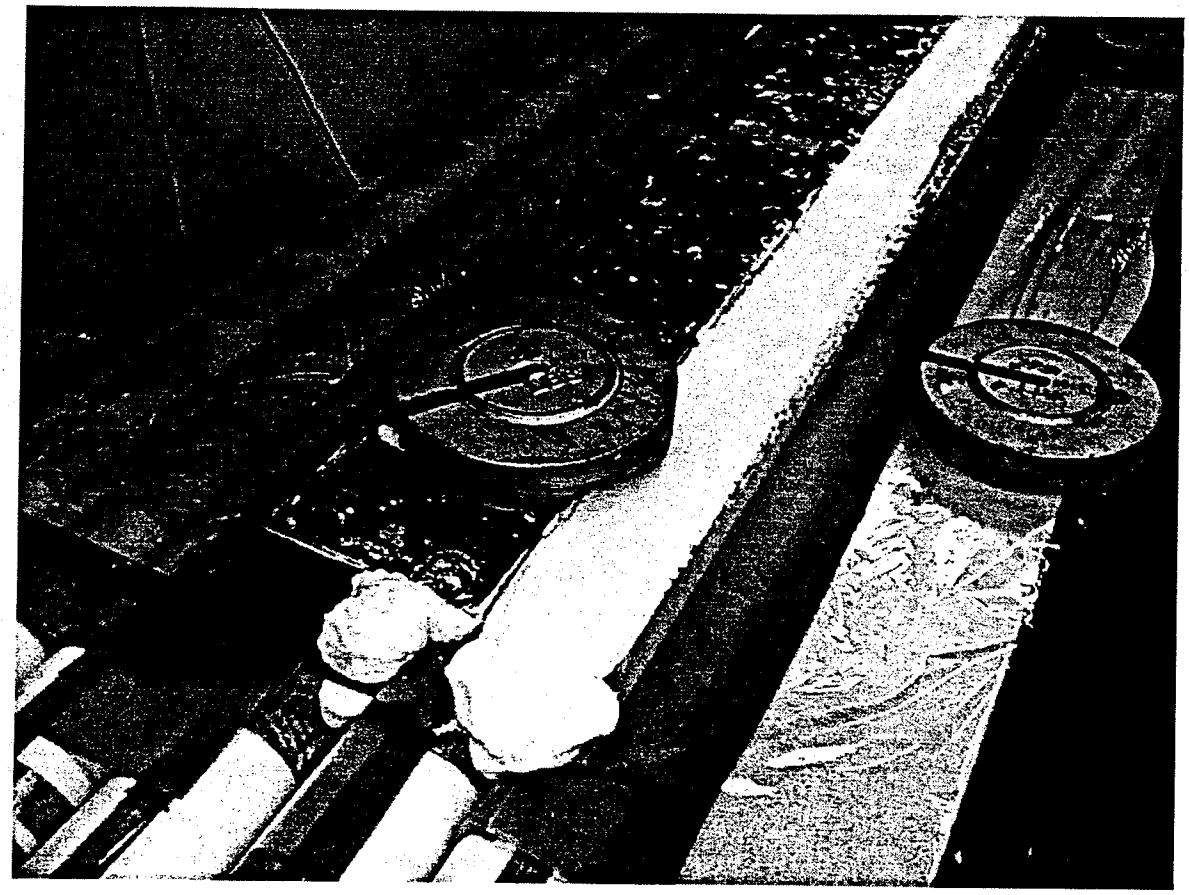

Figure 5.15: Application of the expanding foam.

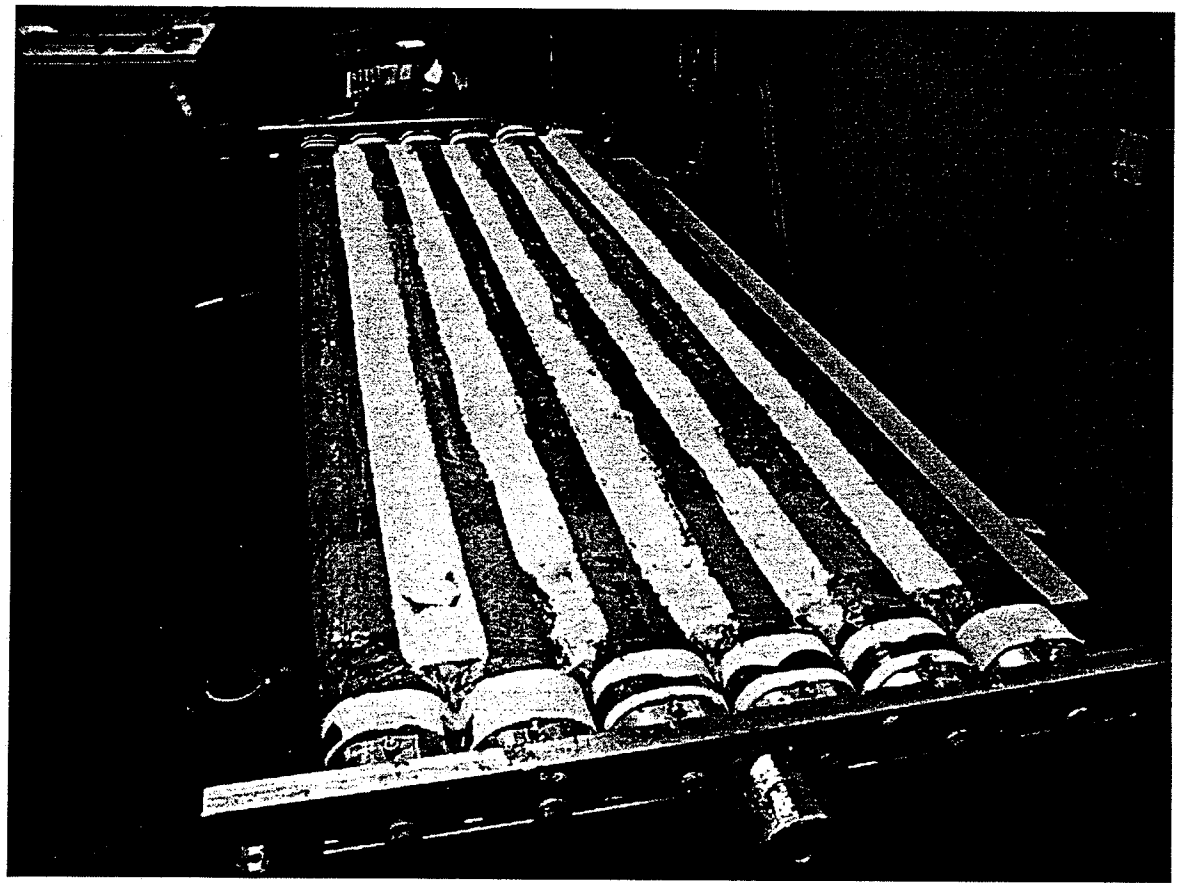

Figure 5.16: Expanding foam after trimming.

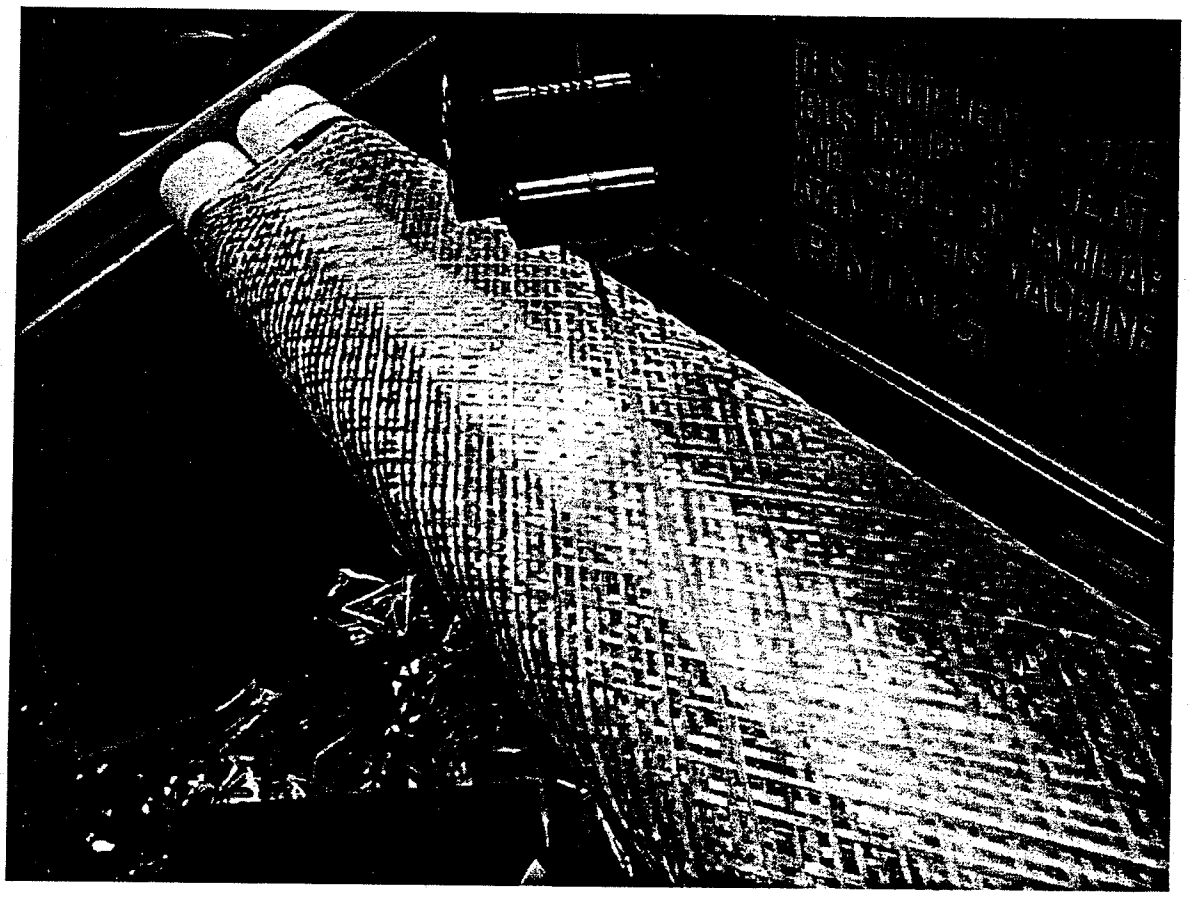

Figure 5.17: Winding of the outer shell for a two cell bridge at an angle of ±30°.

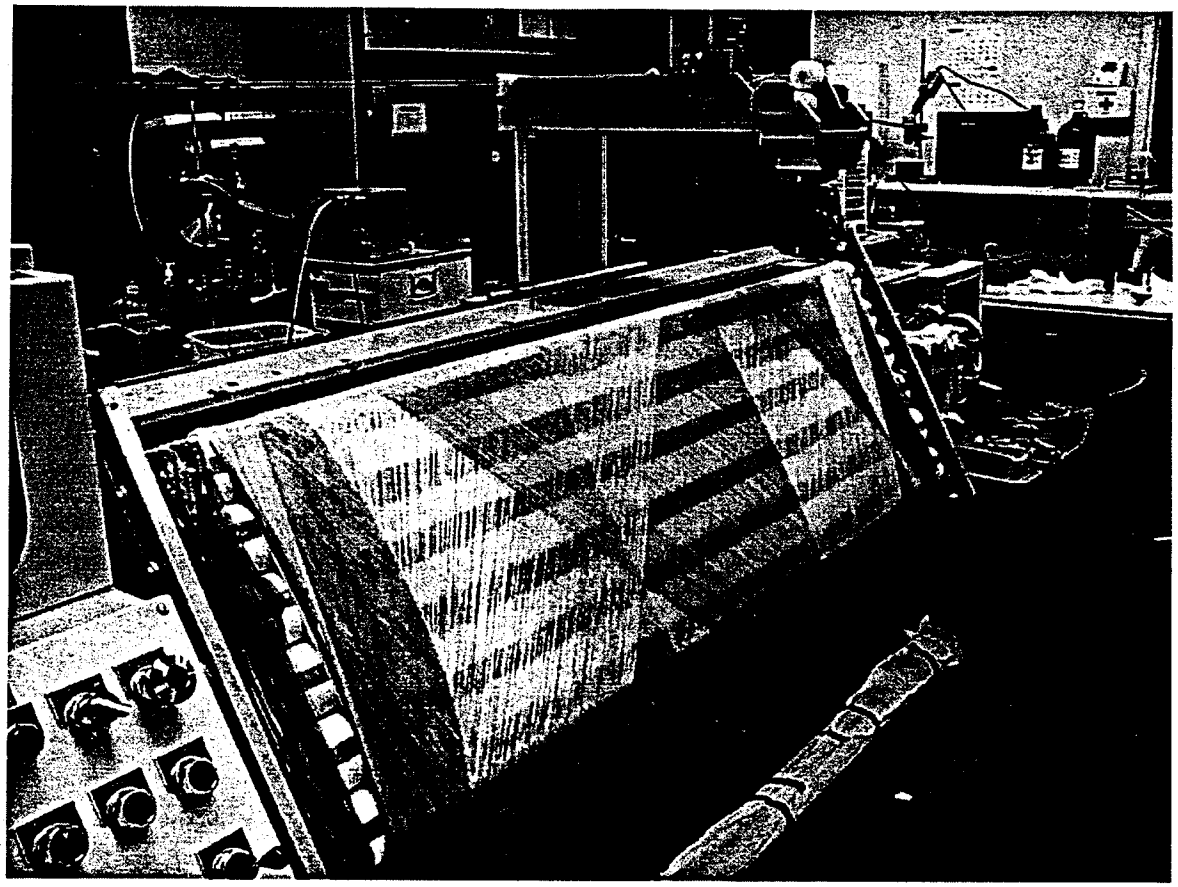

Figure 5.18: Winding of the outer shell for a six cell bridge at an angle of ±45°.

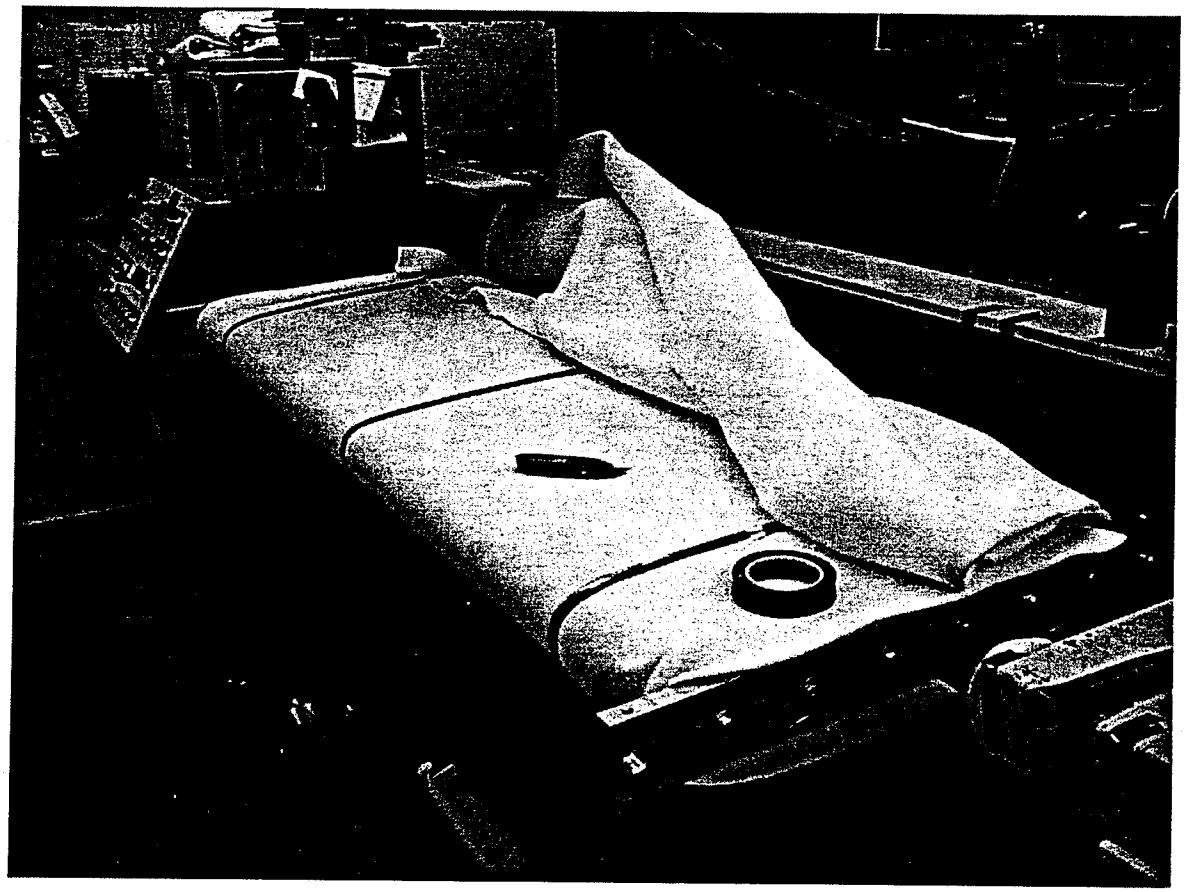

Figure 5.19: Vacuum bag assembly before the insertion of the aluminum plates.

Figure 5.20: Vacuum bag assembly after the insertion of the aluminum plates.

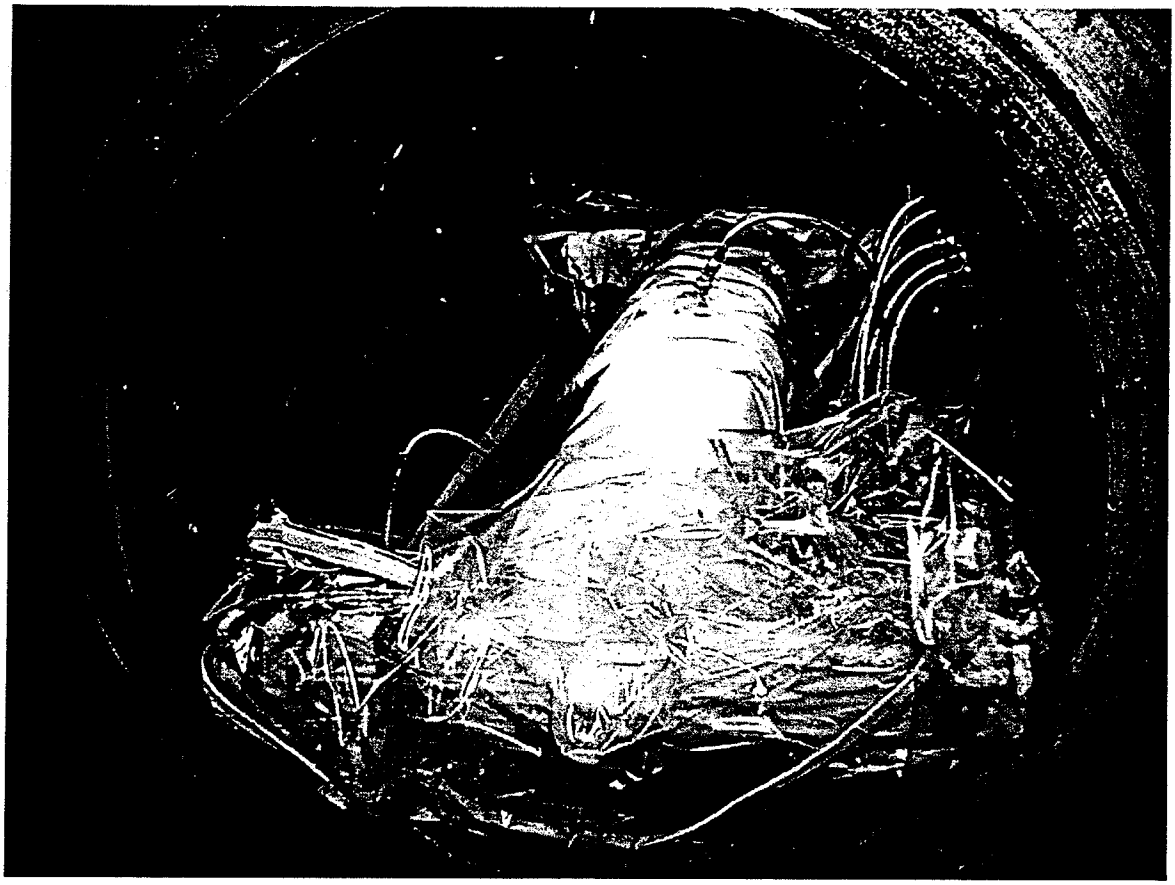

Figure 5.21: Two cell bridge inside the autoclave after complete assembly of the vacuum bag.

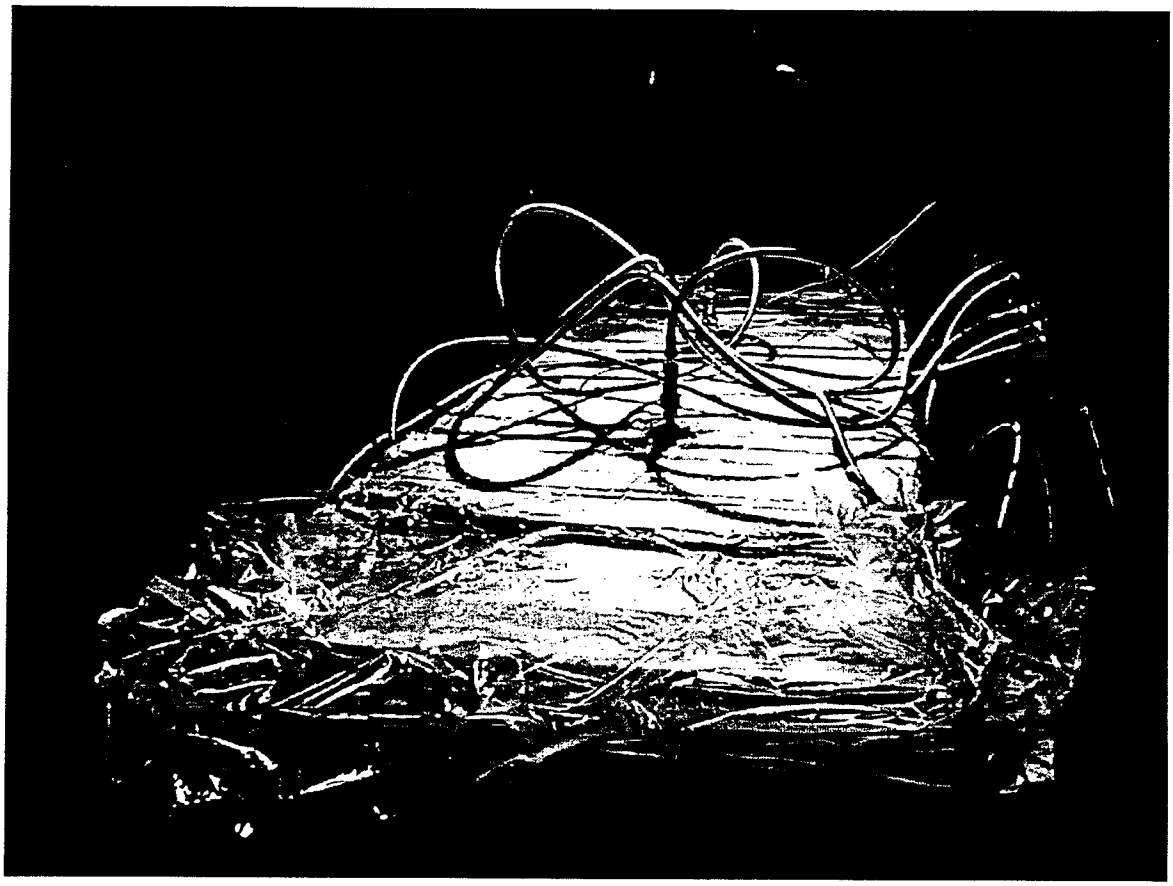

Figure 5.22: Six cell bridge inside the autoclave after complete assembly of the vacuum bag.

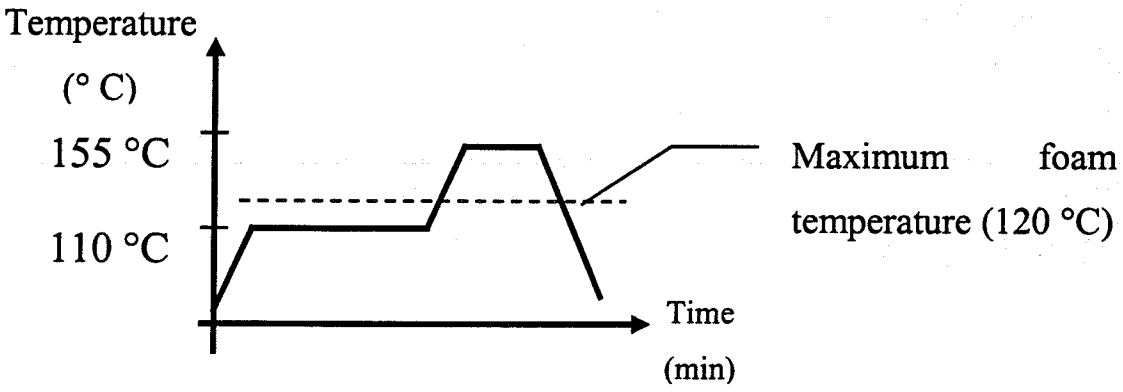

Figure 5.23: Modified curing cycle employed during the manufacture of the outer shell.

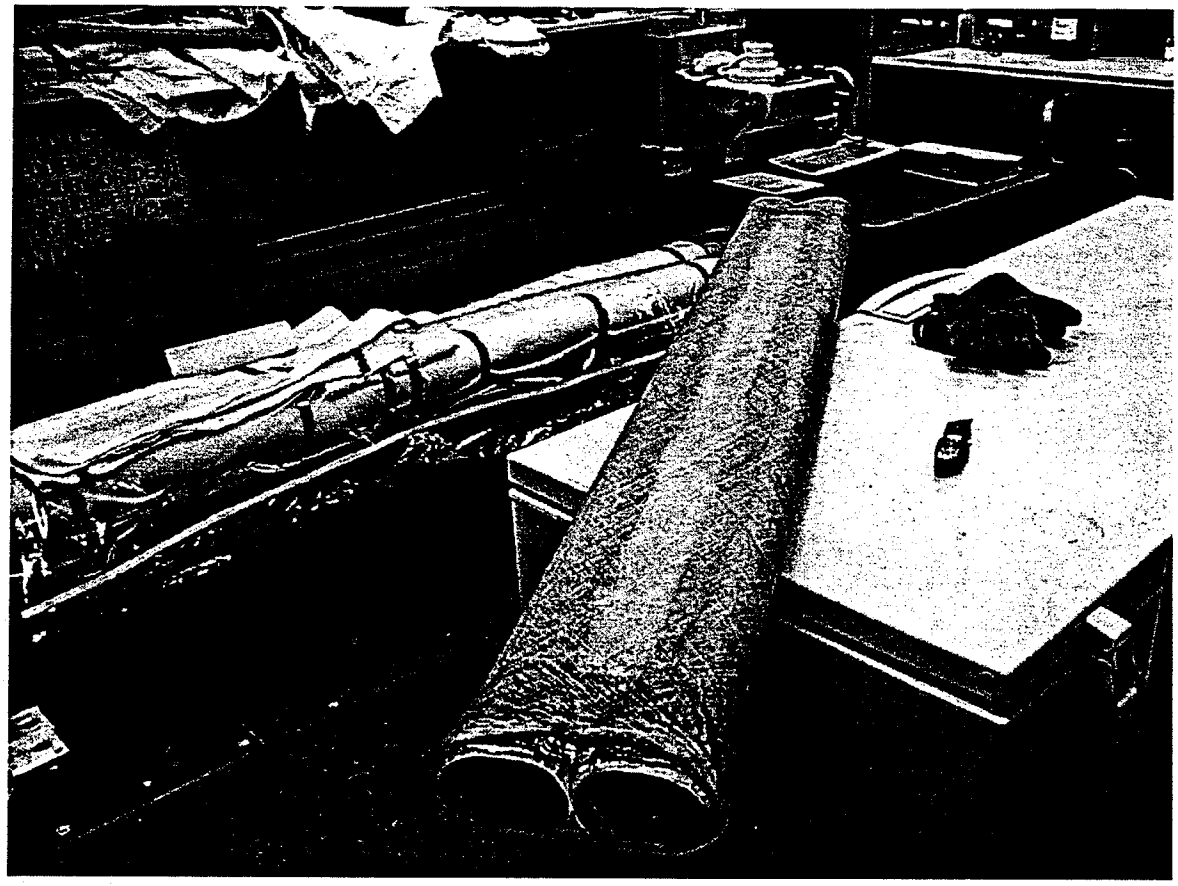

Figure 5.24: Two cell bridge after outer shell curing.

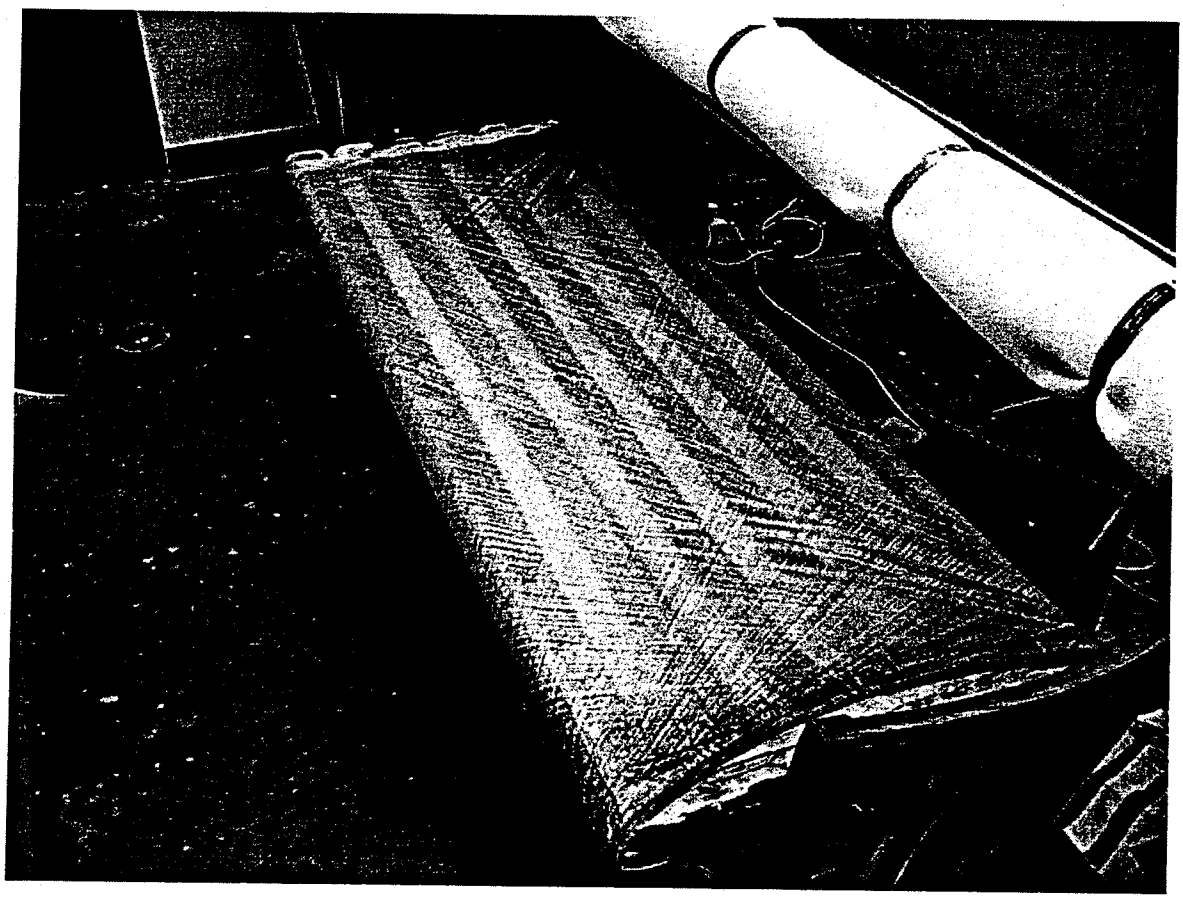

Figure 5.25: Six cell bridge after outer shell curing.

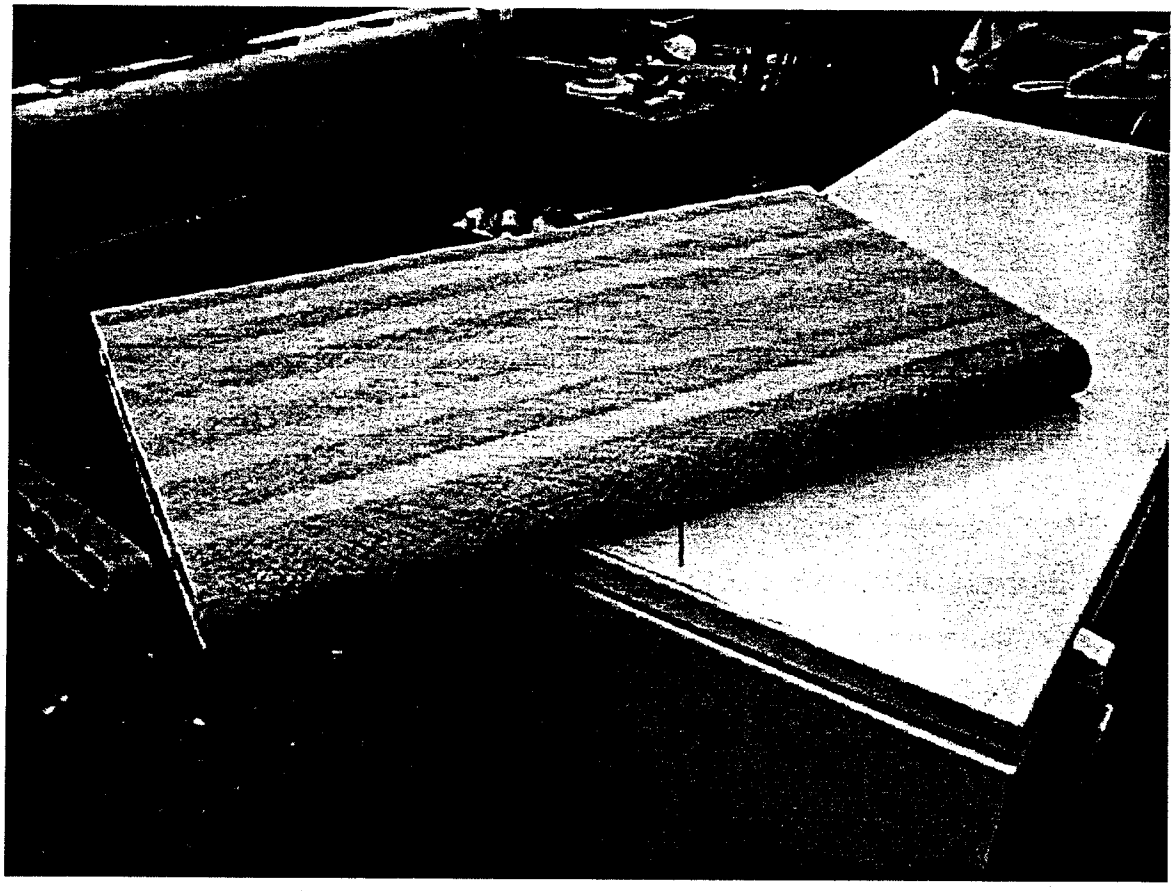

Figure 5.26: Final six cell bridge.

6. Experimental Equipment

This section describes the experimental equipment that was used to test the prototype filament wound bridges. Structural testing of the superstructure prototypes was performed to determine their strength and stiffness as well as their fatigue strength. The bridge strength is characterized by the first ply failure (FPF) of the composite. The same basic testing configuration was used for both the two cell and the six cell bridges.

6.1 Test Configuration

The three point bending configuration was chosen to represent typical bridge superstructure loadings. No attempt was made to scale the standard design loadings with the physical dimensions of the small scale prototypes; instead a uniform load was applied over a steel plate located at the center of the span of the bridges. This provided sufficient information to both assess the structural performance of the manufactured prototypes and investigate the validity of finite element models of the bridges.

6.2 Test Equipment

Figures 6.1 and 6.2 show diagrams of the test equipment employed. The main components of the setup are similar for the two and six cell bridge tests. A 20 kips capacity tensile machine applied the load through a square steel plate (4 in. x 4 in. x 0.5 in.). The ends of the bridge were placed on two 4 in. diameter steel circular rollers to produce the required simply-supported end conditions. Two 10 ft. long steel I-beams were placed on the base plate of the testing machine; the circular rollers were fixed to these I-beams to prevent any motion of the roller supports. A computer was used to manage the data acquisition system.

6.2.1 Two Cell Bridge Test

Figure 6.3 shows a photograph of the specific arrangement used to test the two cell bridges. During these tests, only the applied load and vertical displacement of the actuator were measured.

6.2.2 *Six Cell Bridge Test*

Figures 6.4 and 6.5 show the testing configuration employed for the six cell bridges. In addition to the applied load and vertical deflection of the actuator, 4 LVDT's and 14 strain gauges were used to record the deformation of the specimen. Figure 6.6 shows the location of these transducers on the top and bottom surfaces of the bridge.

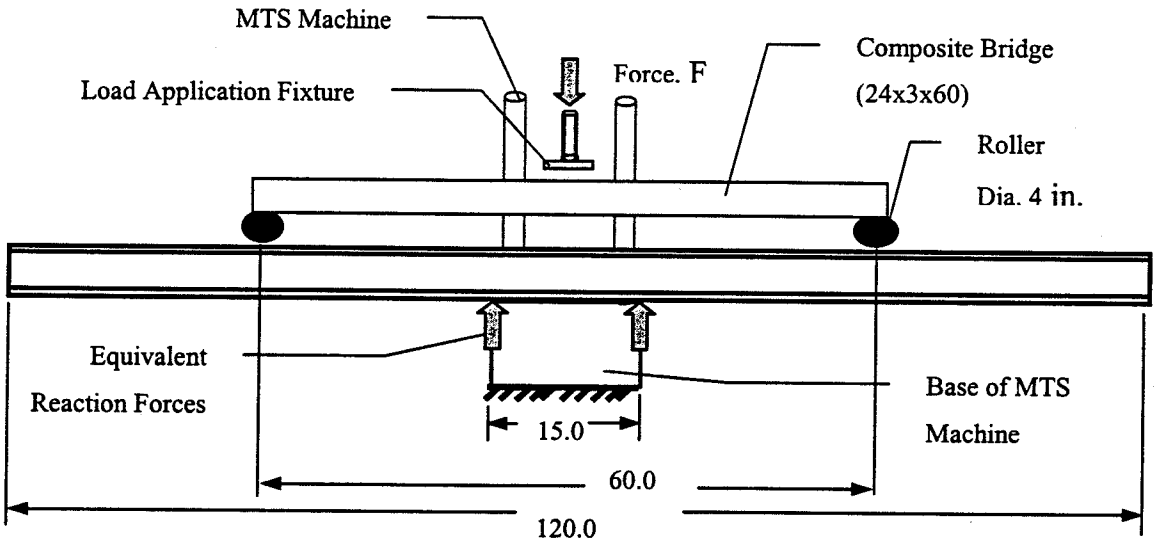

Figure 6.1: Side view of the experimental apparatus.

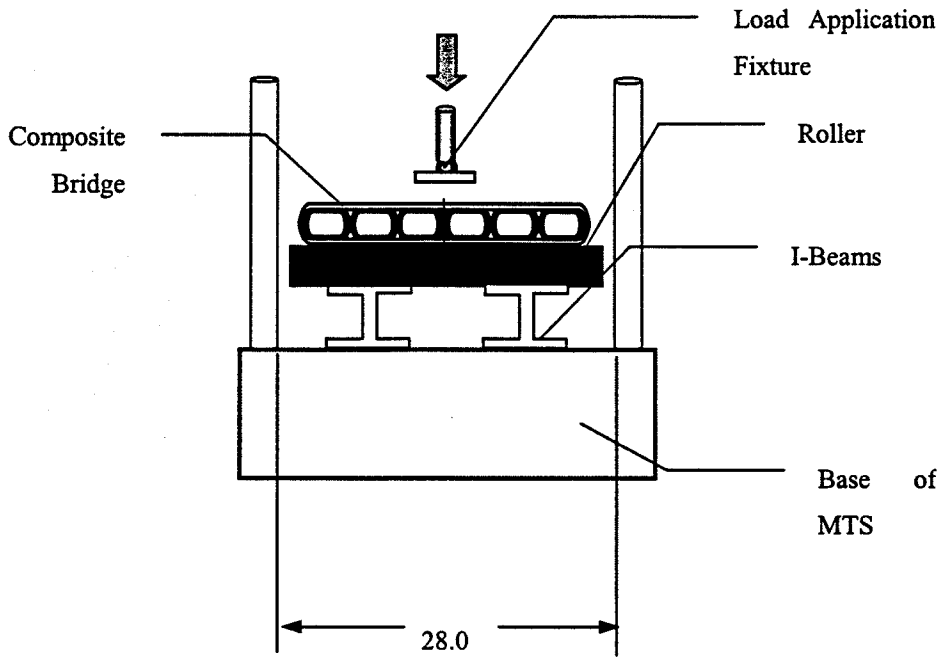

Figure 6.2: Front view of the experimental apparatus.

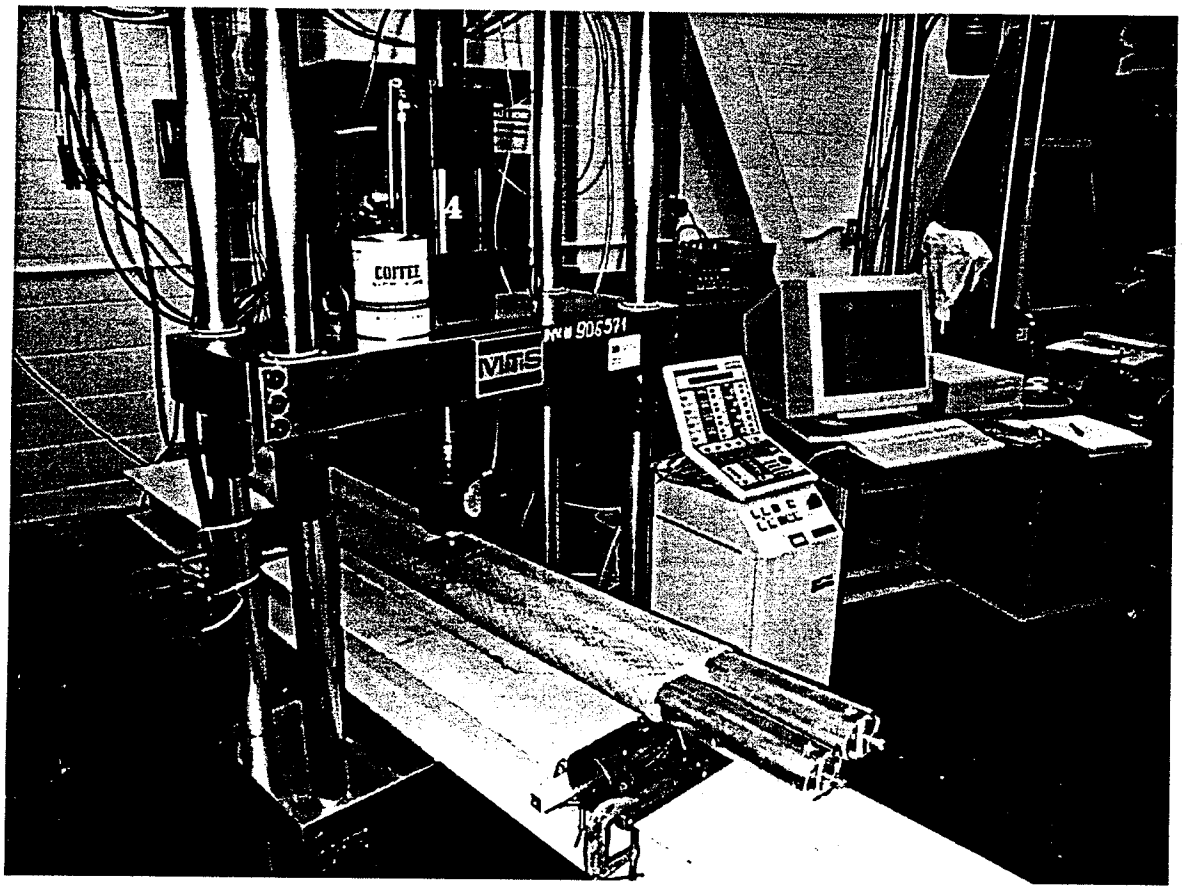

Figure 6.3: Test setup for a two cell bridge.

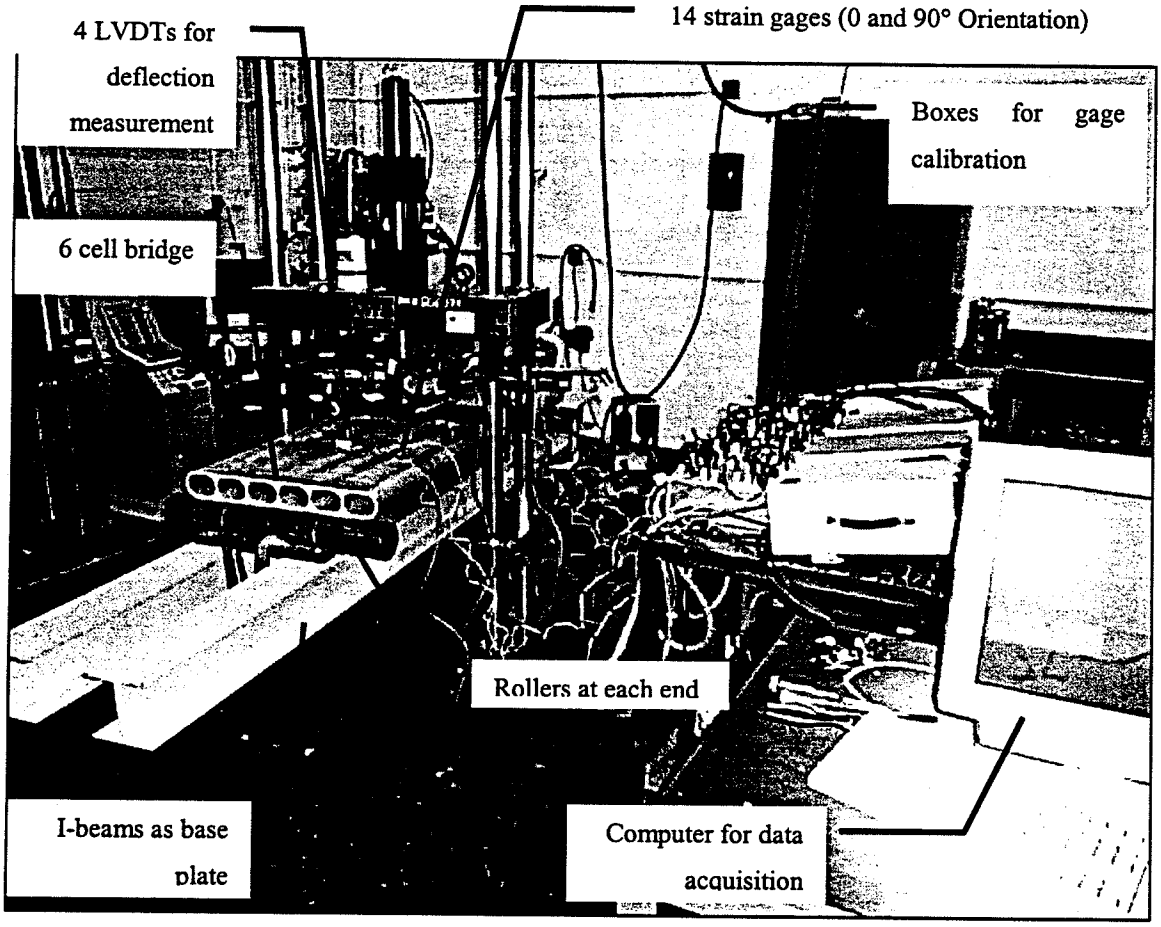

Figure 6.4: Test setup for a six cell bridge.

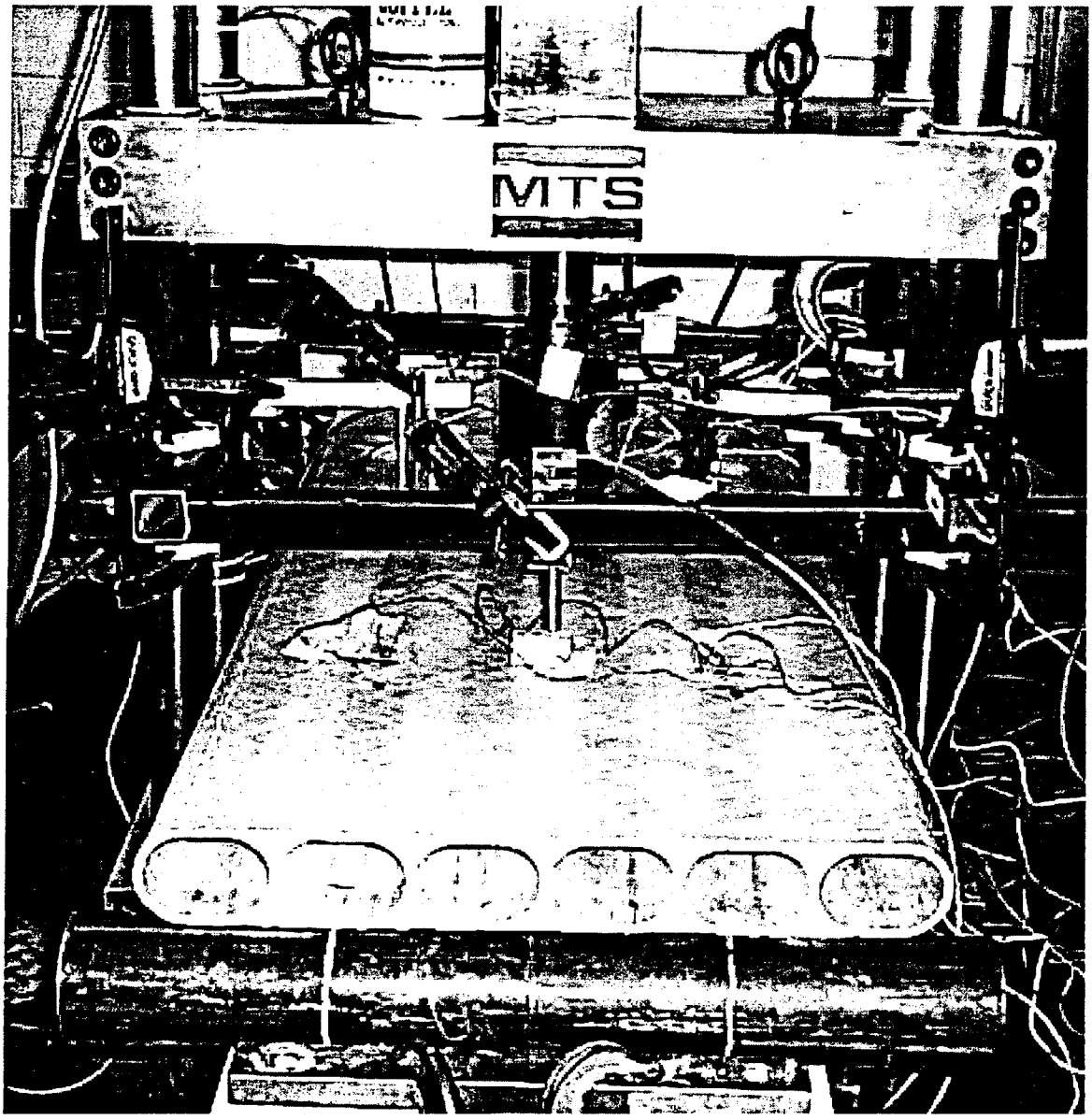

Figure 6.5: Front view of the test setup for a six cell bridge.

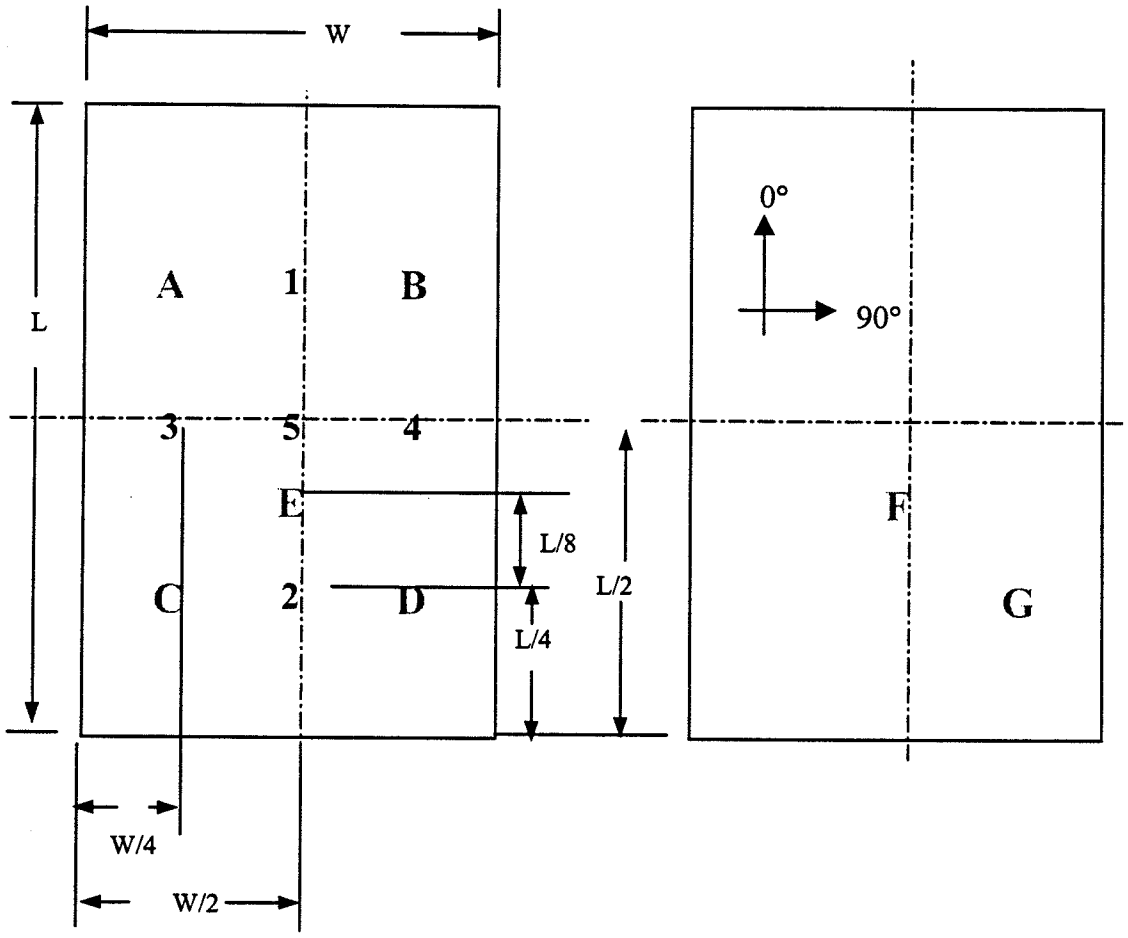

TOP VIEW **BOTTOM VIEW**

Legend:

1: Location of LVDT (North)

2: Location of LVDT (South)

3: Location of LVDT (West)

4: Location of LVDT (East)

5: Location of LVDT (Actuator)

A to G: Location of Strain Gages

L: Length of Bridge

W: Width of Bridge

Figure 6.6: Location of LVDT's and strain gauges on the six cell bridge.

7. Results of the Experimental Tests

This section presents the data obtained by testing the various prototype bridges that were manufactured using the procedures documented in Section 5. The testing equipment and instrumentation were discussed in Section 6. Two categories of bridges were tested: two cell and six cell bridges. Various configurations were examined within these two categories to explore the structural properties of the general design. The objectives of the tests were to measure the stiffness and strength of the different specimens, and, in the case of a six cell bridge, to investigate the fatigue life of the structure. The measured data were used to assess the behavior of the structural system and to investigate the validity of finite element models of the prototypes.

7.1 Two Cell Bridges

7.1.1 Specimen Description

A total of five two cell bridges, each 51 in. long, were manufactured and tested. These specimens were used to check the integrity of the manufacturing process and the experimental equipment. Table 7.1 lists the characteristics of these bridges. The first four bridges (bridges A, B, C and D) were constructed entirely of glass fiber reinforced polymer wound at ±45°. The inner cells of bridges A and D were placed so that there was no gap between them. Bridges B and C were constructed with gaps of $\frac{3}{16}$ in. and $\frac{1}{16}$ in., respectively, between the inner cells. This was done to investigate the additional stiffness provided by inner cell contact. Bridge E was manufactured with inner cells composed of carbon fiber reinforced polymer wound at ±45° and an outer shell composed of glass fiber reinforced polymer wound at ±45°. This specimen served to examine the feasibility of varying the materials used to change the stiffness, strength and cost of the bridge. Bridge A was tested with aluminum inserts placed inside the ends of the inner cells, see Figure 7.1. This was done to determine whether it was necessary to provide support to the ends of the inner cells in order to develop the full stiffness of the structural system. All of the other bridges were tested without these inserts, as shown in Figure 7.2 for bridge D.

7.1.2 Experimental Procedure

Only the actuator displacement and the applied load were measured during the tests of the two cell bridges. The bridges were simply supported by rollers located ½ in. from the ends of the specimen. Thus the distance between the end supports was 50 in. Each specimen was positioned so that the load was applied in the center of the span. In order to remove any looseness from the testing equipment and to verify the functioning of the instrumentation, two loading cycles were conducted up to a load of 1,500 lbs. (corresponding to an actuator deflection of about ½ in.). These initial loading cycles were well within the elastic range of the specimens. The load was then increased until the bridge failed. Initial failure of the specimen was indentified by either the first big crack or the first load drop. When the bridge had been completely broken, the load was removed and the data acquisition stopped.

7.1.3 Experimental Results

Figure 7.3 shows plots of the measured applied load versus actuator displacement for the five two cell bridges. Table 7.2 lists the observed failure loads and stiffness of each specimen. The stiffnesses were obtained by measuring the slopes of the actuator load-deflection curves within their linear ranges between applied load levels of 1,000 lbs. and 2,000 lbs. The failure mode of all of the two cell bridges was the development of cracks parallel to the fibers in the compressive side of the outer shell near the load application region as shown in Figure 7.4 for bridge D. These cracks were followed by localized buckling of the outer layers of the outer shell. Figure 7.5 shows the final state of bridge A. These large deformations were representative of the final state of the other two cell bridges. When the load was removed, the bridges all returned to almost perfectly straight structures.

7.1.4 Discussion of Results

Comparison of the measured data for bridges A and D indicate that placing rigid supports at the ends of the inner cell has little effect. The stiffness differed by 5%, and the measured load-deflection behavior was similar. These observations are within a reasonable estimate of the repeatability of the manufacturing process and cannot be

attributed to the different end conditions. No deformation was observed at the ends for either of these specimens, further indicating that the rigid supports had no measurable effect on the behavior of the bridges. The data obtained for the four glass bridges (i.e., bridges A, B, C and D demonstrate that providing contact between the inner cells by setting the gap size to 0 produces an increase in stiffness. The use of carbon fiber inner cells in bridge E results in a stiffer structure, as was expected, but is accompanied by a reduction in strength, which was unexpected.

7.2 Six Cell Bridges

7.2.1 Specimen Description

A total of four six cell bridges were manufactured and tested using the procedures documented in this report. Table 7.3 lists the characteristics of these bridges. The first three bridges (i.e., bridges #1, #2 and #3, see Table 7.3) were manufactured entirely out of glass fiber reinforced plastic. Bridges #4 and#5 were manufactured to investigate the performance of hybrid material systems: bridge #4 was composed of glass fiber inner cells and a hybrid carbon and glass fiber outer shell (using three layers of equal thickness, with a carbon layer between the two glass layers), whereas bridge #5 was composed of carbon fiber inner cells and a glass fiber outer shell. In all cases, the inner cells were placed so that there was contact between adjacent cells.

The objectives of the tests were to measure the stiffness and strength of the different specimens. Bridge #3 was constructed to investigate its structural performance under fatigue loading.

7.2.2 Experimental Procedure

The apparatus used for the tests of the six cell bridges is shown in Figure 7.6 and is very similar to the apparatus used to test the two cell bridges. However, more measurements were taken during the tests as described in Section 6, namely:

1. The deflections measured by the four LVDTs;
2. The displacement of the actuator;
3. The load applied by the actuator;
4. The strain measured by 14 strain gages.

The bridges were simply supported by the long steel rollers located 0.5 in. from each end of the bridge.

The testing protocol employed for the six cell bridges was the same as that used for the two cell bridges. Three load cycles are used to measure the stiffness of the bridge. The first two cycles deformed the bridge in its elastic range by applying a load that increased monotonically from 0 to 1,500 lbs. These two cycles were applied to eliminate any looseness in the testing equipment. On the third load cycle, the specimen was loaded until failure. A different set of loads were applied to bridge #3, since the objective of the test on this bridge was to investigate its fatigue properties. This loading protocol is described in the section below that presents the results of the fatigue test.

7.2.3 Experimental Results for the Glass Bridges

Two all-glass bridges were tested: bridges #1 and #2. This section presents the observations and measured data obtained from these tests.

7.2.3.1 Bridge #1

Figure 7.7 shows plots of load versus displacements measured at the actuator and the four LVDT's for bridge #1. Early in the loading, there was some light cracking sounds and some debonding at the shell-cell interface (see Figure 7.8). A loud cracking sound was heard at an applied load of about 2 kips. This was accompanied by the appearance of cracks near the load application region as shown in Figure 7.9. Debonding between the inner cells and the outer shell became visible at a load of about 3 kips, see Figure 7.10. The bridge fails at a load of about 9 kips; this failure is due to the development of large deflections and cracks in the compression side of the bridge near the load application regions as shown in Figure 7.11.

7.2.3.2 Bridge #2

Figure 7.12 shows plots of load versus displacements measured at the actuator and the four LVDT's for bridge #2. No cracking sounds or debonding at the cell-shell interface were observed during the first 2 loading cycles (Figure 7.13).

The first load cracking sound (accompanied by a small drop in the applied load) occurred at a load of approximately 2.6 kips. The first visible cracks appeared near the load application zone on the top surface of the bridge is shown in Figure 7.14. Failure of the specimen occurred at a load of 7.8 kips; as with bridge #1, this was a compression failure of the outer shell near the load application region. Figre 7.15 shows the state of the bridge at the collapse load.

7.2.4 Experimental Results for the Glass-Carbon Bridges

Two hybrid glass-carbon bridges were tested: bridges #4 and #5. This section presents the observations and measured data obtained from these tests.

7.2.4.1 Bridge #4

Figure 7.16 shows plots of load versus displacements measured at the actuator and the four LVDT's for bridge #4. Manufacturing defects were visible in this specimen before the test was conducted. Figure 7.17 shows a crack that was observed inside one of the inner cells. During the first load cycle, some cracking sounds were heard at a load of about 800 lbs. A louder cracking sound was heard at a load of 1.4 kips during the final load cycle. The first visible cracks are shown in Figure 7.18 and are located farther from the load application zone compared to the cracks observed in bridges #1 and #2. At higher loads, the inner cells experience significant deformation and cracking, see Figure 7.19. The top surface of the bridge experiences significant deformation as shown in Figure 7.20. Complete failure of the bridge occurs at a load if 5.2 kips and is accompanied by cracks in the top surface, see Figure 7.21.

7.2.4.2 Bridge #5

Figure 7.22 shows the load-displacement plots obtained during the test of bridge #5. Figure 7.23 shows the testing configuration for this specimen. As with bridge #4, manufacturing defects were present prior to the test; Figure 7.24 shows longitundinal cracks that were observed inside the carbon-epoxy inner cells. No cracking noises were heard during the first two loads cycles. During the final load cycle, minor cracking sounds were heard at a load of 2,200 lbs. A major cracking noise was heard at 2,600 lbs. Crack were observed on the top surface of the outer shell at a load of 2,900 lbs. Figure

7.25 shows the deformation experienced by the inner cells near the load application region during the application of the load. Figure 7.26 shows the crack that developed on the surface of the outer shell. Complete collapse of the bridge occurred at a load of about 5 kips.

7.2.5 Experimental Results for the Glass Bridge Fatigue Test

Bridge #3 was built to the same specifications as bridge #2 (see Table 7.3), and was used to examine the performance of the proposed bridge design under fatigue loads. Once again, the bridge was simply-supported at end using the long steel rollers as seen in Figure 7.27. However, the rollers were located at 1.0 in. for each end of the bridge to reduce the chance that the specimen would slide off its supports during the long duration fatigue test. Thus the unsupported length of bridge #3 was 58 in., compared with 59 in. for the otherwise identical bridge #2.

The fatigue test was similar to a test performed on another fiberglass bridge [9]. The loading was applied under displacement control conditions as a sine wave with a frequency of 5 Hz. The minimum value of the applied displacement was the displacement that corresponded to a preload of 50 lbs. The maximum value of the applied displacement was 0.090 in., which is equal to the maximum allowable displacement of $L/800$ plus 20% (i.e., $1.2 \times L/800 = 1.2 \times 0.075$ in.). This applied load was similar to that used in [9] and is a reasonable simulation of the actual loads that a full-size bridge may experience.

The performance of the bridge under fatigue loading was examined in two ways: by measuring the stiffness of the specimen before, during and after the application of the three million loading cycles; and by measuring the failure load of the bridge after the application of the three million loading cycles. These measurements were obtained in the following manner.

The stiffness of the specimen was measured at the start of the test and after one, two and three million loading cycles in the following way. The load actuator was moved a distance of 0.3 in. after application of the 50 lbs. preload (this corresponded to an applied of load of approximately 1.5 kips). This produced a linear elastic deformation in the specimen, and enabled the stiffness of the bridge to be measured using the various LVDT's employed in the test apparatus. The fatigue test was interrupted every million

cycles and the elastic stiffness measured in this manner. After completion of three million cycles, the bridge stiffness was measured and the specimen loaded to failure.

Figure 7.28 shows bridge #3 during the fatigue test; the displacement of the bridge is clearly visible. No cracking sounds or debonding of the bridge components (see Figure 7.29) were perceived during the application of the cyclic loads and during the various stiffness measurements. After the fatigue test was complete, the bridge was loaded until failure. The failure load of the bridge after the application of three million loading cycles was 7.6 kips. As with bridge #2, the collapse of the specimen was initiated by the development of cracks in the compression side of the outer shell near the load application regions as shown in Figure 7.30.

Figure 7.31 shows the measured deflections of bridge #3 after the application of three million loading cycles. Figure 7.32 shows a comparison between the measured stiffnesses of the bridge before, during and after the fatigue loading. These data are discussed further in Chapter 9.

7.2.6 Summary of the Experimental Results

Tables 7.4 and 7.5 summarize the measured stiffness and failure loads of the six cell bridges. The stiffnesses were calculated by measuring the initially constant slopes of the load-deflection plots obtained during the final loading of the specimens (i.e., the loading that caused the specimen to fail). These values are expected to produce a reasonable approximation to the linear stiffness of the bridge specimens. The failure loads correspond to the observed load carrying capacities of the various bridges, and are expected to be significantly higher than the first ply failure loads.

In Chapter 9, the data presented in Tables 7.4 ad 7.5 are discussed and compared with the predicted specimen stiffnesses and strengths computed using the finite element models described in Chapter 8.

Name	Inner Cell Gap	Inner Cell Material	Outer Shell Material
Bridge A	0 in.	glass	glass
Bridge B	3/16 in.	glass	glass
Bridge C	1/16 in.	glass	glass
Bridge D	0 in.	glass	glass
Bridge E	0 in.	carbon	glass

Table 7.1: Summary of the two cell bridge specimens.

Name	Stiffness	First Ply Failure
Bridge A	3,610 lb/in	
Bridge B	3,080 lb/in	
Bridge C	3,260 lb/in	
Bridge D	3,430 lb/in	2,400 lbs
Bridge E	3,990 lb/in	1,100 lbs

Table 7.2: Measured stiffnesses and failure loads for the two cell bridges.

Name	Length	Inner Cell		Outer Shell	
		Material	Angle	Material	Angle
Bridge #1	41 in.	glass	±45°	glass	±30°
Bridge #2	60 in.	glass	±45°	glass	±45°
Bridge #3	60 in.	glass	±45°	glass	±45°
Bridge #4	60 in.	glass	±45°	carbon/glass	±45°
Bridge #5	60 in.	carbon	±45°	glass	±50°

Table 7.3: Summary of the six cell bridge specimens.

	Bridge #1	Bridge #2	Bridge #3	Bridge #4	Bridge #5
Actuator	5,823 lb/in	4,335 lb/in	4,792 lb/in	2,601 lb/in	4,740 lb/in
LVDT 1	8,805 lb/in	7,242 lb/in	8,550 lb/in	5,334 lb/in	7,535 lb/in
LVDT 2	8,533 lb/in	7,283 lb/in	8,163 lb/in	5,846 lb/in	7,047 lb/in
LVDT 3	15,728 lb/in	5,813 lb/in	7,266 lb/in	4,768 lb/in	6,445 lb/in
LVDT 4	17,604 lb/in	6,052 lb/in	6,854 lb/in		6,407 lb/in

Table 7.4: Measured stiffnesses for the six cell bridges.

Name	First Ply Failure
Bridge #1	2,000 lbs
Bridge #2	2,600 lbs
Bridge #4	3,000 lbs
Bridge #5	2,200 lbs

Table 7.5: Measured failure loads for the six cell bridges.

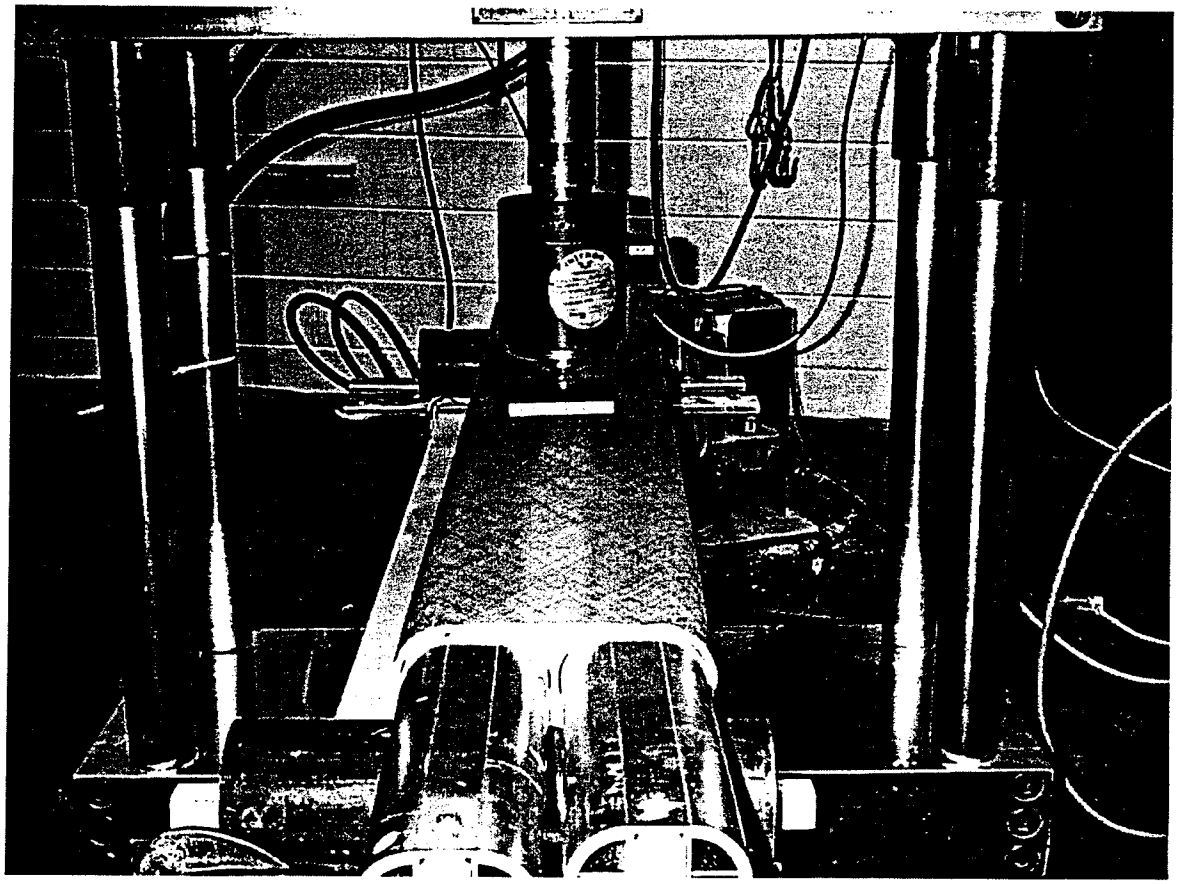

Figure 7.1: Testing configuration for bridge A.

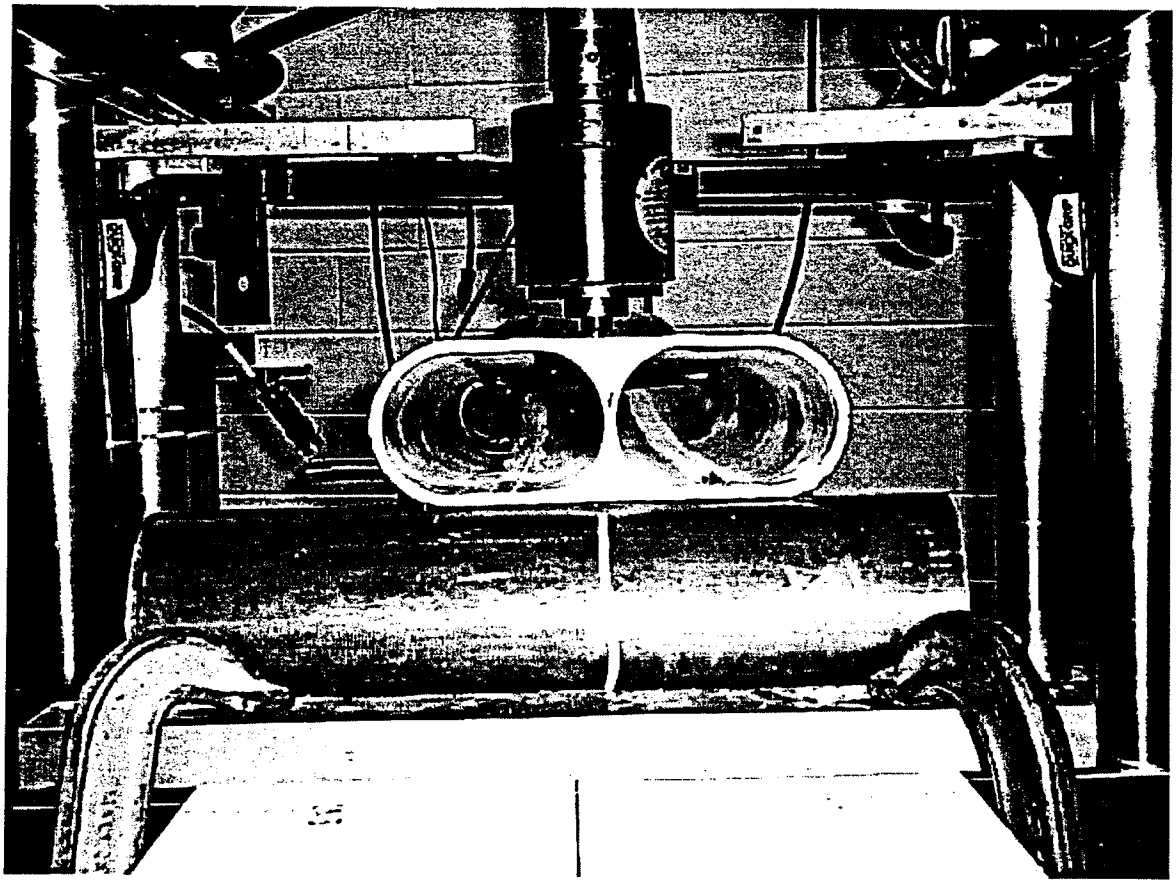

Figure 7.2: Testing configuration for bridge D.

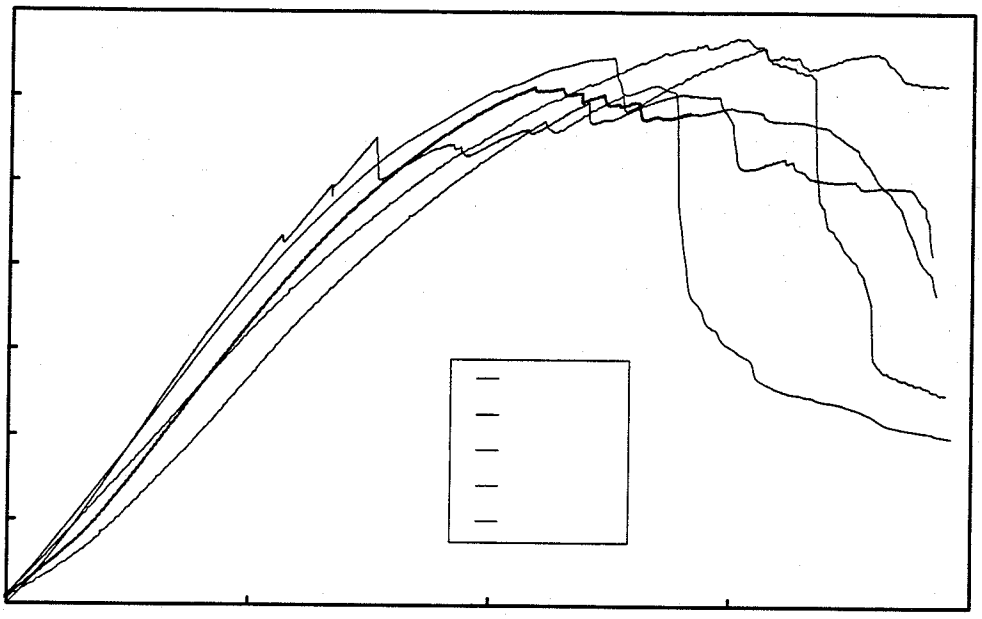

Figure 7.3: Measured actuator load-deflection data for the two cell bridges.

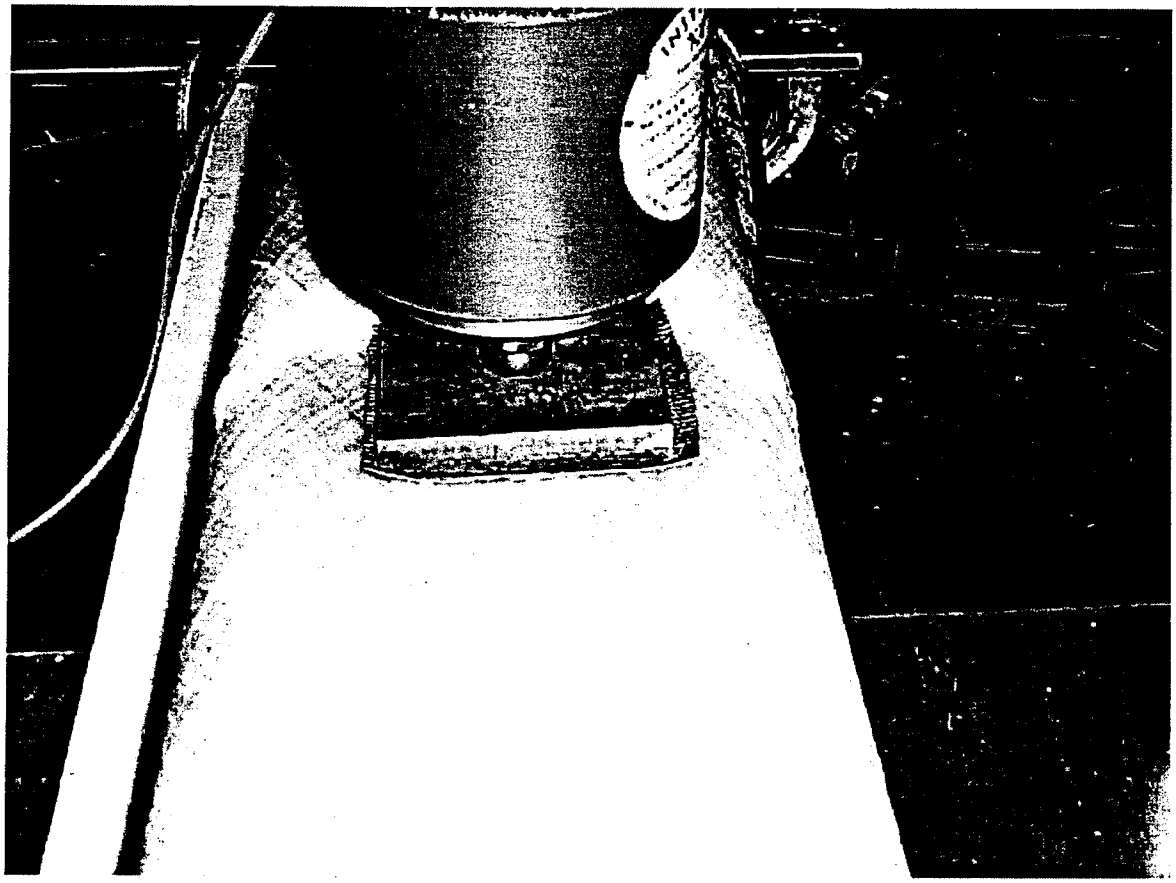

Figure 7.4: Failure of bridge D.

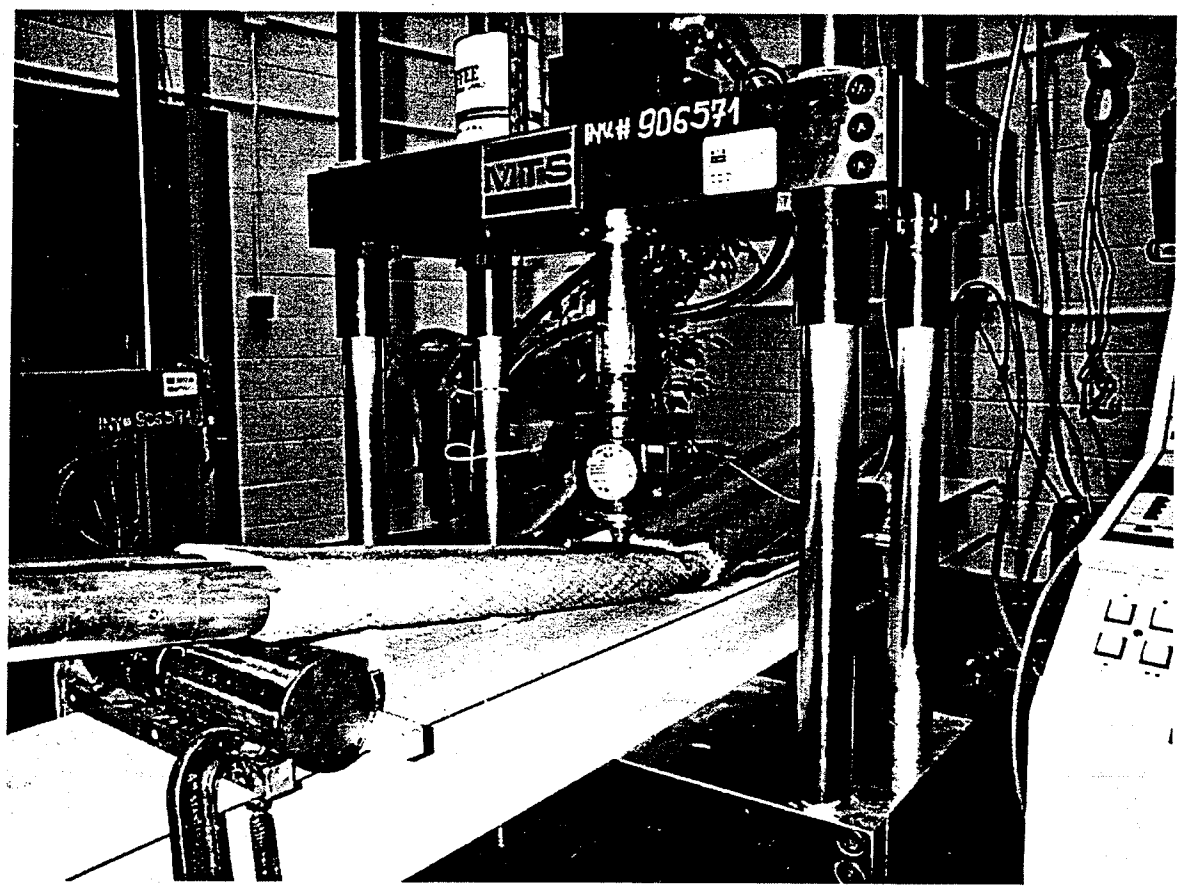

Figure 7.5: Ultimate collapse of bridge A.

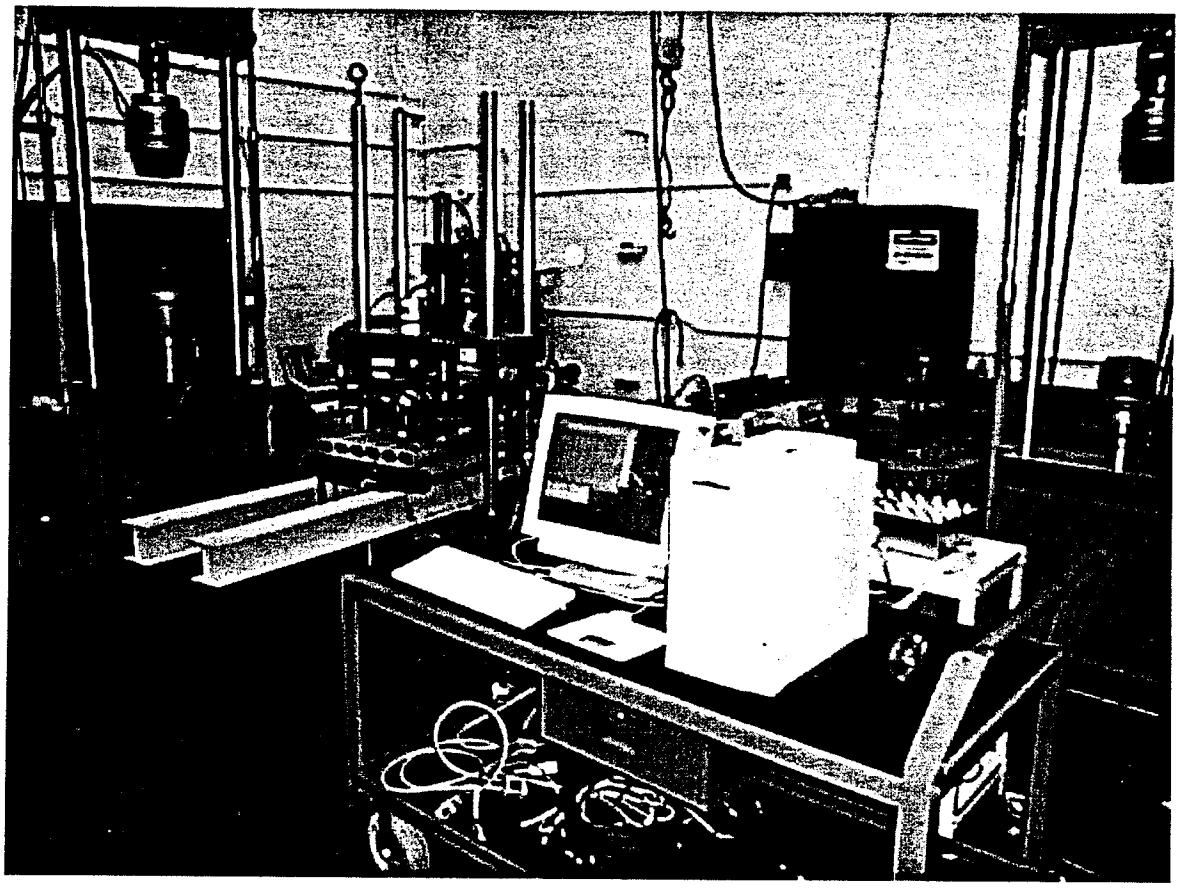

Figure 7.6: Experimental apparatus used of the six cell bridges (bridge #1 shown).

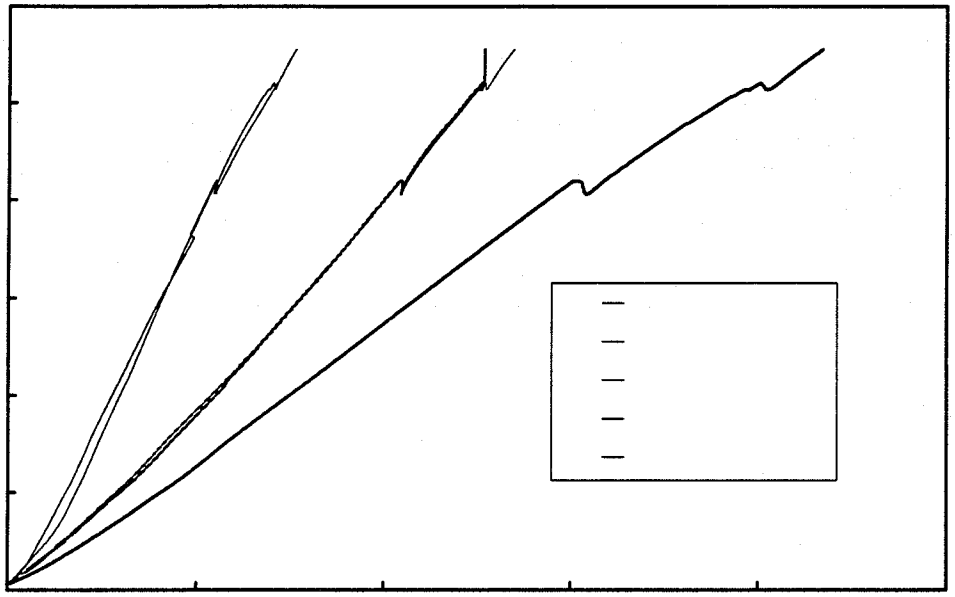

Figure 7.7: Measured load-deflection data for bridge #1.

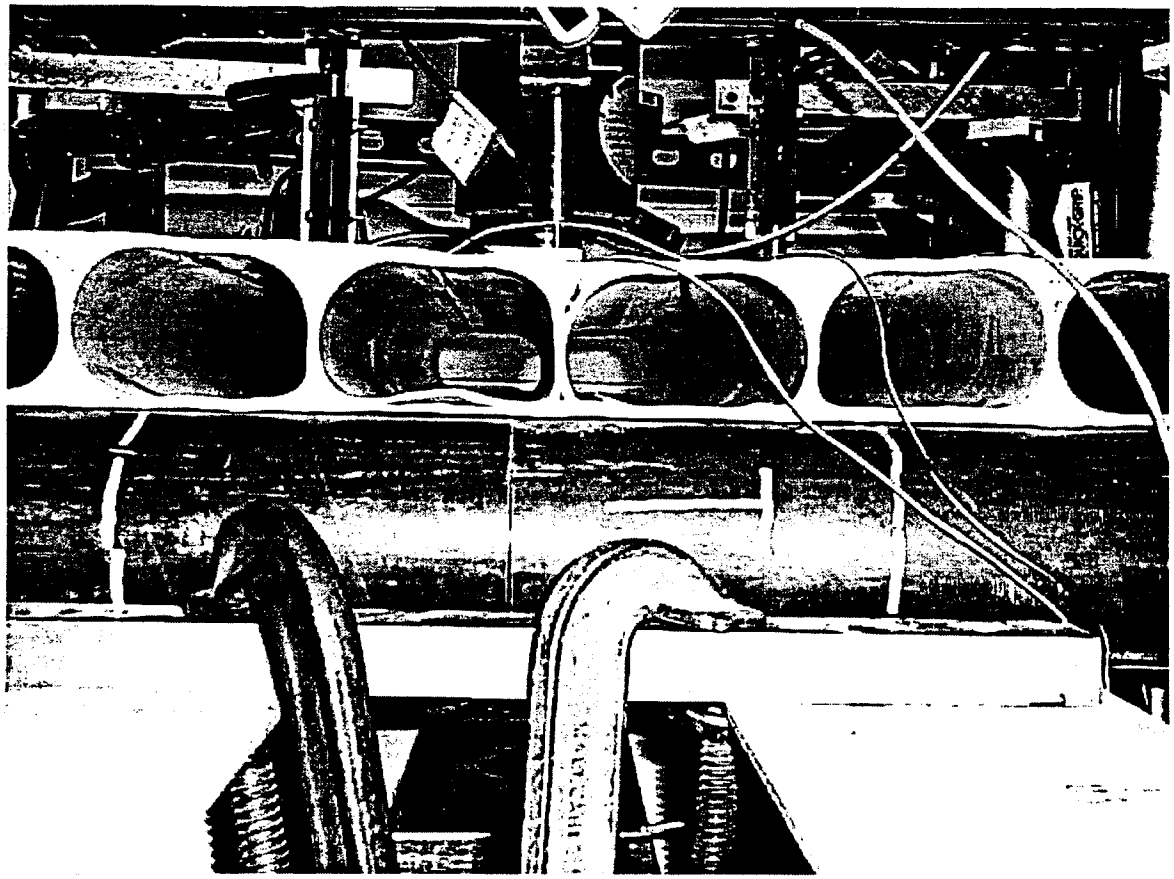

Figure 7.8: Debonding between the inner cells and the outer shell of bridge #1.

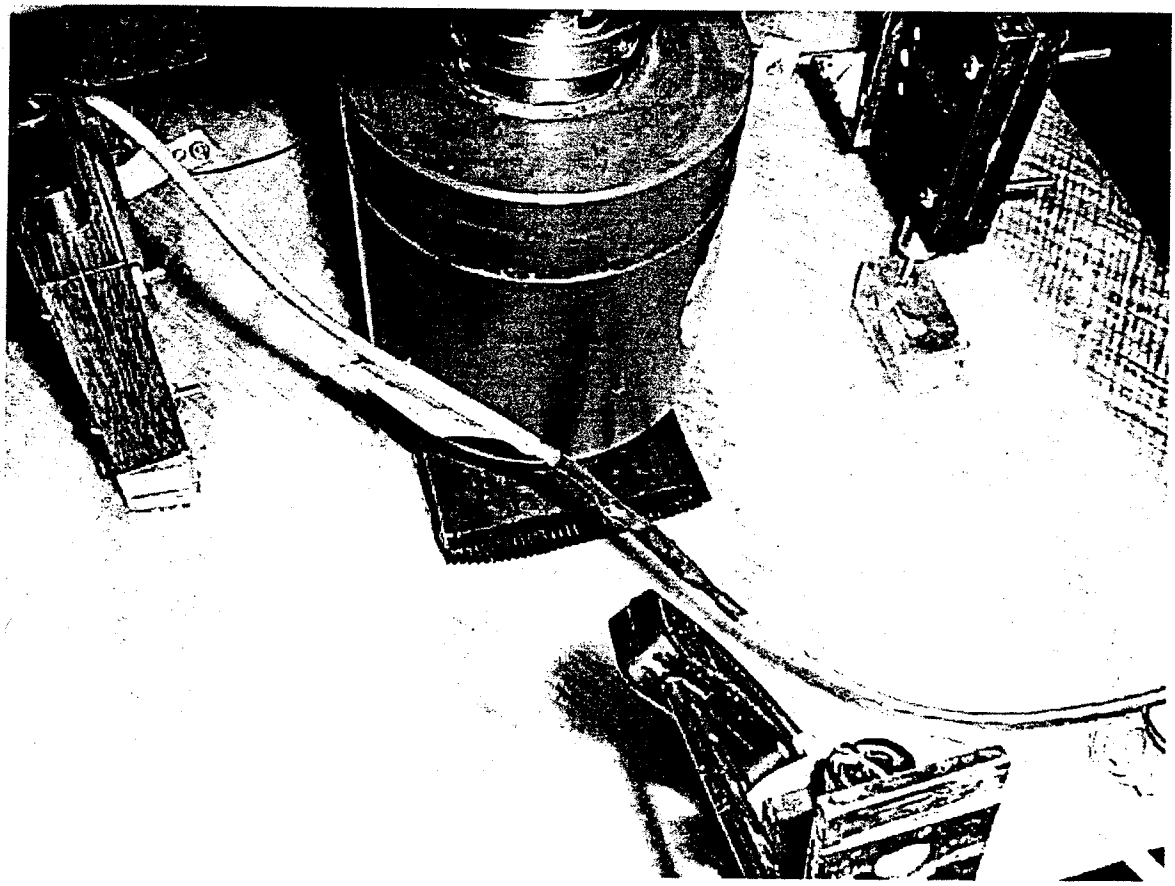

Figure 7.9: Initial cracking of the outer shell of bridge #1.

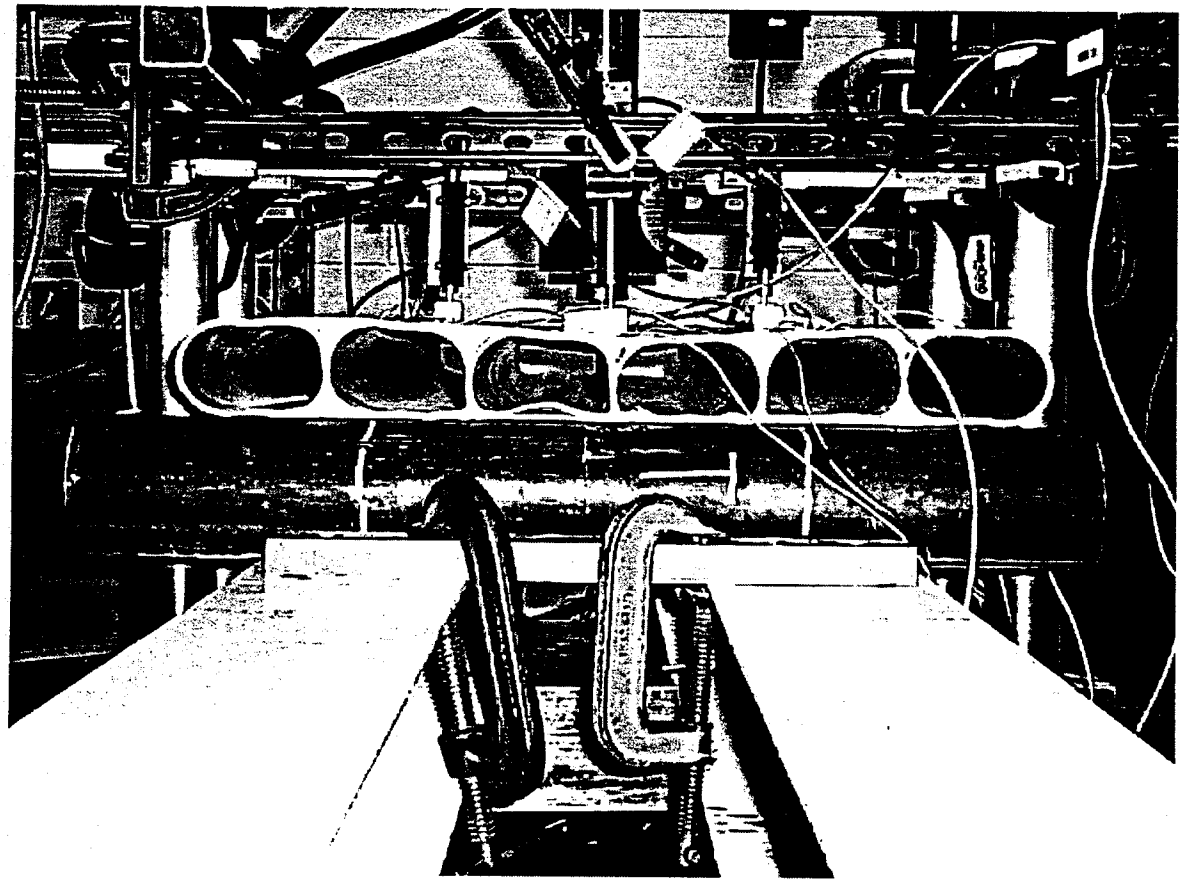

Figure 7.10: Debonding at inner cell-outer shell interface of bridge #1.

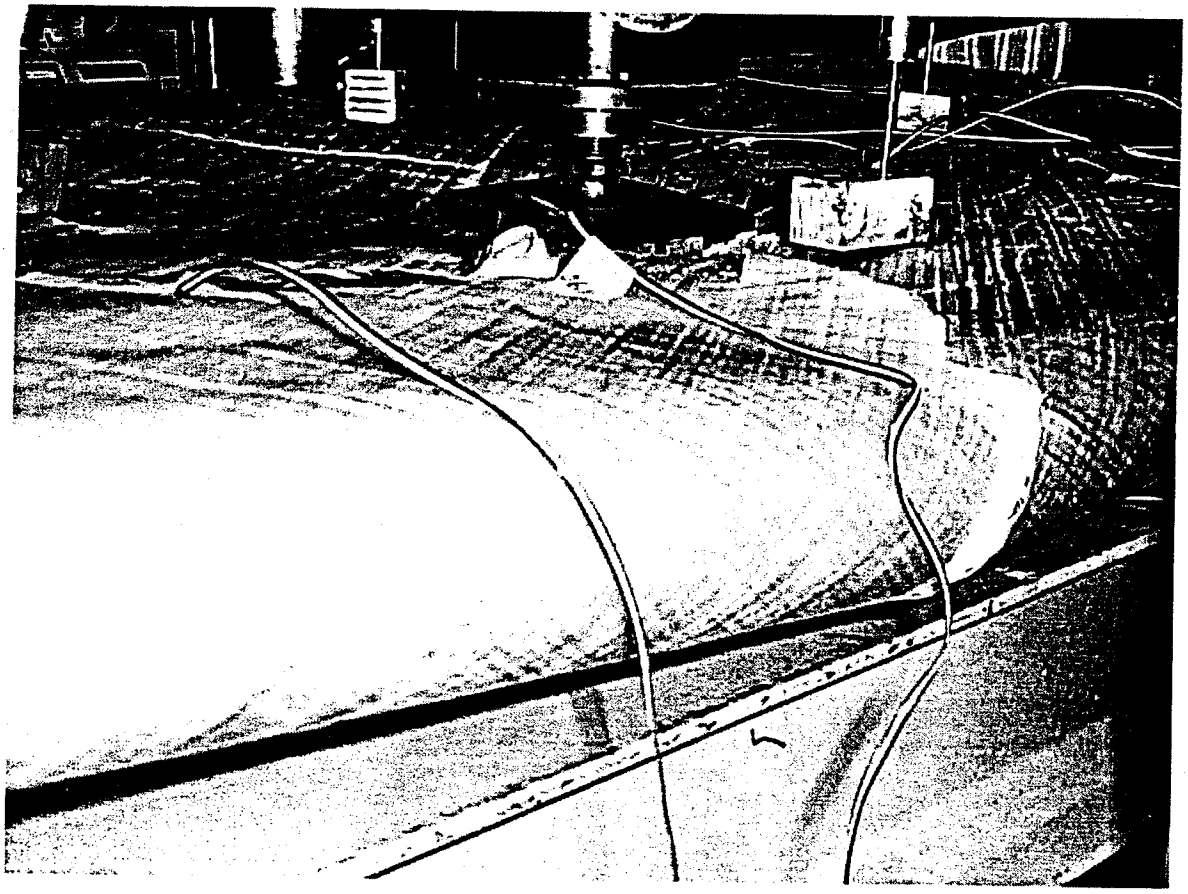

Figure 7.11: Final failure of bridge #1.

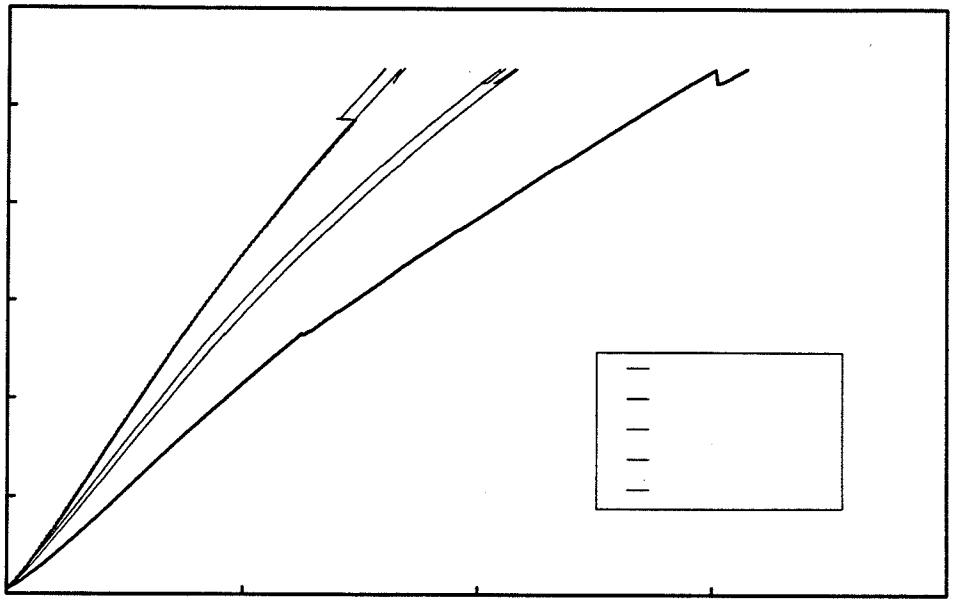

Figure 7.12: Measured load-deflection data for bridge #2.

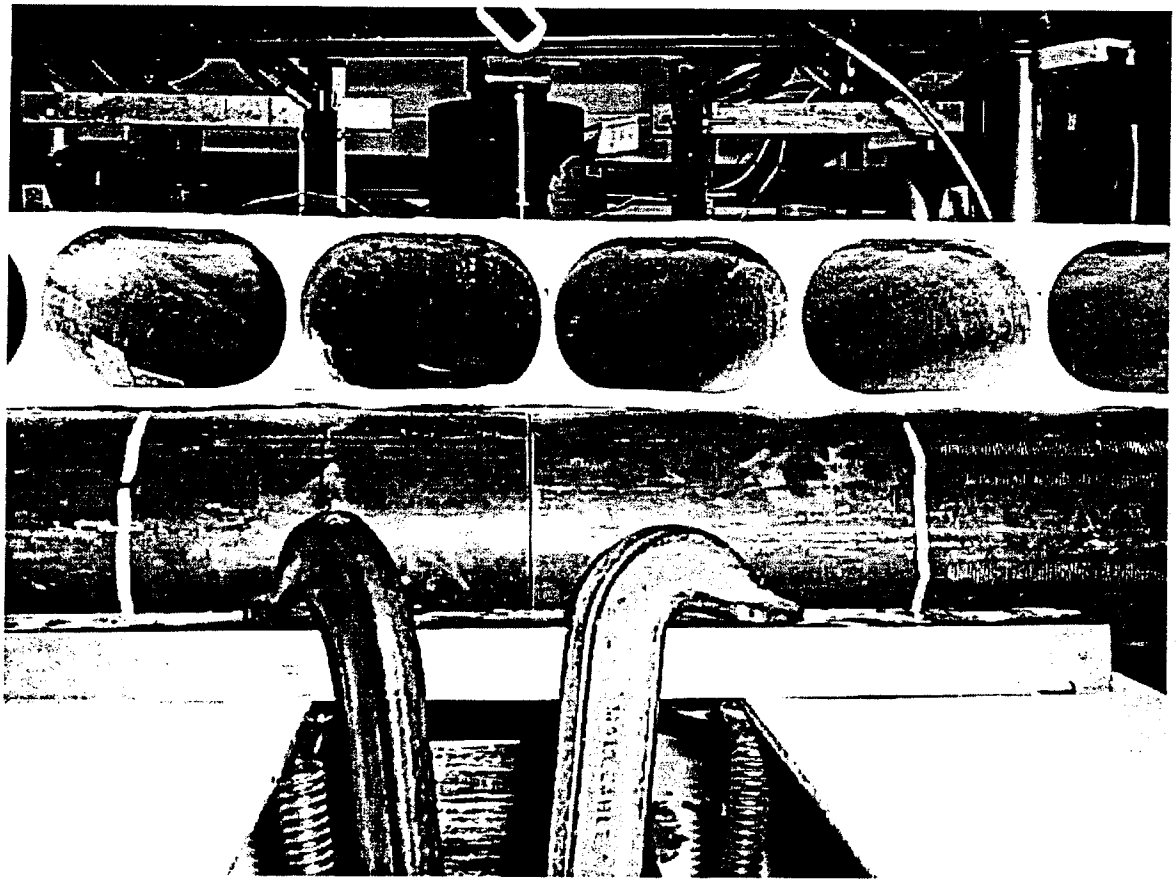

Figure 7.13: Maintenance of the bond between the inner cell and outer shell of bridge #2.

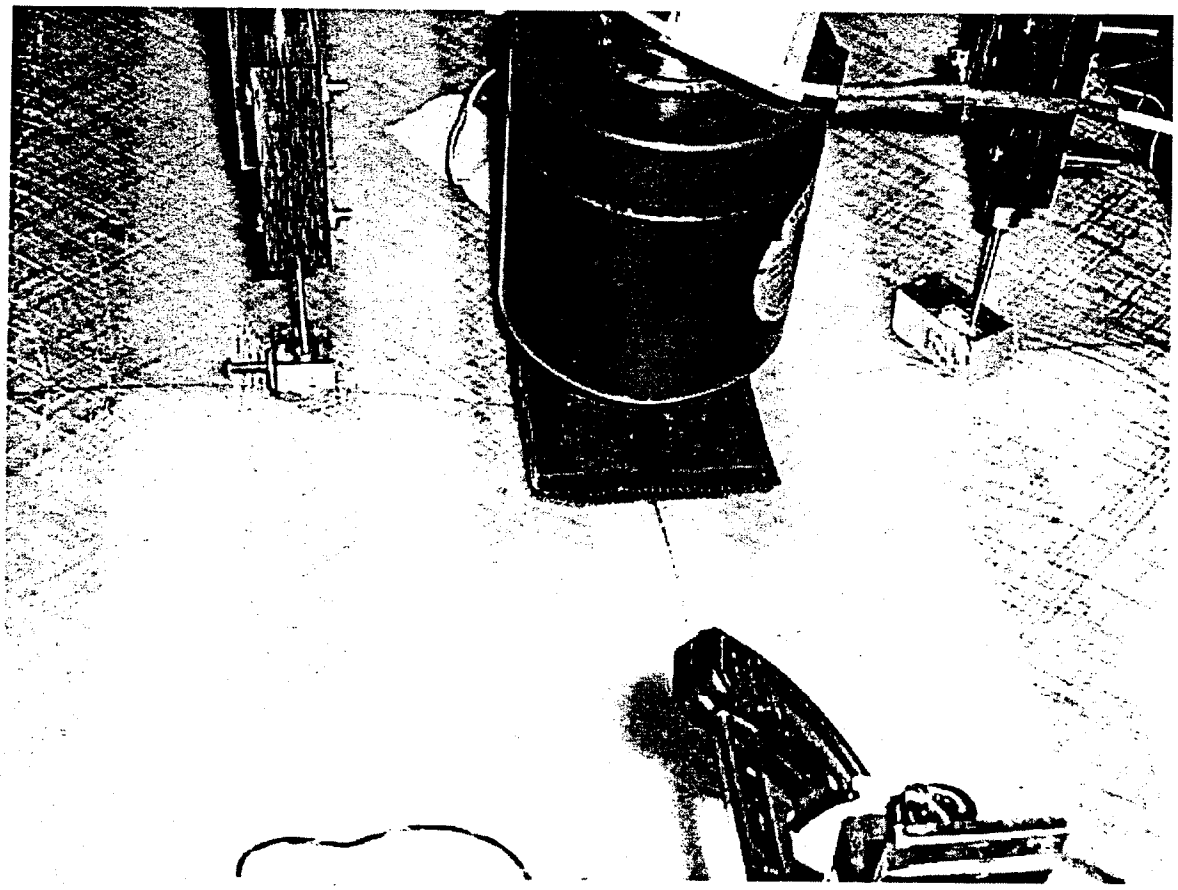

Figure 7.14: Initiation of cracks in the outer shell of bridge #2.

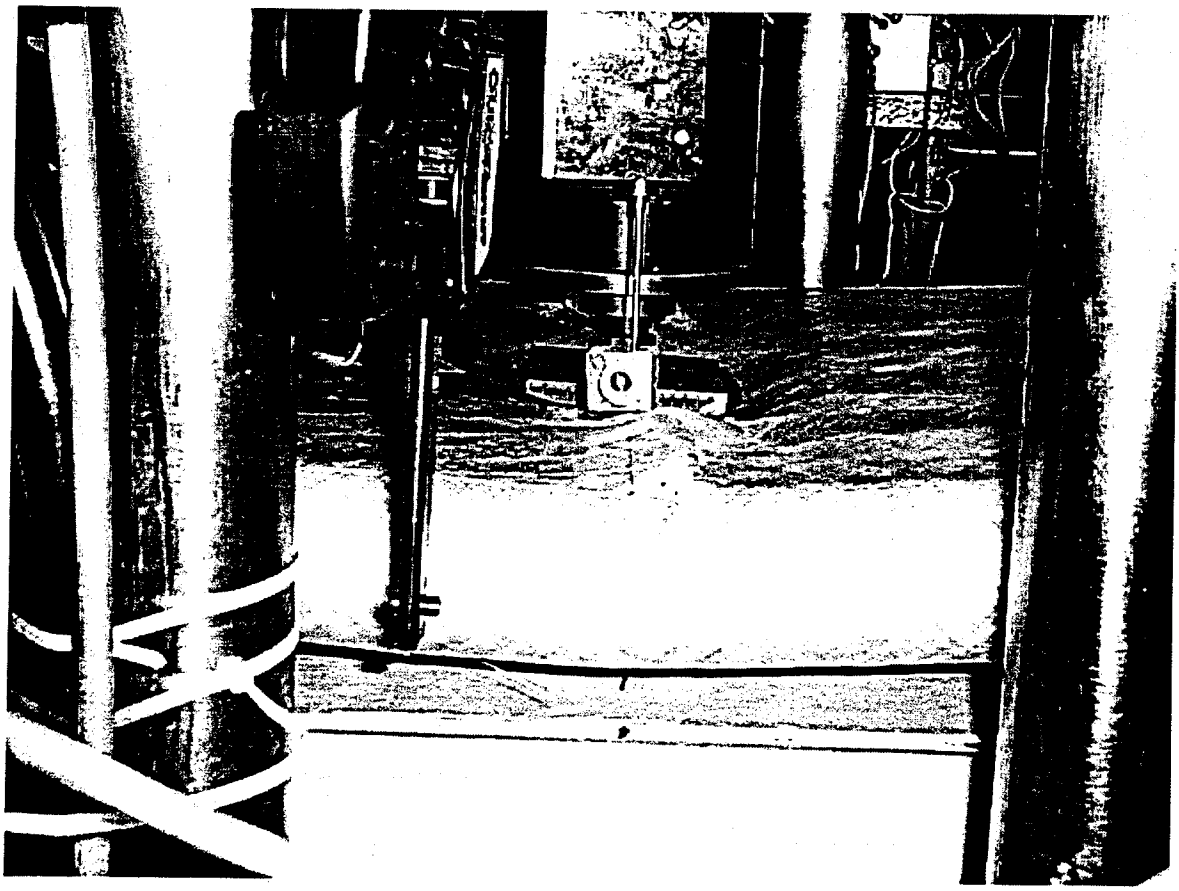

Figure 7.15: Final failure of bridge #2.

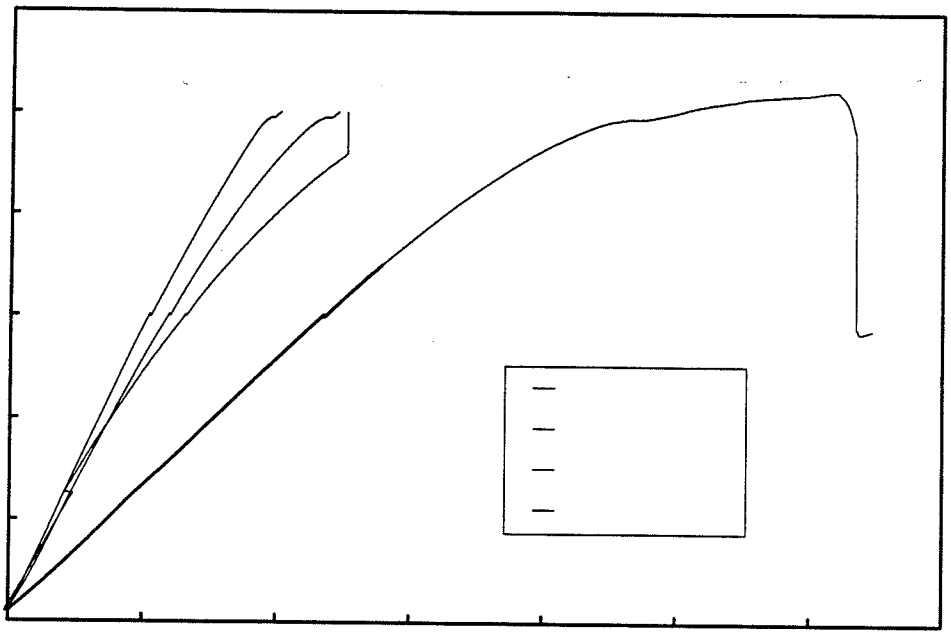

Figure 7.16: Measured load-deflection data for bridge #4.

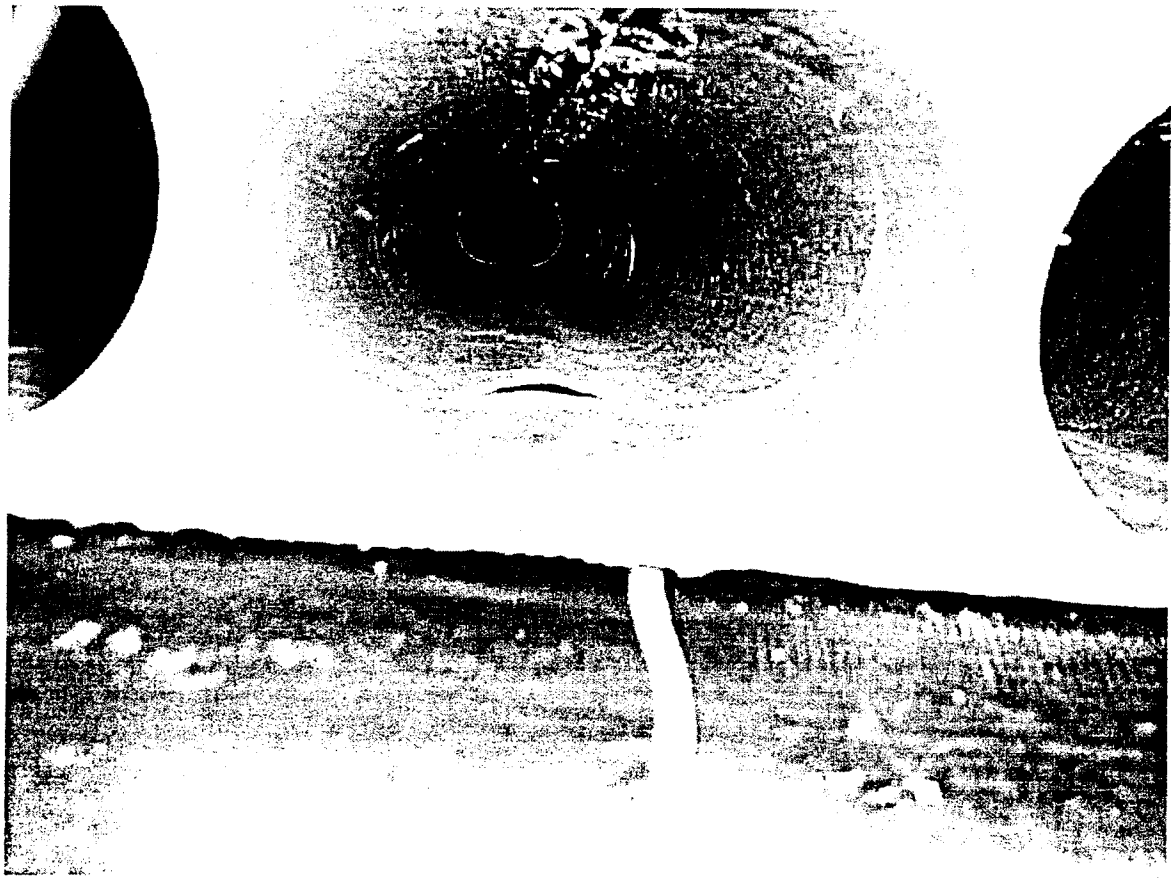

Figure 7.17: Manufacturing defect in the inner cell of bridge #4.

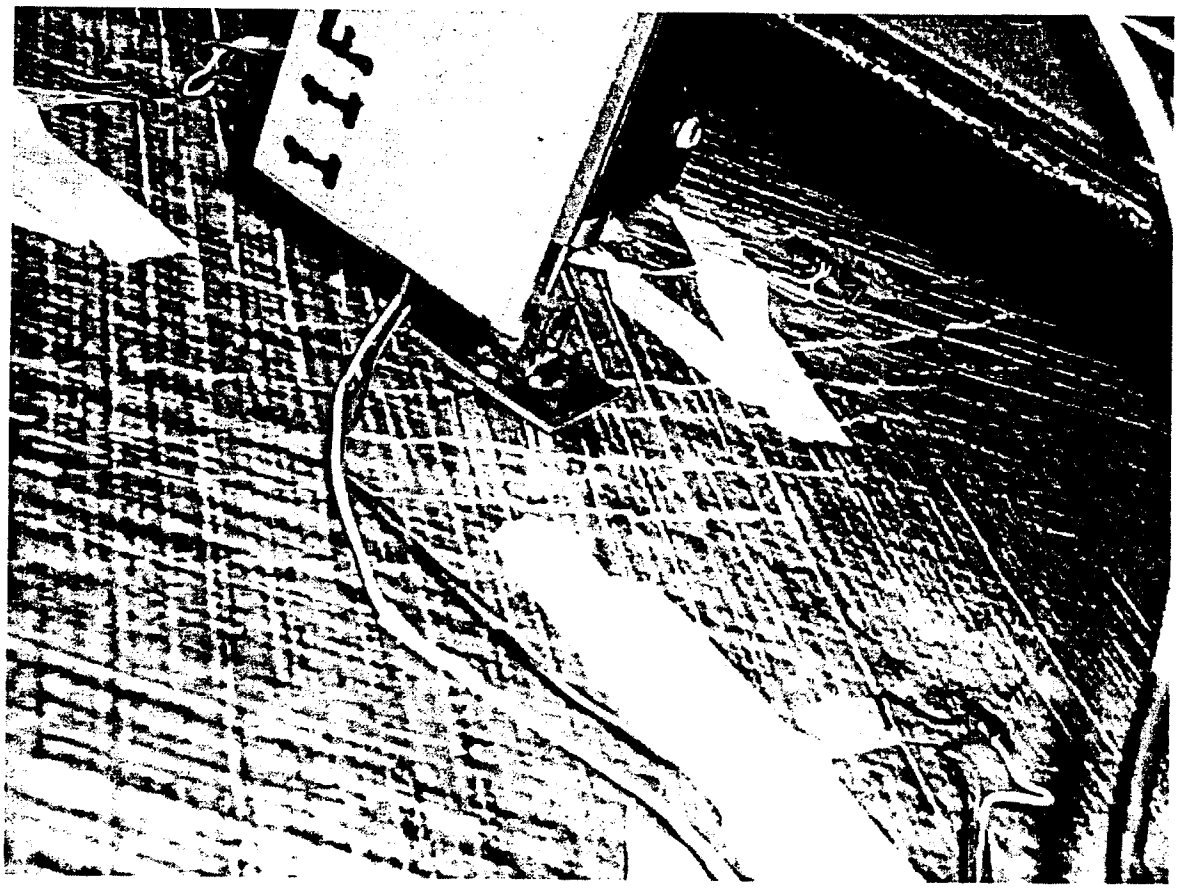

Figure 7.18: Initial cracking in the outer shell of bridge #4.

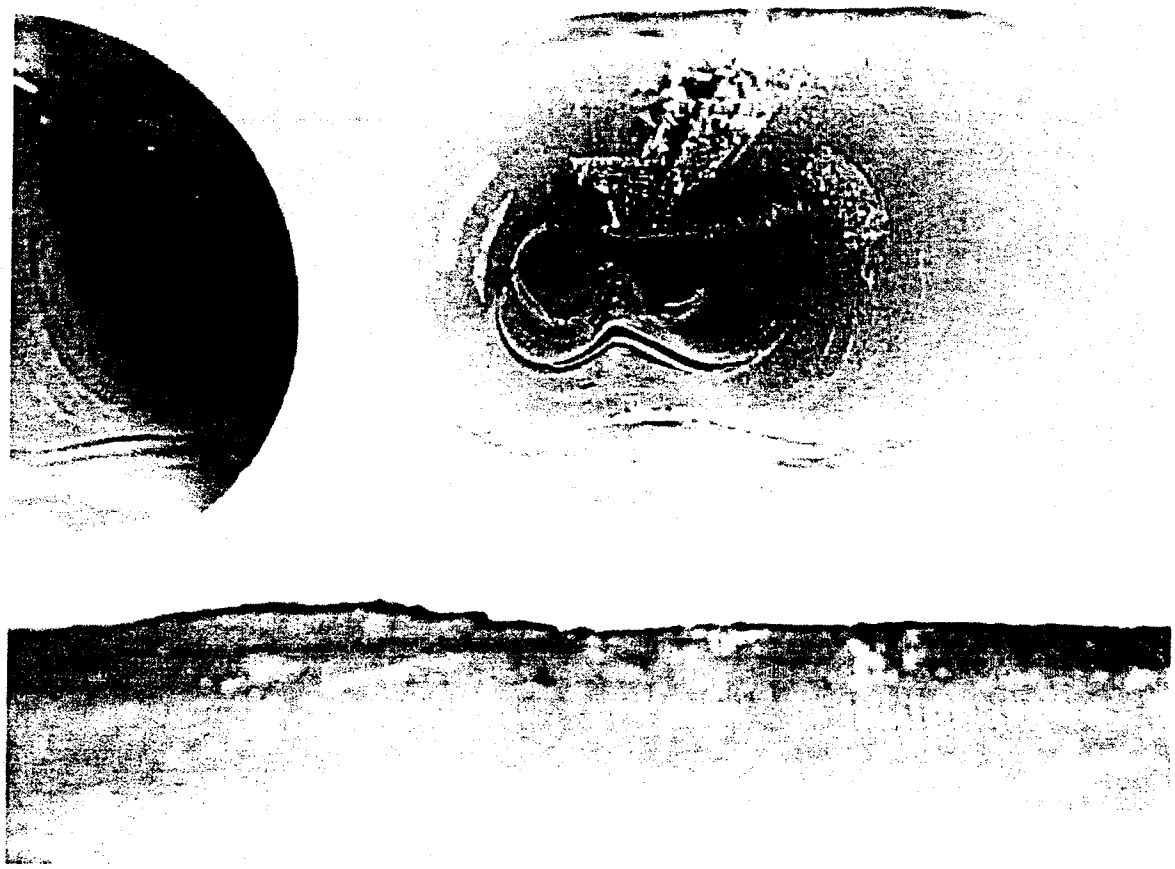

Figure 7.19: Inner cell buckling and cracking in bridge #4.

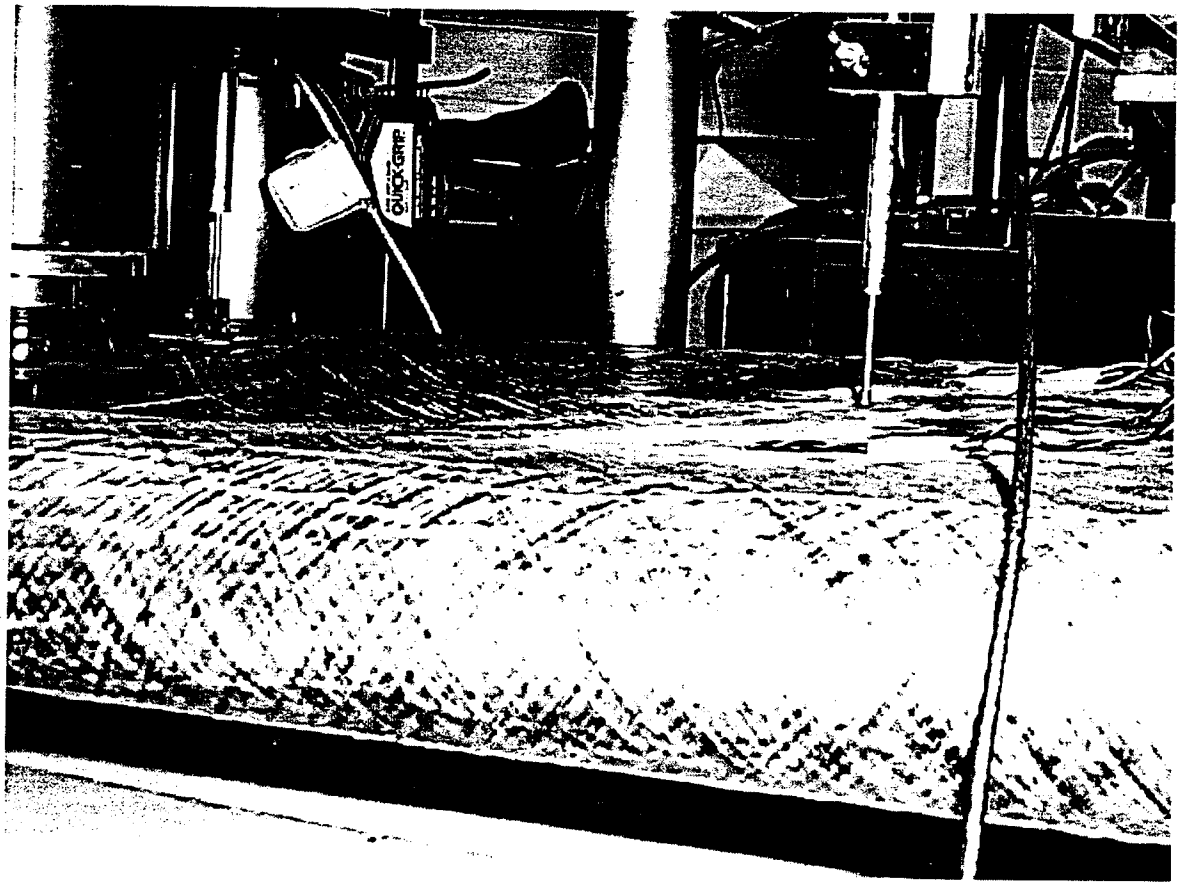

Figure 7.20: Deformation of the top surface of bridge #4.

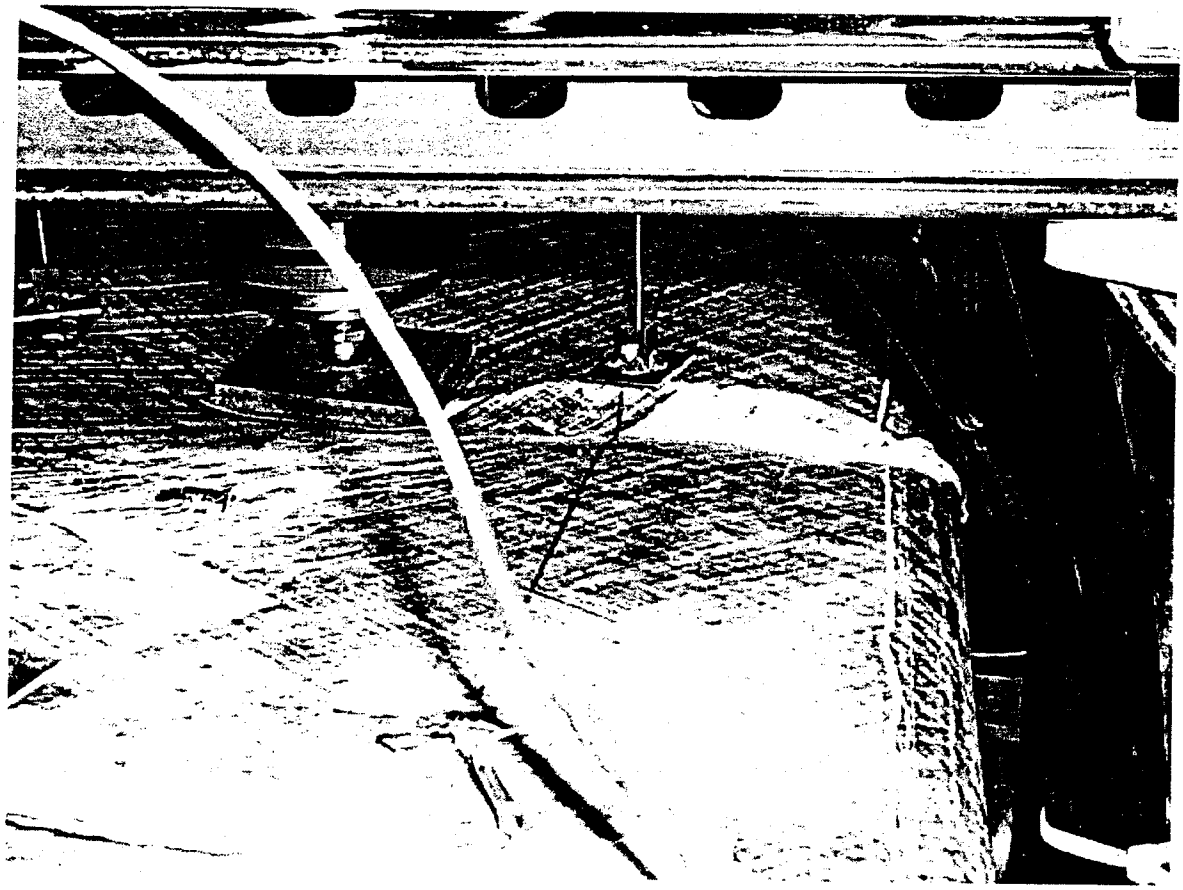

Figure 7.21: Final failure of bridge #4.

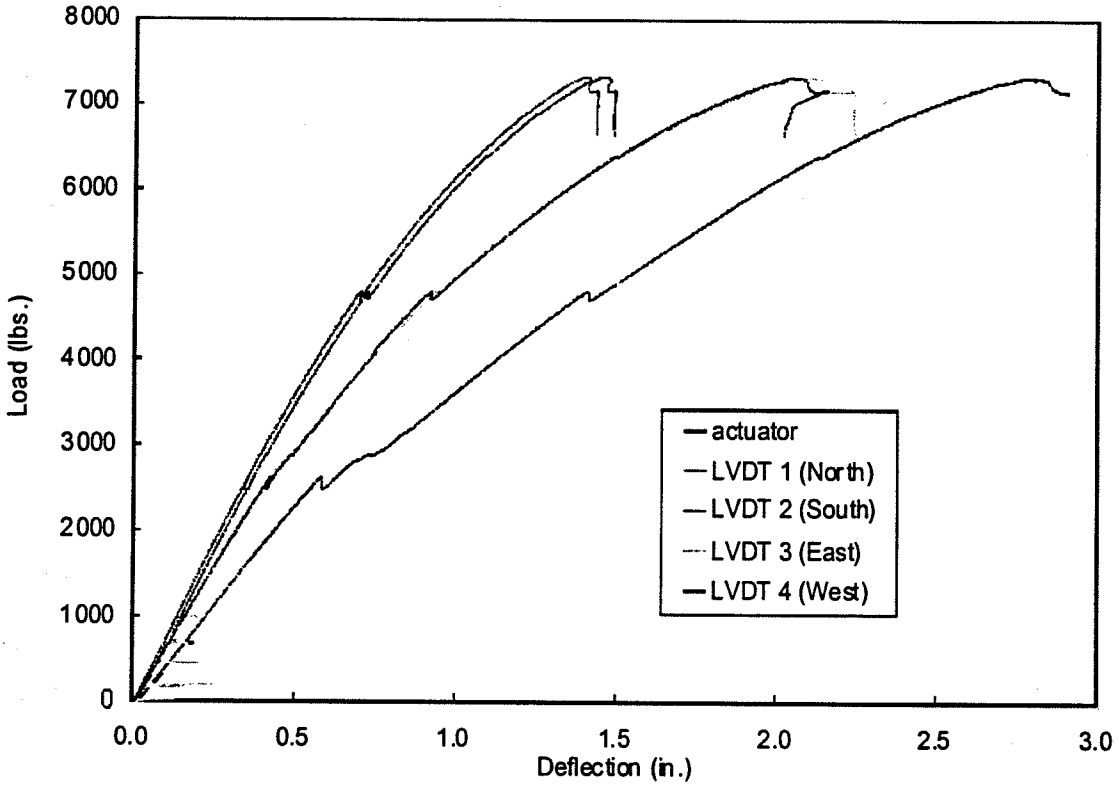

Figure 7.22: Measured load-deflection data for bridge #5.

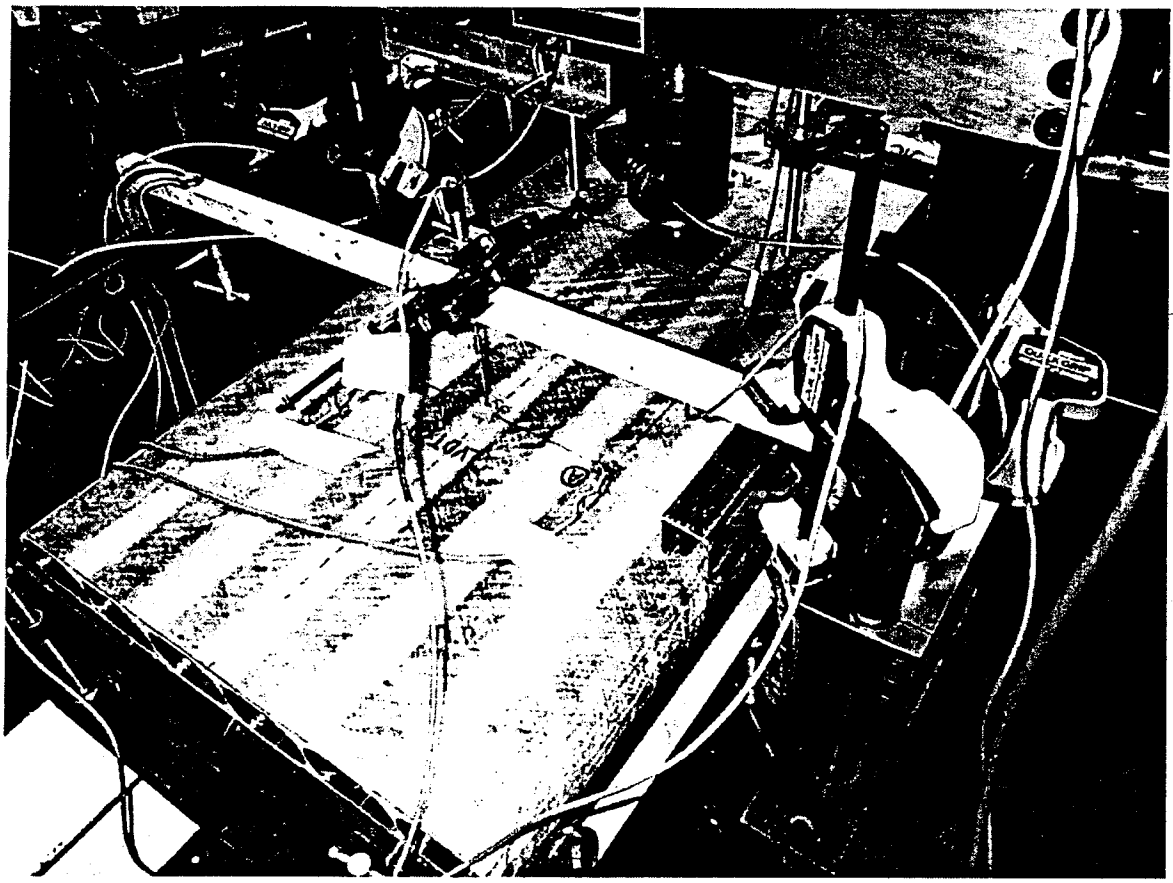

Figure 7.23: Testing configuration for bridge #5.

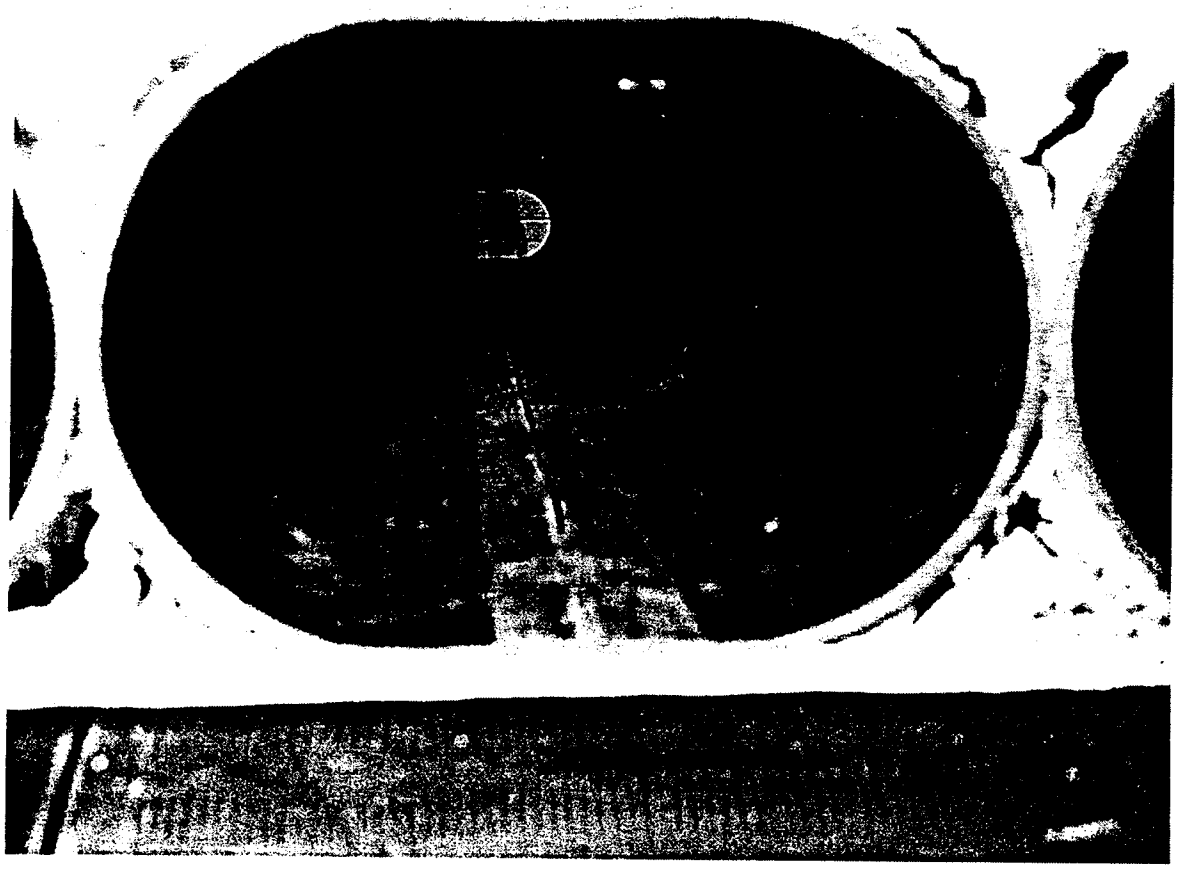

Figure 7.24: Initial longitudinal cracks in inner cells of bridge #5.

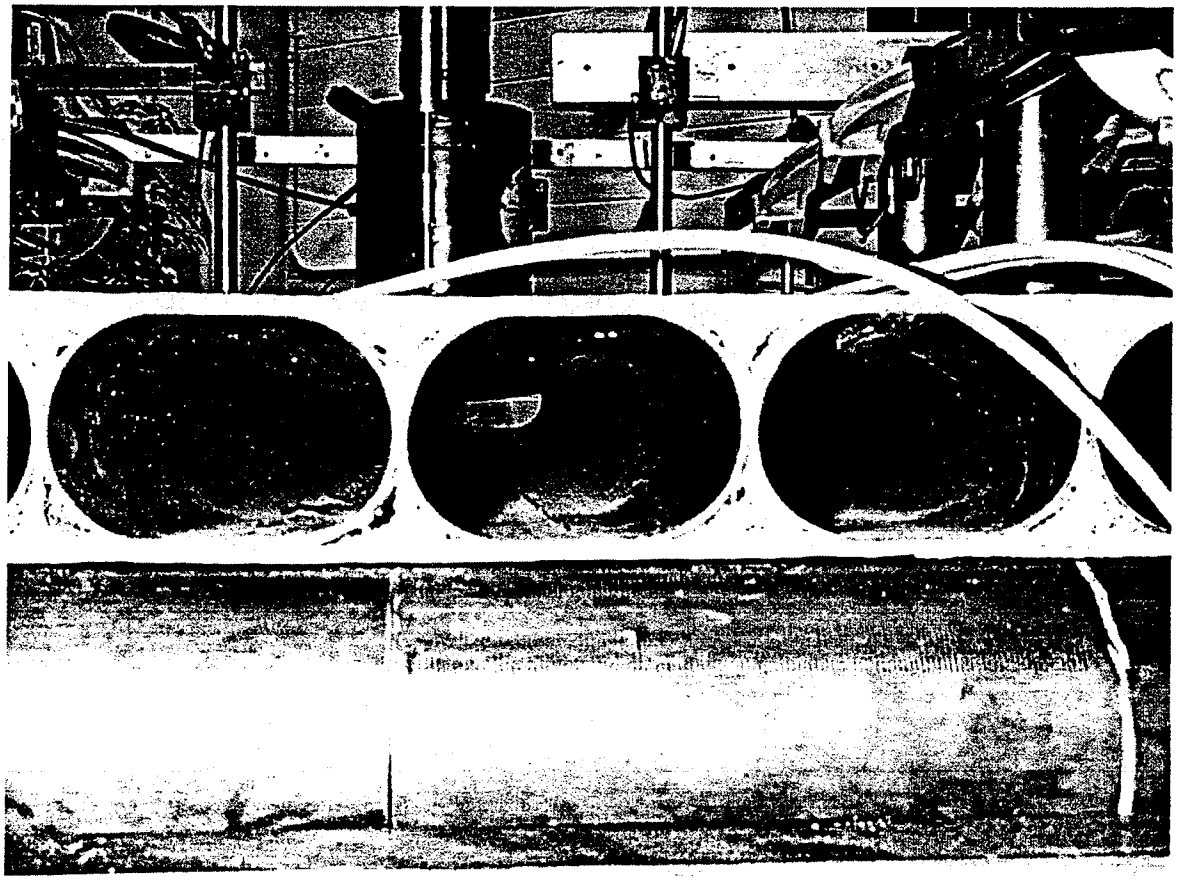

Figure 7.25: Localized deformation of bridge #5.

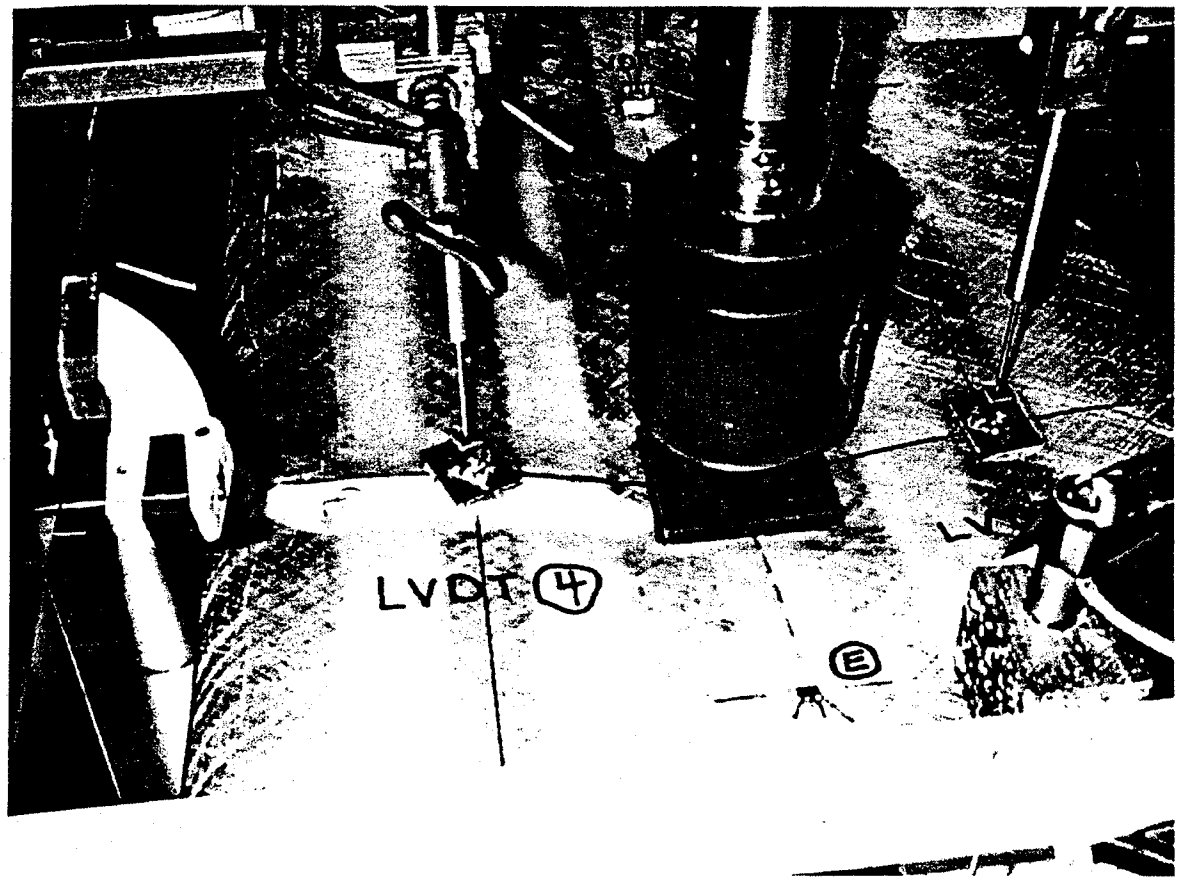

Figure 7.26: Outer shell cracks in bridge #5.

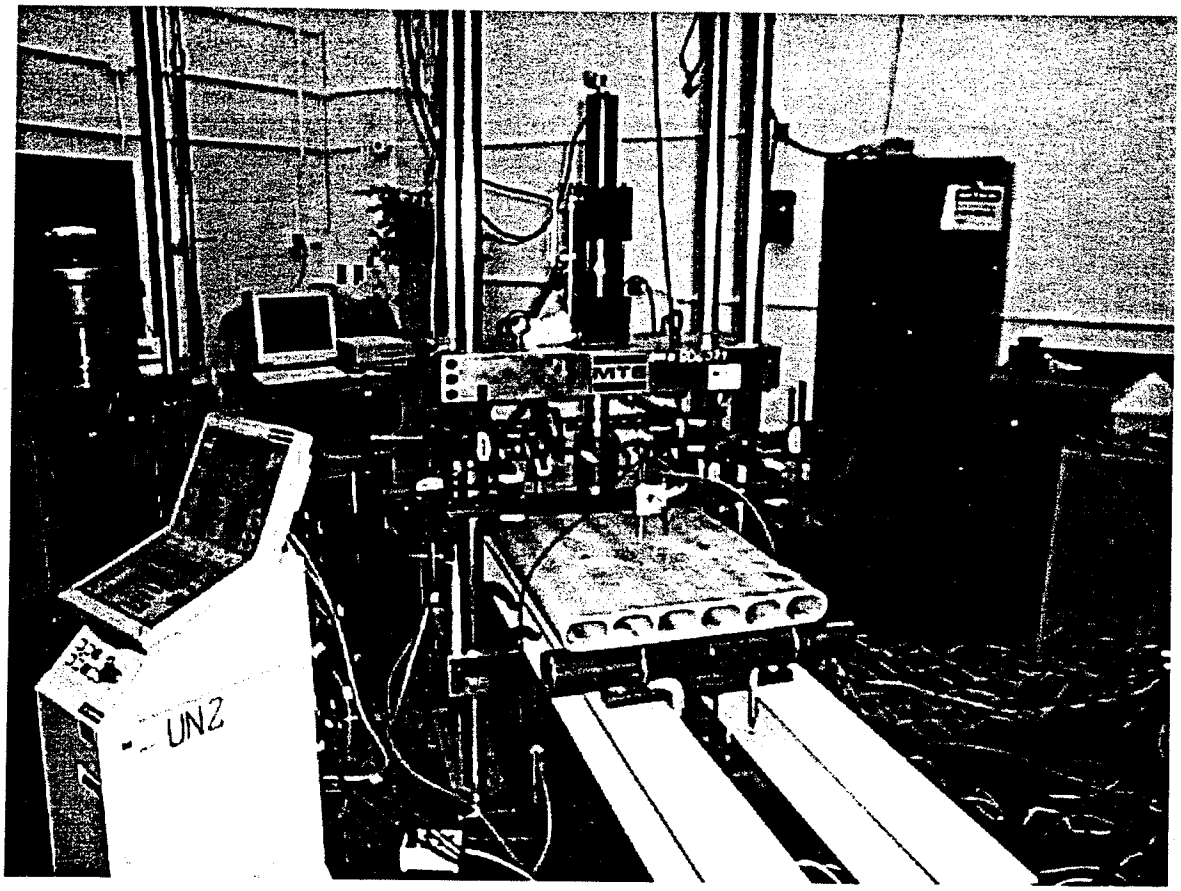

Figure 7.27: Experimental apparatus employed for the fatigue test of bridge #3.

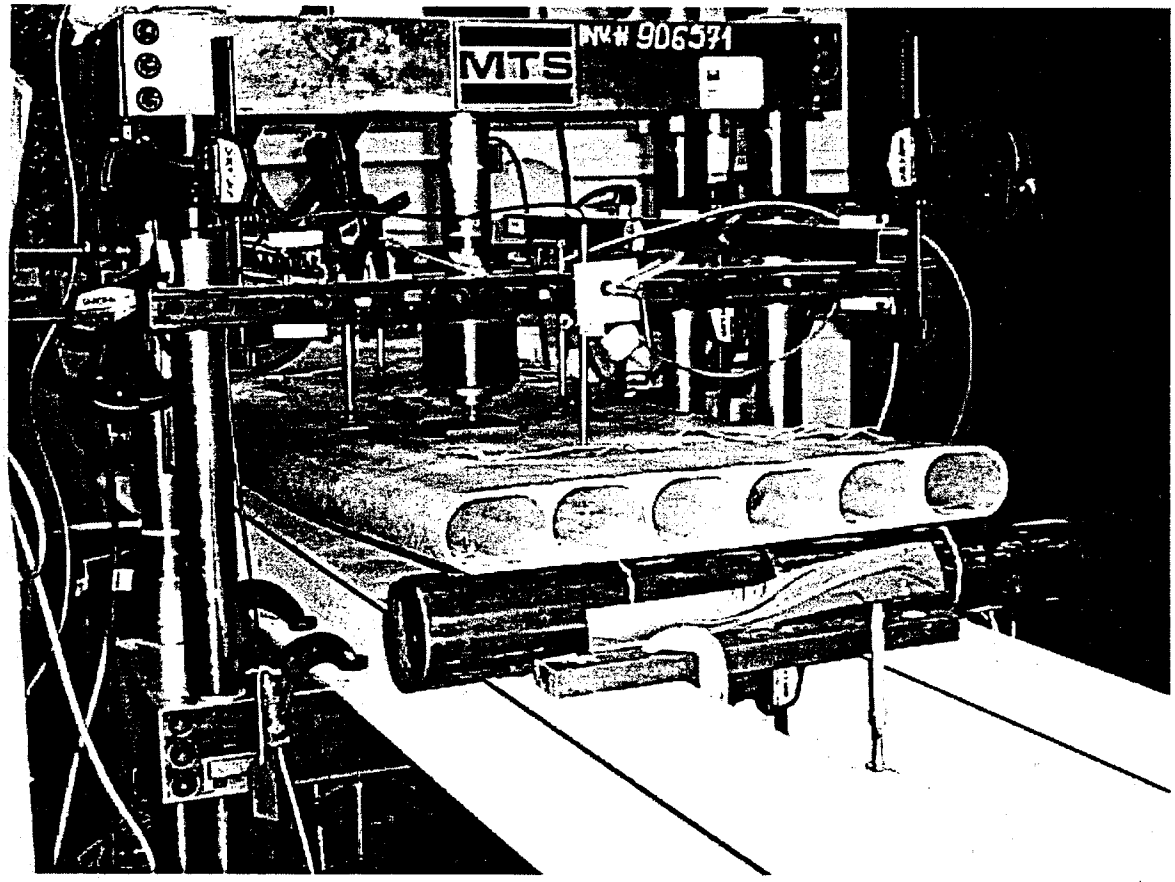

Figure 7.28: Bridge #3 during the fatigue test.

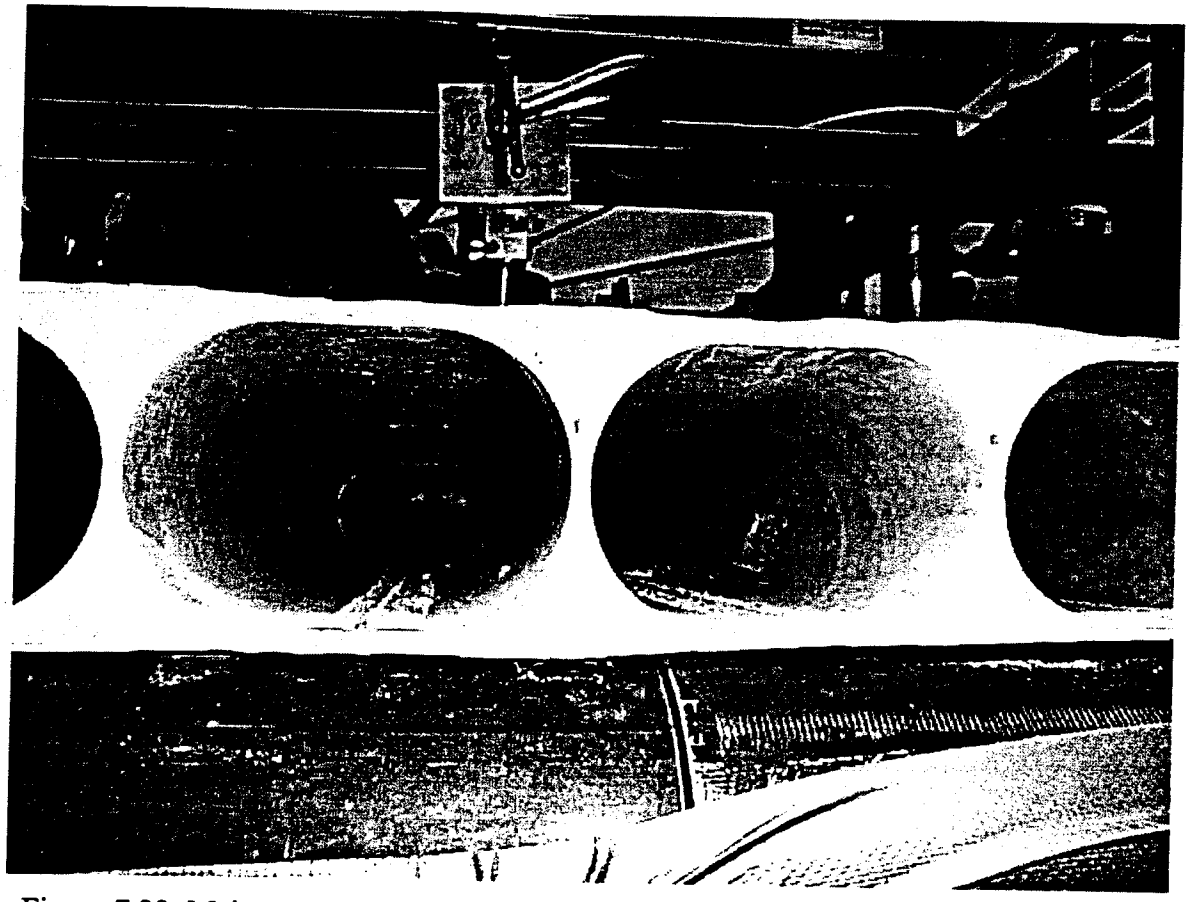

Figure 7.29: Maintenance of the bond between the inner cells and the outer shell during the fatigue test of bridge #3.

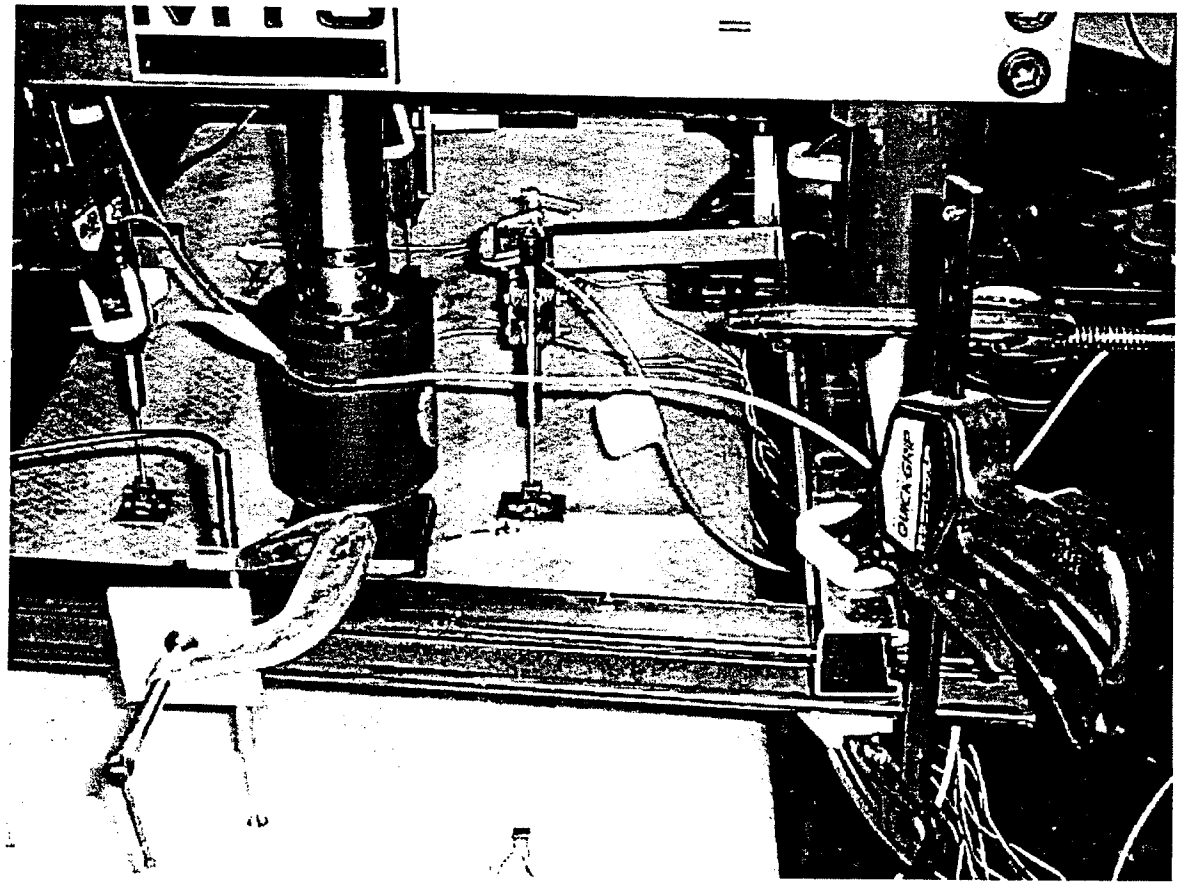

Figure 7.30: Final failure of bridge #3.

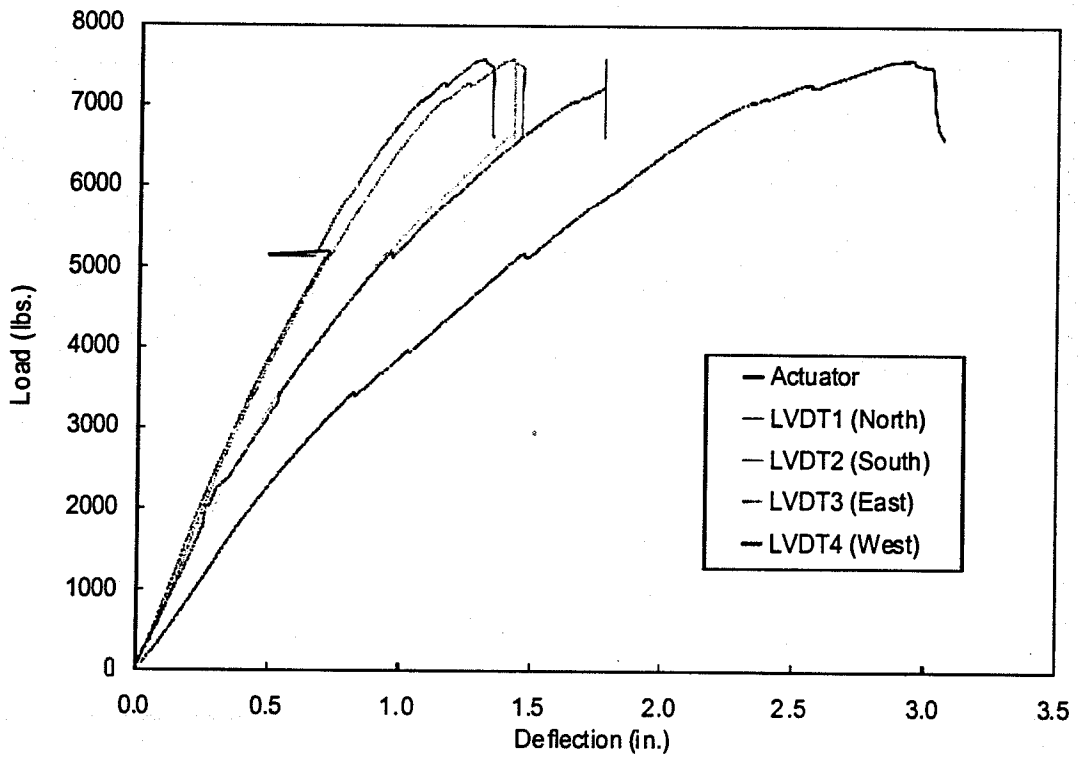

Figure 7.31: Measured load-deflection data for bridge #3 after three million loading cycles.

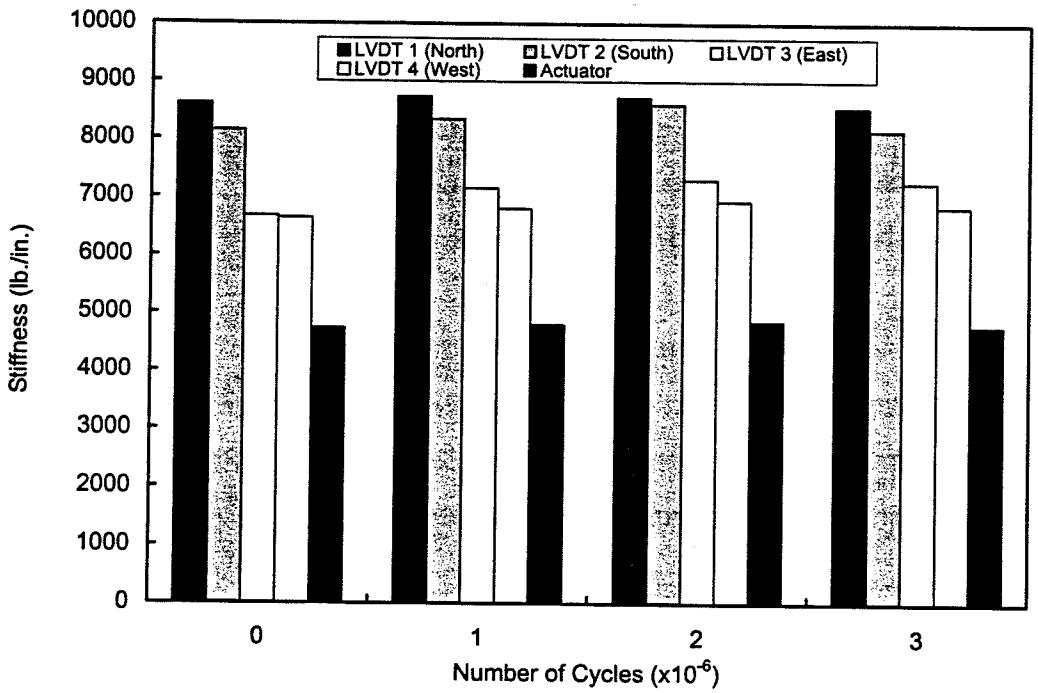

Figure 7.32: Measured stiffnesses of bridge #3 before, during and after the fatigue test.

8. Finite Element Analysis of the Prototype Bridges

This chapter presents the methodology and the results of a series of finite element analyses that were conducted in an attempt to predict the experimentally observed specimen stiffnesses and strengths documented in Chapter 7. In all cases, the commercially available analysis code Abaqus version 5.7 was used.

8.1 Two Cell Bridges

Finite element models were constructed of bridges D and E. These were the only two cell bridges modeled since their construction were closest to those of the six cell bridges (i.e., a REPEAT parameter equal to one and no gap between the inner cells).

Figure 8.1 shows the finite element mesh that was constructed to model bridges D and E. It consisted of 6,283 nodes and 6,528 S4R5 four-node shell elements. Note that nodes were placed at the locations of the four LVDT's employed during the specimen tests. Also, the mesh was designed so that a contiguous patch of elements was placed over the load application region. The glass and carbon fiber were assigned the linear elastic material properties listed in Tables 8.1; these data were assembled form information provided by the manufacturer and by independent tests. Table 8.2 lists the lamina thicknesses and winding angles that were used in the inner cells and the outer shells. The total thickness of each component was measured at several locations using a caliper. The average values were then used I n the finite element model. The winding angles were also measured directly form the manufactured specimens. The models of the bridges are simply supported at the lower edge of each end, consistent with the roller supports used in the tests. A uniform pressure is applied over a square surface located at the center of the bridge and having the same dimensions as the square plate used to load the specimens. The pressure was chosen to produce a total load of 1 lb. Note that this is not an exact representation of the manner in which the loads were applied during the tests. In the tests, the actuator was subjected to displacement control; thus the pressure applied to a specimen through the loading plate would be expected to be non-uniform. The model replaces the load application under displacement control with application

under load control. This would be expected to result in localized differences between the physical and simulated deformation.

Figures 8.2 and 8.3 show the vertical displacements computed using the finite element models of bridges D and E, respectively. Noting that these deflections were computed using an applied load of unit magnitude enables the specimen stiffness and first ply failure load to be calculated in the following way.

The actutator stiffness was measured during the tests of the two cell bridges, and was therefore computed using the results of the finite element analyses of the specimens. The actuator stiffness was computed by dividing the applied load by an average of the vertical displacements computed for the load application region. This vertical displacement was calculated as the average vertical displacement of the four nodes located at the corners of the load application region and the node located at the center of the load application region.

First ply failure was estimated using the Tsai-Wu failure criterion, which predicts first ply failure when the failure index

$$\Phi = \left(\frac{\sigma_L}{\sigma_{L_U}}\right)^2 - \left(\frac{\sigma_L}{\sigma_{L_U}}\right)\left(\frac{\sigma_T}{\sigma_{T_U}}\right) + \left(\frac{\sigma_T}{\sigma_{T_U}}\right)^2 + \left(\frac{\sigma_{LT}}{\sigma_{LT_U}}\right)^2 \qquad (1)$$

is equal to one. In Equation (1), σ_L is the normal stress in the longitudinal (i.e., fiber) direction, σ_T is the normal stress in the transverse direction and σ_{LT} is the in-plane shear stress. The subscript U denotes the ultimate values of these stresses.

Since the structure will deform linearly up to first ply failure, the results of the linear analyses described above can be scaled according to the value of the failure index computed at the unit applied load: the applied load is scaled so that it produces a maximum failure index equal to one.

Table 8.3 shows the model stiffness and first ply failure loads computed using the results of the finite element analysis described above.

8.2 Six Cell Bridges

Finite element models were constructed of bridges #1, #2, #4 and #5, i.e., all of the six cell bridges except the specimen used in the fatigue test. This bridge (bridge #3) was identical to bridge #2 with the exception that the supported length of bridge #3 was 2 in. shorter that bridge #2.

Figures 8.4 and 8.5 show the finite element mesh constructed to model these four bridges. The mesh used for the shorter bridge #1 consisted of 16,019 nodes and 17,056 S4R5 four-node shell elements. The meshes used for bridges #2, #4 and #5 were identical and consisted of 23,353 nodes and 24,960 S4R5 four-node shell elements. As was done with the meses for the two cell bridges, nodes were placed at the locations of the four LVDT's employed during the specimen tests and the meshes were designed so that a contiguous patch of elements was placed over the load application region. Table 8.4 lists the lamina thicknesses and winding angles that were used in the inner cells and the outer shells for each of the six cell bridges. The boundary conditions and applied loads were similar to those used for the two cell bridges.

Figures 8.6, 8.7, 8.8 and 8.9 show the vertical displacements computed using the finite element models of the four six cell bridges. Since these deflections were computed using an applied load of unit magnitude, the specimen stiffness and first ply failure load were calculated using the same procedure employed for the two cell bridges. An additional set of specimen stiffness measurements were made during the experimental testing of the six cell bridges, namely the LVDT stiffness. The LVDT stiffness was calculated by dividing the unit applied load by the vertical displacements computed at the nodes positioned at the locations of the LVDT's.

Tables 8.5 and 8.6 show the model stiffness and first ply failure loads computed using the results of the finite element analyses of the four six cell bridges.

Material Property	Symbol	E-glass Epoxy	Carbon Epoxy
Longitundinal Young's modulus	E_L	5.7 Msi	20 Msi
Transverse Young's modulus	E_T	0.7 Msi	1.5 Msi
Poisson's ratio	υ_{LT}	0.31	0.21
Shear modulus	G_{LT}	0.7 Msi	0.95 Msi
Longitudinal tensile strength	$\hat{\sigma}_{L_T}$	160 ksi	210 ksi
Longitudinal compressive strength	$\hat{\sigma}_{L_C}$	90 ksi	210 ksi
Transverse tensile strength	$\hat{\sigma}_{T_T}$	14 ksi	6.5 ksi
Transverse compressive strength	$\hat{\sigma}_{T_C}$	120 ksi	34 ksi
Shear strength	$\hat{\sigma}_{LT}$	12 ksi	9 ksi

Table 8.1: Material properties used in the finite element analysis.

	Bridge D	Bridge E
Length (in.)	51	51
Unsupported Length (in.)	50	51
Inner Cell Winding Angle (degrees)	+/-45	+/-45
Outer Shell Winding Angle (degrees)	+/-29	+/-29
Inner Cell Thickness - Four Layers (in.)	0.0704	0.0680
Outer Shell Thickness - Six Layers (in.)	0.1110	0.1110

Table 8.2: Dimensions of the two cell bridges.

Name	Stiffness	First Ply Failure
Bridge D	3,513 lb/in	1,177 lbs
Bridge E	4,130 lb/in	826 lbs

Table 8.3: Computed specimen stiffnesses and strengths for the two cell bridges.

	Bridge #1	Bridge #2	Bridge #4	Bridge #5
Length (in.)	41	60	60	60
Unsupported Length (in.)	40	59	59	59
Inner Cell Winding Angle (degrees)	+/-45	+/-45	+/-45	+/-45
Outer Shell Winding Angle (degrees)	+/-33	+/-50	+/-50	+/-50
Inner Cell Thickness - Four Layers (in.)	0.0704	0.0732	0.0704	0.0680
Outer Shell Thickness - Six Layers (in.)	0.1122	0.1146	0.1158	0.1110

Table 8.4: Dimensions of the six cell bridges.

	Bridge #1	Bridge #2	Bridge #4	Bridge #5
Actuator	7,019 lb/in	4,116 lb/in	4,574 lb/in	5,620 lb/in
LVDT 1	12,051 lb/in	7,039 lb/in	7,859 lb/in	9,360 lb/in
LVDT 2	12,051 lb/in	7,039 lb/in	7,859 lb/in	9,360 lb/in
LVDT 3	23,596 lb/in	6,531 lb/in	7,423 lb/in	8,151 lb/in
LVDT 4	23,596 lb/in	6,531 lb/in	7,423 lb/in	8,151 lb/in

Table 8.5: Computed specimen stiffnesses for the six cell bridges.

	First Ply Failure
Bridge #1	1,318 lb
Bridge #2	1,358 lb
Bridge #4	1,433 lb
Bridge #5	989 lb

Table 8.6: Computed specimen strengths for the six cell bridges.

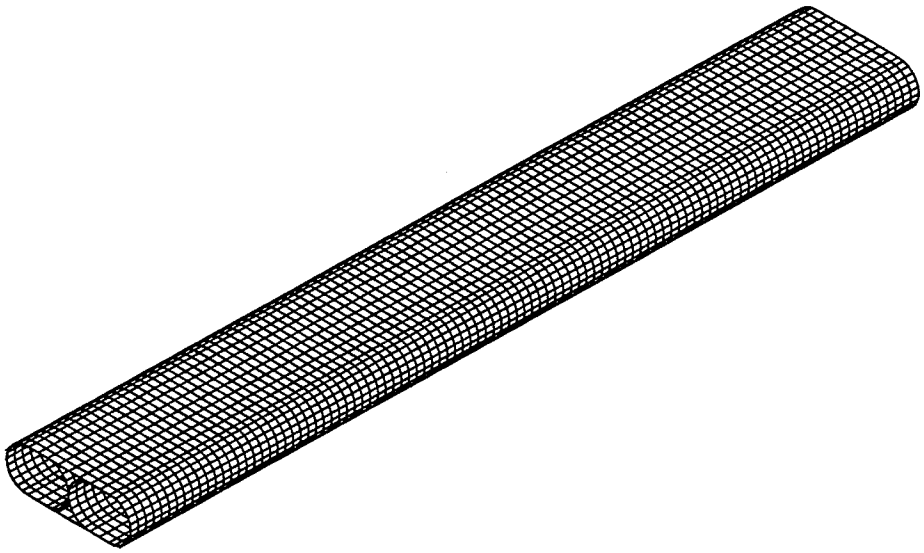

Figure 8.1: Finite element mesh employed for the two cell bridges.

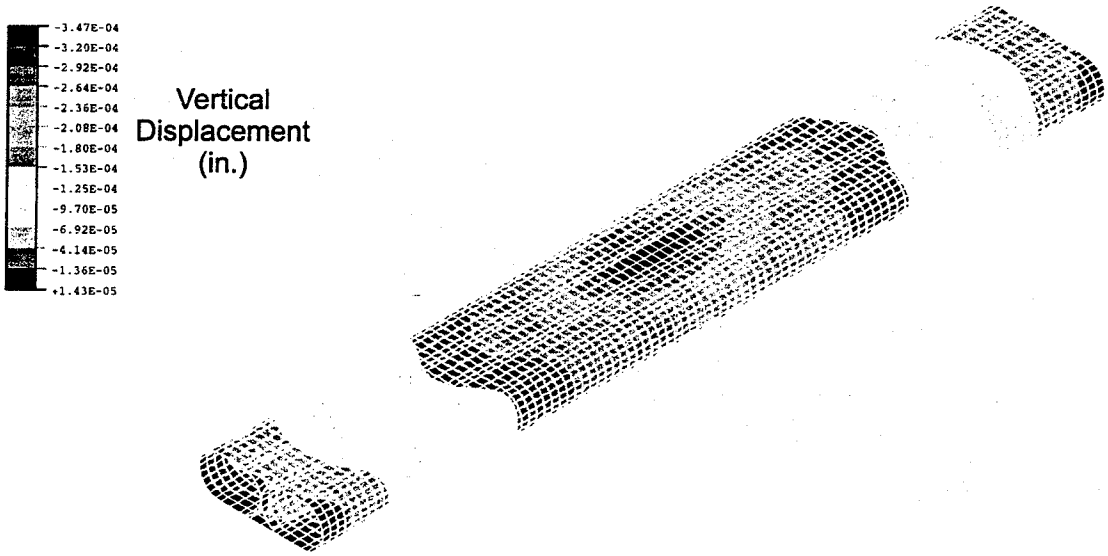

Figure 8.2: Vertical displacements computed for bridge D.

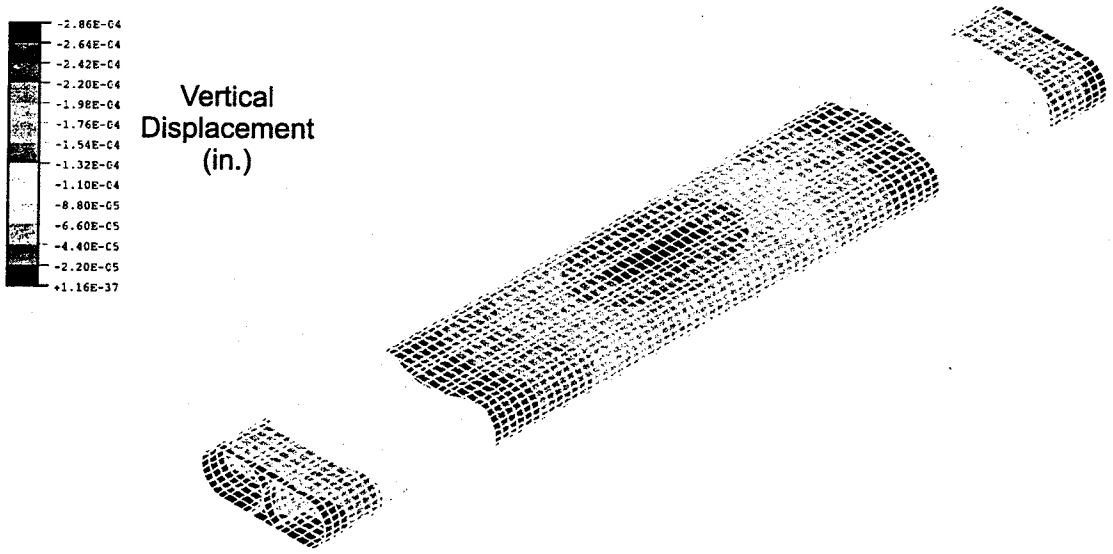

Figure 8.3: Vertical displacements computed for bridge E.

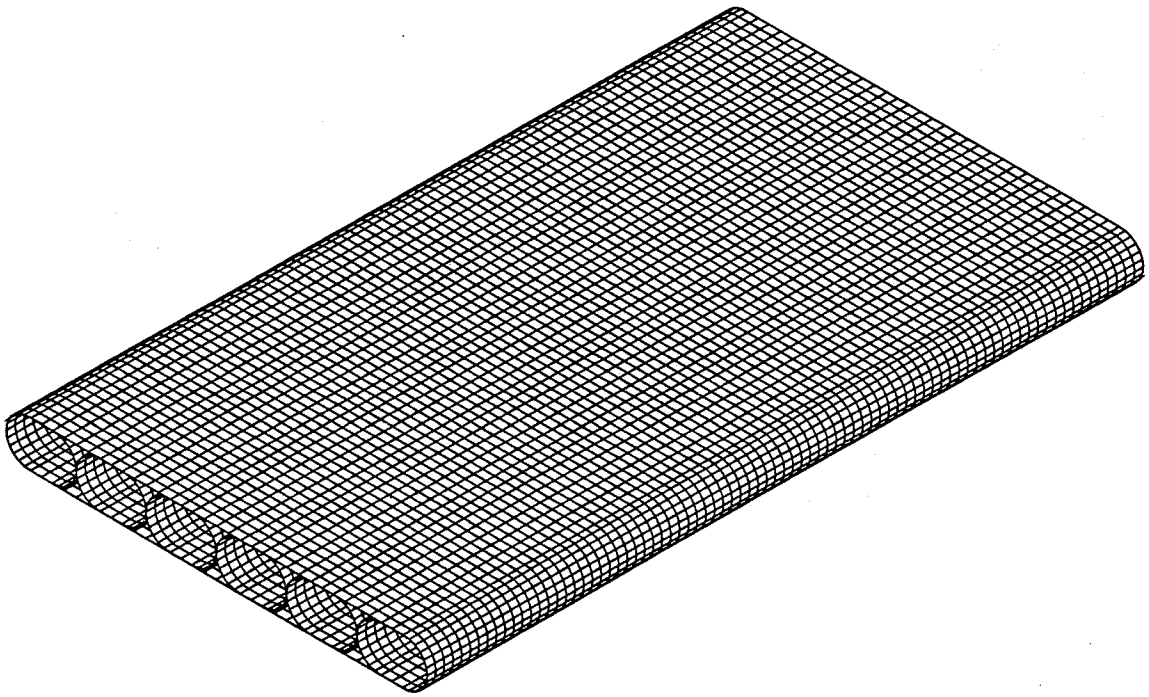

Figure 8.4: Finite element mesh employed for the bridge #1.

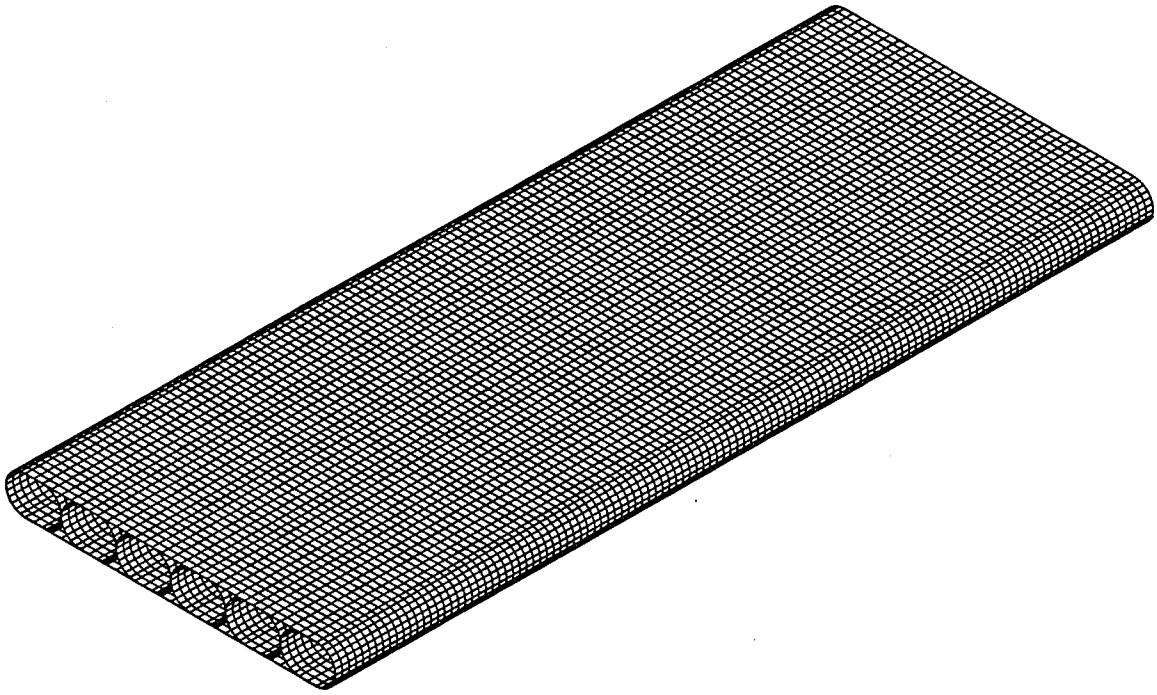

Figure 8.5: Finite element mesh employed for bridges #2, #4 and #5.

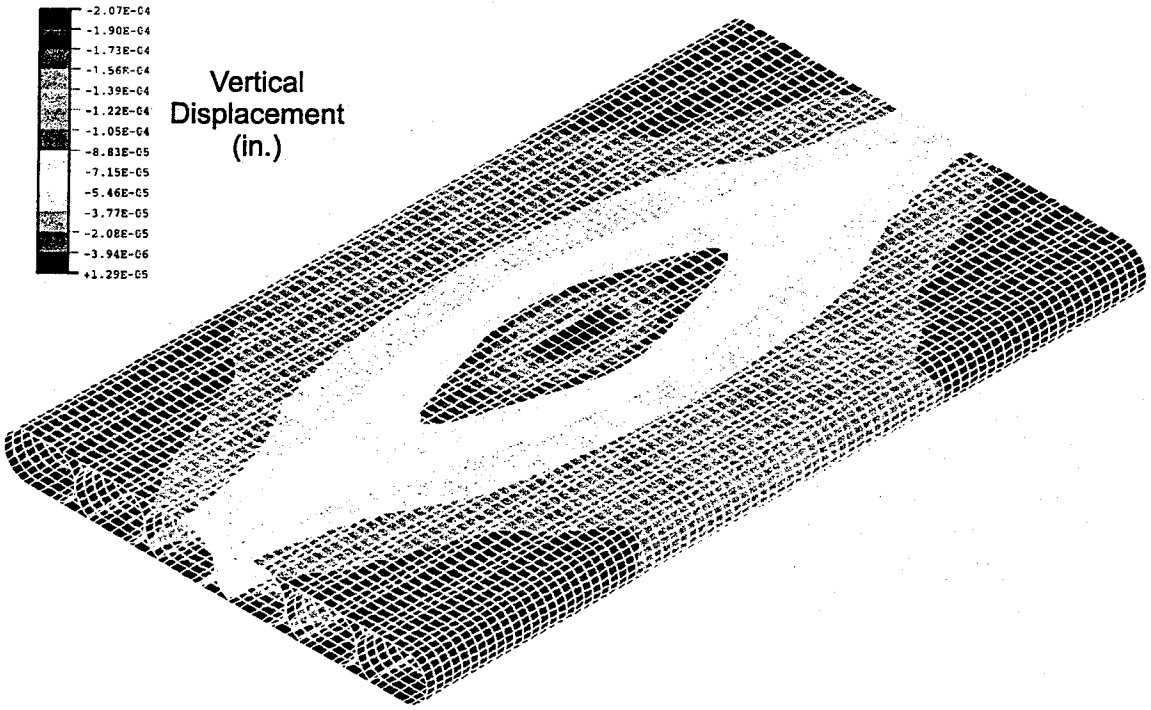

Figure 8.6: Vertical displacements computed for bridge #1.

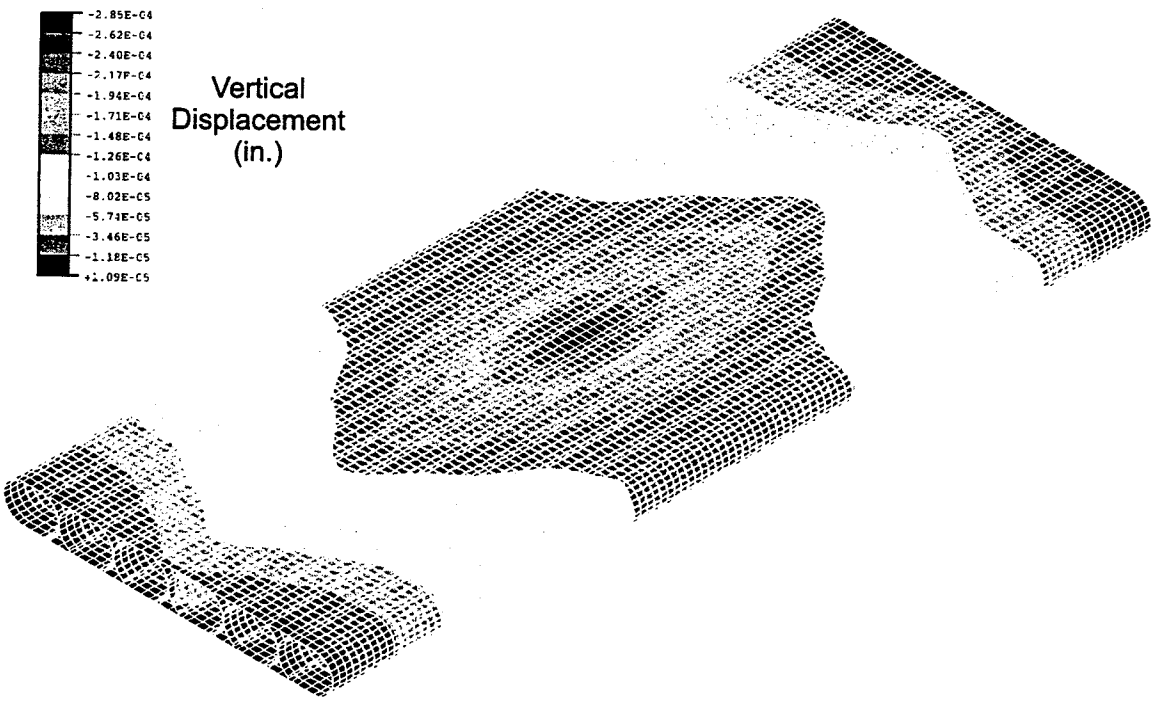

Figure 8.7: Vertical displacements computed for bridge #2.

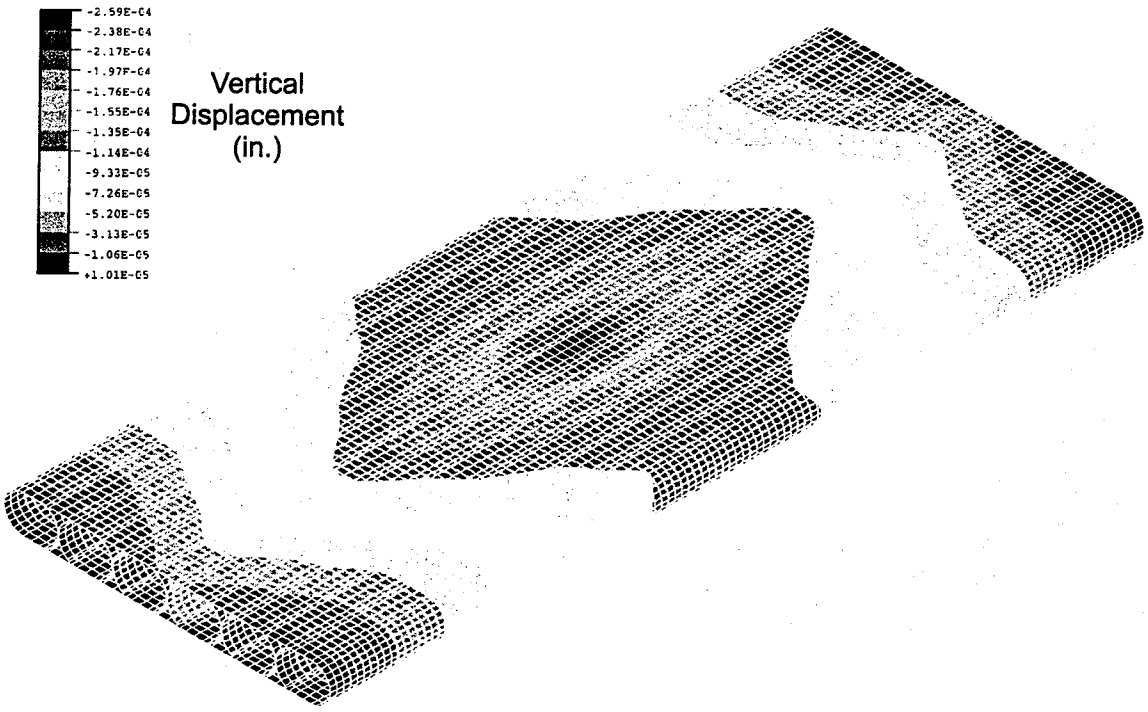

Figure 8.8: Vertical displacements computed for bridge #4.

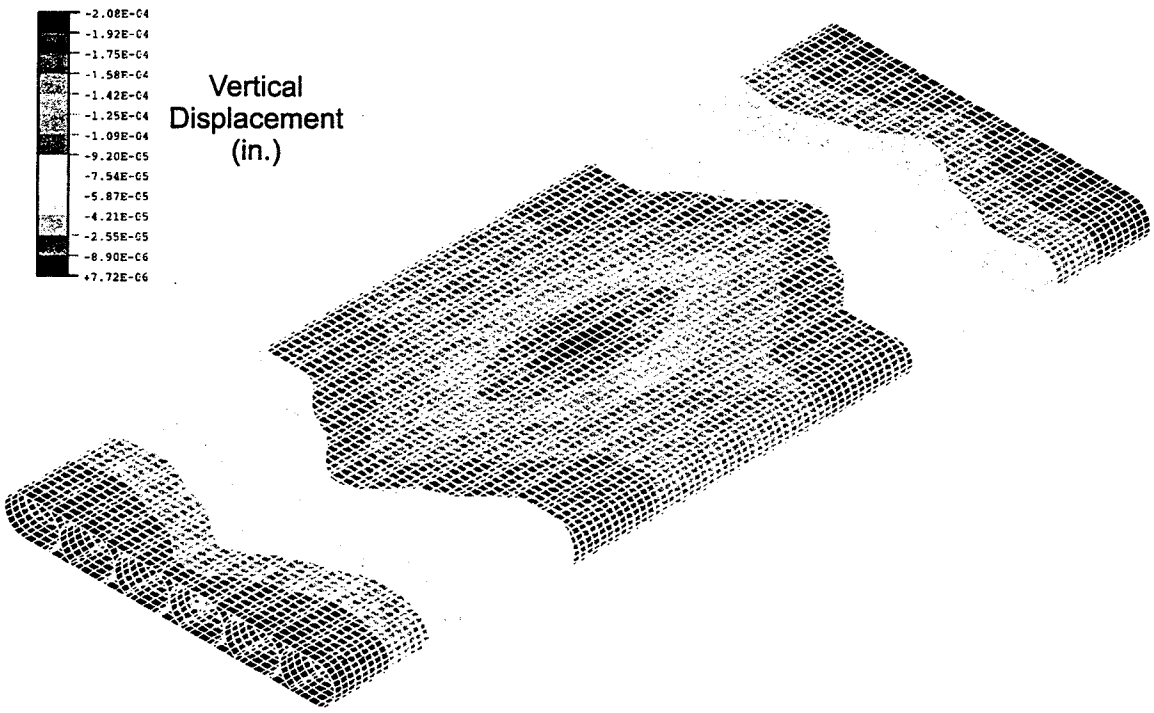

Figure 8.9: Vertical displacements computed for bridge #5.

9. Discussion of Results

The objectives of the research described in this report were to: (1) demonstrate that the proposed bridge superstructure could be manufactured; (2) perform experiments to measure the stiffness, strength and fatigue properties of small-scale fabricated specimens; and (3) build finite element models to determine whether these models could be used to predict the performance of the manufactured specimens. This chapter discusses the results presented in the preceding chapters in the context of the project objectives.

9.1 Manufacture of the Proposed Bridge Superstructure

Chapters 4 and 5 presented the methodology adopted to manufacture small-scale versions of the proposed bridge design. The physical size of the specimens was limited by the available manufacturing equipment (i.e., the filament winder and the autoclave). However, sufficient experience was gained to develop a repeatable manufacturing process that was used to construct a number of specimens having different characteristics, including length, number of cells, material type and winding angles. The basic process of winding and curing individual inner cells followed by the winding of the outer shell over the chosen number of inner cells is potential scalable to full-size structures. Special care is required to ensure that the inner cells can be removed from the mandrel after curing and that support is provided for the portion of the outer shell that is not directly attached to the inner cells.

Two significant problems arose during the manufacture of the specimens that were not fully solved in this project. First, the relatively small outer shell winding angle employed for bridge #1 produced significant variability in the quality of the final part. Specifically, the length of the filament winding machine coupled with the desire to produce a bridge with at least a 2:1 length:width aspect ratio resulted in fiber placement at the ends of the outer shell that was not consistent with the desired winding angle. This problem would be solved by using a longer winder or by reducing the width of the structure.

Second, the manufacture of hybrid bridges (i.e., bridges composed of glass and carbon reinforced fiber) proved to be problematic. Tow approaches were tried: placing

carbon fibers in the outer shell (bridge #4) and making the inner cells out of carbon (bridges E and #5). The two hybrid six cell bridges (bridges #4 and #5) developed cracks in the inner cells during the curing of the outer shell. The cause of this cracking was not clear and could have been due to thermal effects. However, the hybrid two cell bridge (bridge E) did not appear to have any such defects. Further work would be required to investigate this problem further before attempting to construct larger scale hybrid bridges.

9.2 *Testing of the Fabricated Specimens*

Chapters 6 and 7 describe the test procedures employed in this project and the results that were obtained from the experiments. Five two-cell bridges were fabricated and tested to refine the test procedures and investigate the effect of gaps between the inner cells. The tests of the two-cell bridges demonstrated that it was not necessary to place end supports in the inner cells to develop the full capacity of the bridges. This was apparent by noting that the failure of the unsupported bridges did not involve local collapse of the inner cells. Introduction of a gap between the inner cells resulted in a reduction of specimen stiffness; this reduction increased with the gap size. This effect was predicted in [4] and may be attributed to the membrane stiffness of the inner cells. The hybrid two-cell bridge was observed to have a higher stiffness than the glass fiber two-cell bridges; however, the strength of the hybrid bridge was lower than the glass fiber bridges. All of the two-cell bridges exhibited essentially linear behavior until their load capacity was reached. The failure of the specimens was sudden and brittle in nature. Various cracking noises were evident during the tests, and were sometimes accompanied by small reductions in the applied loads.

Some of the data obtained from the testing of the two-cell bridges was used for comparison with finite element models of these specimens. This comparison is discussed in Section 9.3.

Five six-cell bridges were manufactured and tested. The overall behavior of these specimens was similar to that observed during the tests of the six-cell bridges. The specimens behave linearly until failing in a sudden and brittle manner. Cracking noises were perceived at various intermediate loads, together with reductions in the applied load. Specimen stiffnesses were measured using the actuator instrumentation and four LVDT's

placed on the top surface of the outer shell. Several strain gauges were also used; however, the data obtained from these strain gauges did not produce any useful insights into the behavior of the specimens and is therefore not presented in this report.

The six-cell bridges can be arranged into three groups: (1) glass fiber bridges used to measure stiffness and strength (bridges #1 and #2); (2) a glass bridge used to investigate the behavior of the design under cyclic loads (bridge #3); and (3) hybrid bridges used to measure stiffness and strength (bridges #4 and #5). The stiffness and strength of bridges #1, #2, #4 and #5 (i.e., the frist and last of these groups) are presented in Chapter 7 and were used to investigate the validity of finite element models of these specimen (see Section 9.3).

The fatigue test of bridge #3 demonstrated that the stiffness and strength of the proposed design was not effected by the application of 3 million cycles of an applied load chosen to produce a 20% greater deflection than the AASHTO standard of $L/800$. Measurements of the specimen's stiffness were taken at the start of the cyclic load test and after every 1 million cycles; no reduction in stiffness was evident. The strength of bridge #3 at the end of the cyclic load test was observed to be similar to the strength of bridge #2, which had identical nominal geometric and material properties.

9.3 *Finite Element Analysis of the Manufactured Specimens*

Chapter 8 describes the finite element analyses that were conducted to predict the behavior of some of the specimens, namely bridges D, E, #1, #2, #4 and #5. Tables 9.1, 9.2 and 9.3 present the errors between the computed and measured specimen stiffnesses and first ply failures. In these tables, the error in a given stiffness is defined as

$$e_{stiff} = 1 - \frac{k_{FEM}}{k_{EXP}} \tag{9.1}$$

where k_{FEM} and k_{EXP} are the stiffness computed using the finite element model and the stiffness measured from the test, respectively. The error in a given first ply failure is defined as

$$e_{FPF} = \frac{P_{FEM}}{P_{EXP}} \tag{9.2}$$

where P_{FEM} and P_{EXP} are the first ply failure loads computed using the finite element model and observed during the test, respectively.

The data presented in Tables 9.1, 9.2 and 9.3 show that the finite element models were generally unsuccessful in predicting the performance of the various specimens. However, there were some successes. The actuator stiffness of the two-cell bridges (bridges D and E) was successfully predicted by the finite element models, as was all of the stiffness for bridge #2. The lack of agreement between the measured and predicted stiffness for the remaining six-cell bridges could be attributed to the manufacturing defects present in these three specimens (see Section 9.1). Local defects in the winding of the outer shell (bridge #1) and the development of crack in the inner tubes during curing (bridges #4 and #5) could have resulted in a loss of stiffness.

The predictions of first ply failure were substantially lower than those observed during the tests. It should be noted that the observed values were made based on the perception of audible cracking sounds, and did not always correlate with any noticeable change in the measured load-deflection response. Moreover, it is conceivable that first ply failure did initiate at loads lower than those reported and was simply not detected due to the lack of appropriate instrumentation. The ultimate load carrying capacity of all of the specimens was substantially greater than both the computed and observed first ply failures.

9.4 Conclusions

The research documented in this report has demonstrated that small-scale prototypes of the proposed bridge superstructure can be manufactured using basic filament winding equipment. Care was required to ensure that the specimens were free of manufacturing defects. Some specimens contained defects, but these were attributed to the limitations of the equipment available and unsolved problems that arise when different materials are integrated into the same specimen. The structural tests of the manufactured specimens demonstrated that the structural properties of the prototypes did not deteriorate when the bridge was subjected to cyclic loads. The test also produced measurements of the stiffness and strength of the various specimens. These data were used in attempt to

validate finite element models of the prototypes. The models were generally unsuccessful in reproducing the measured structural properties. However, the finite element model did accurately predict the specimen stiffness when the specimen was free of manufacturing defects. First ply failure was consistently under-estimated by the models; this may have been due to the difficulties inherent in observing fist ply failure in complex structures. The ultimate loads of the specimens were substantially greater than the first ply failure loads predicted by the models or observed during the tests.

This research indicates that full-scale prototypes of the proposed design could be manufactured using appropriate equipment. Finite element models could be expected to accurately predict the stiffness of defect-free specimens, but would tend to underestimate the specimen failure loads. However, previous work [3,4] indicates that the design of this type of structure would be governed by stiffness considerations. Therefore, the finite element models would be valuable in arriving at appropriate designs of the full-scale prototypes. More sophisticated models that account for the material nonlinearity may give further insight into the failure mechanisms at work.

	Stiffness	First Ply Failure
Bridge D	2.3%	49.1%
Bridge E	3.4%	75.1%

Table 9.1: Finite element analysis errors for the two-cell bridges.

	Bridge #1	Bridge #2	Bridge #4	Bridge #5
Actuator	20.5%	5.0%	75.8%	18.6%
LVDT 1	36.9%	2.8%	47.3%	24.2%
LVDT 2	41.2%	3.4%	34.4%	32.8%
LVDT 3	50.0%	12.4%	55.7%	26.5%
LVDT 4	34.0%	7.9%		27.2%

Table 9.2: Finite element analysis errors for the stiffnesses of the six-cell bridges.

Name	First Ply Failure
Bridge #1	65.9%
Bridge #2	52.2%
Bridge #4	47.6%
Bridge #5	45.5%

Table 9.3: Finite element analysis errors for the first ply failure of the six-cell bridges.

10. References

[1] S. Alampalli, A. Yannotti and J. O'Connor. Extending life of bridges using FRP composites. International Conference and Exhibition on Structural Faults and Repair, London, July 1999.

[2] American Association of State Highway and Transportation Officials, AASHTO LRFD Bridge Design Specifications. 1994.

[3] A. Aref and I. D. Parsons. Design optimization procedures for a fiber reinforced plastic bridge. Journal of Engineering Mechanics, 125, 1040-1047, 1999.

[4] A. J. Aref and I. D. Parsons. Design and performance of a modular fiber reinforced plastic bridge. Composites - Part B Engineering, 31, 619-628, 2000.

[5] C. Dumlao et al. Demonstration low-cost modular composite highway bridge. Proceedings of the First International Conference on Composites in Infrastructure, Saadatmanesh, H. and Ehsani, M. R., editors, 1141-1155, 1996.

[6] Federal Highway Administration. National Bridge Inventory 1995.

[7] W. Finch et al. Bridge rehabilitation using composite materials. Infrastructure: New Materials and Methods of Repair, K. D. Basham, editor, 1135-1140, 1994.

[8] D. C. Foster, D. Richards and B. R. Bogner. Design and installation of fiber-reinforced polymer composite bridge. Journal of Composites for Construction 4, 33-37, 2000.

[9] Hayes, M. D. et al. Performance of tube and plate fiberglass composite bridge deck. Journal of Composites For Construction 4, 48-55, 2000.

[10] P. R. Head. Advanced composites in civil engineering - a critical overview at this high interest, low use stage of development. Advanced Composite Materials Bridges and Structures, M. M. Elbadry, editor, 3-13, 1996.

[11] E. M. Lenoe. Attempts to introduce new materials into bridging. Infrastructure: New Materials and Methods of Repair, K. D. Basham, editor, 64-71, 1994.

[12] R. Lopez-Anido et al. Development and demonstration of a modular FRP deck for bridge construction and replacement. International Composites Expo 97 conference, Composites Institute 1997, 16-D.

[13] F. C. McCormick. Field study of a pedestrian bridge of reinforced plastic. Transportation Research Record 1118, 1987.

[14] Plecnik, J. M. and Henriquez, O. Applications of composites in highway bridges. Chapter 51 in Bridge Engineering Handbook, Chen, W.-F. and Duan, L., editors. CRC Press, 1999.

[15] S. N. Sotiropoulos, H. V. S. GangaRao and A. N. Mongi. Theoretical and experimental evaluation of FRP components and systems. Journal of Structural Engineering, 120, 1994.

[16] F. Seible. Advanced composites materials for bridges in the 21st century. Advanced Composite Materials Bridges and Structures, M.M. Elbadry, editor, 17-40, 1996.